An Equation of State with the Complete SU(3)$_f$ Baryon Octet for Neutron Star Mergers

by
Gabriel B. Frohaug

A dissertation submitted to the Department of Computer Science,

College of Natural Sciences and Mathematics

in partial fulfillment of the requirements for the degree of

Doctor of Philosophy
in Physics

Chair of Committee: Claudia Ratti

Committee Member: Carlos Ordonez

Committee Member: Rene Bellwied

Committee Member: Annalisa Quaini

University of Houston
December 2025

ACKNOWLEDGMENTS

This research would have not been possible without the assistance of Claudia Ratti, the adviser and the one who helped me find this project; Johannes Jahan, who helped me with the earlier stages of the dissertation; and Konstantin "Kostya" Maslov, who helped me get through the work for the final year of the dissertation.

I'd also thank my father, Dwight, who encouraged me to stay focused on this task whenever I got distracted.

ABSTRACT

Above 2–3 times saturation density (n_0), the neutron star equation of state (EoS) is predicted to contain strange quarks, but it is difficult to model the strange degrees of freedom in a way that correctly predicts a maximum neutron star mass in excess of the heaviest known neutron stars, such as PSR J0740+6620 ($2.08 \pm 0.07\ M_\odot$), and which correctly predicts the radius and tidal deformability of neutron stars, particularly that measured for the predecessors of GW170817. We also demonstrate that existing density-dependent relativistic-mean-field (DD-RMF) EoSs do not accurately predict the single-particle potential of hyperons in both symmetric and neutron matter at n_0, as predicted by the HALQCD Collaboration's lattice QCD-informed Brückner–Hartree–Fock (BHF) model. We develop a new EoS, DID (for "density- and isospin-dependent"), that includes the complete $\mathrm{SU}(3)_f$ ground-state baryon octet as well as a novel isospin-density dependence. It correctly predicts the HALQCD hyperon potentials and is consistent with neutron star observables, including the maximum mass. The cold β-equilibrated EoS features a Σ^- baryon that appears before the Λ, as well as a c_s^2 that peaks near 0.71 around 4 n_0 and dips to around 0.54 near 6.5 n_0. A software tool has also been constructed for solving DD-RMF EoSs and the Hempel–Schaffner-Bielich crust model.

TABLE OF CONTENTS

LIST OF TABLES

LIST OF FIGURES

1 Preface

1.1 List of acronyms

To save space, many terms in this dissertation have been abbreviated to acronyms. We use the following acronyms:

- BH: Black hole
- BHF: Brückner–Hartree–Fock
- CFL: Color–flavor-locked
- CG: Clebsch–Gordan
- ChEFT: Chiral effective field theory
- DBHF: Dirac–Brückner–Hartree–Fock
- DD: Density-dependent
- DIS: Deep inelastic scattering
- EoM (pl. EoMs): Equation of motion
- EoS (pl. EoSs): Equation of state
- GMR: Giant monopole resonance
- GUT: Grand Unified Theory
- GW: Gravitational wave
- HIC: Heavy-ion collision
- HS: Hempel–Schaffner-Bielich
- LO: Least order (in a perturbative expansion)

- LQCD: Lattice QCD
- MLE: Maximum likelihood estimate
- NLO: Next-to-least order
- N^{k}LO: $(k+1)$th-to-least order
- NS: Neutron star
- NSE: Nuclear statistical equilibrium
- PN: Post-Newtonian
- QCD: Quantum chromodynamics
- QED: Quantum electrodynamics
- QGP: Quark–gluon plasma
- RMF: Relativistic mean field
- SN (pl. SNe): Supernova
- TOV: Tolman–Oppenheimer–Volkoff

1.2 Sign convention

There are two competing sign conventions for the Minkowski metric tensor $\eta_{\mu\nu}$: the "East Coast" convention with $\eta_{\mu\nu} = \mathrm{diag}(-1, +1, +1, +1)$, and the "West Coast" convention $\eta_{\mu\nu} = \mathrm{diag}(+1, -1, -1, -1)$. The West Coast convention is common in particle physics, while the East Coast one is common in general relativity. We use the West Coast convention unless otherwise noted.

2 Introduction

2.1 The Standard Model

There are four known fundamental forces in nature: gravity, electromagnetism, the weak force, and the strong force. Of these four, gravity is well-described within Einstein's general relativity, but there is no known consistent description of gravity that includes quantum mechanics. However, quantum mechanics is consistent with the gravity-free special relativity, and the remaining three fundamental forces are described in quantum mechanics as the Standard Model [3, 1]. The Standard Model also provides a taxonomy of the known subatomic particles. While the Standard Model does not explain gravity, dark matter, dark energy, neutrino oscillation, and the preponderance of matter over antimatter, it is the best known description of nature up to energies of at least 13 TeV, and the most rigorously tested theory in all of science.

In the Standard Model, there are twelve matter fermions, all with spin 1/2, arranged in three generations, with each generation containing an up-type quark with electric charge $+2/3\ e$, a down-type quark with $-1/3e$, a charged lepton with charge $-e$, and a near-massless neutrino with no charge; each has a distinct antiparticle with equal mass and opposite charge [1]. These particles interact via exchange of gauge bosons with spin 1. The model also contains the uncharged, spin-0 Higgs boson, which is related to the unification of the electromagnetic and weak forces at energy scales above ~ 246 GeV into a unified electroweak force, and is responsible for the masses of all other massive particles except the neutrinos. Its discovery at the LHC in 2012 was an important vindication of the Standard Model as the description of nature at low energies.

The gauge boson that carries the electromagnetic force is the photon, which has zero mass; it couples to electrically charged particles, and the theory which describes this sector of the Standard Model is QED. Since the photon has no mass, the electromagnetic force can act on long ranges, and together with gravity describes everything that happens at macroscopic scales.

The weak force is mediated by the $W^{\pm}$ and Z bosons, which respectively have electric charge $\pm e$ and 0. These bosons have mass due to the Higgs mechanism that also produces the Higgs boson

and confers mass to the fermions (except neutrinos): the W bosons weigh about 80 GeV and the Z has mass around 91 GeV, and therefore the weak force is attenuated at a length scale of about $\hbar c/m_Z = 2.2$ am.[1] The weak force mediates β decay and is the only phenomenon in the Standard Model that breaks matter–antimatter (C), mirror-image (P), or time-reversal (T) symmetry [3].

The strong force is mediated by the gluon, also massless, which couples to quarks as well as to other gluons within the framework of QCD. As we will see later, the coupling of gluons to gluons causes the strong force to increase with distance, and this effect cuts off the strong force on scales longer than ~ 1 fm and confines quarks and gluons into hadrons. This property also makes it difficult to describe energy scales below ~ 200 MeV using QCD. In fact, the problem of formally proving the confinement property of QCD is one of the seven Clay Mathematics Institute Millennium Prize Problems [32, 33].

QCD can be modeled non-perturbatively as LQCD, a discrete path-integral model of QCD that localizes quark and gluon fields to a lattice in Euclidean spacetime [13]. This spacetime is related to the real Minkowski spacetime by Wick rotation to imaginary time, substituting $t \to -i\tau$ in the metric.

2.2 QCD matter and NSs

QCD matter can be described at high density or temperatures using an asymptotic, perturbative expansion: a color superconductor phase at low temperature and high density, and a quark–gluon plasma (QGP) phase at high temperatures. At low temperatures and densities (up to about 2.5×10^{14} g cm^{-3}), QCD matter exists as hadrons, and its properties can be captured using an effective field theory called ChEFT and the study of atomic nuclei. However, it is poorly understood at low temperature and intermediate density because, besides the non-perturbative nature of QCD at low energy, the fermion sign problem prevents accurate integration of the EoS with LQCD unless there is no net baryon number [34]. Instead, this information is limited to empirical studies of HICs for the QGP phase and the predicted first-order transition to hadrons at high density; and of NSs

[1] The Higgs coupling to fermions is a Yukawa interaction, which is universally attractive [31] and proportional to fermion mass [3], and at a mass of 125 GeV it attenuates at a similar length scale as the weak bosons.

for bulk properties of cold dense QCD matter.

NSs are extremely dense degenerate objects, ~ 10 km in radius and about 1.4–2.2 $M_\odot$ in mass, formed when a star with initial mass 8–25 $M_\odot$ reaches the end of its life and goes SN [35]. Originally theorized by Walter Baade and Fritz Zwicky in 1934 [36], they would consist mostly of neutrons and be formed as a possible SN remnant. In 1965, a small, radio-bright object that is distinguishable from a quasar was identified within the Crab Nebula in Taurus, which was known to have been the remnant of the SN in 1054 [37]. In 1967, an exceptionally bright X-ray source, Scorpius X-1, was identified by I. S. Shklovsky as an NS that is accreting gas from a visible object [38]. The same year, Jocelyn Bell Burnell discovered a periodic 1.3-s signal in the constellation of Vulpecula, now known as PSR B1919+21, at Mullard Radio Astronomy Observatory in Cambridge, United Kingdom. Initially attributed to aliens because of its unnaturally short period and extrasolar origin, Bell Burnell soon identified three additional sources with similar properties, including the Cassiopeia A SN remnant [39]. It was soon determined, based on the 33-ms period of the Crab Nebula source, that these objects, now known as pulsars, must be extremely compact rotating objects, and could only be NSs [40].

The properties of NSs are poorly understood. At intermediate densities between atomic nuclei and the perturbative regime, there should be enough Fermi pressure in cold QCD matter to produce strange quarks. However, it remains undetermined if this occurs in the form of kaons, strange baryons (a.k.a. hyperons), or a transition to a color-superconductor phase; some models also predict a pion condensate [35, 14, 41], a ρ^- condensate [42], or a phase that includes the non-strange, spin-3/2 Δ baryons [41, 43]. It is also hard to justify the observed high mass of some NSs, such as PSR J0740+6620 at 2.08 ± 0.07 $M_\odot$, particularly if the intermediate-density state includes hyperons [44, 41].

2.3 Research objective

We developed a hyperonic EoS that includes all eight baryons of the ground-state SU(3) flavor octet. In order to describe the hyperon potentials of an LQCD-informed BHF model [2] for neutron matter,

we introduce two features to the strange sector: an $SU(3)_f$-breaking ρ meson, and meson couplings that depend on isospin density. We develop a model that correctly predicts these observables an is consistent with NS observables, including the maximum mass and measurements of the radius and tidal deformability. We also aim to provide an accessible software tool for computation of DD-RMF EoSs and the NSE crust model of Ref. [45].

2.4 Summary of layout

The dissertation from here onward is organized as follows:

- Chapter 3 introduces the QCD Lagrangian and describes the quark model for hadrons.
- Chapter 4 explains the table of nuclides and provides an outline of nuclear structure.
- Chapter 5 outlines the current state of knowledge of the phase diagram of QCD matter.
- Chapter 6 describes NSs, including their structure and methods for observing them and predicting their properties from a cold-matter EoS.
- Chapter 7 describes the EoS we designed.
- Chapter 8 describes the program, including an outline of the numerical methods used to solve the EoS.
- Chapter 9 describes the procedure and data we used to fit the EoS.
- Chapter 10 describes some results for the EoS and the NS properties it predicts.
- Chapter 11 draws our conclusions.

3 Quantum chromodynamics (QCD)

In 1956, the elastic electron–proton scattering amplitude was measured at SLAC, where they found that the proton is not point-like, unlike the electron, and therefore the proton is not an elementary particle; similar measurements of electron–deuteron scattering also found a nonzero size for the neutron [3], which was already known as early as 1940 to have a nonzero magnetic moment, despite having no charge [46]. That same year, Murray Gell-Mann organized the then-known baryons and mesons (collectively, hadrons) into grids based on quantum numbers called isospin and strangeness (related to weak decays), which led to the development of the Eightfold Way in 1961, and eventually the quark model in 1964 to explain their organization [3].

In the quark model, the isospin T and strangeness $\mathcal{S}$ are related to three flavors of quarks, called up (u), down (d), and strange (s), with baryons made of three quarks and mesons made of one quark and one antiquark. The baryon number B is $+1/3$ for each quark and $-1/3$ for each antiquark, and is a globally conserved quantity in the Standard Model. The up and down quarks have isospin $1/2$, with the projected isospin T_3 equal to $+1/2$ for the up quark with charge $+2/3$ e, and $-1/2$ for the down quark with charge $-1/3$ e. The strange quark has $\mathcal{S} = -1$ and charge $-1/3$ e. Their antiquarks have opposite charge, T_3, and strangeness. Together with the subsequently discovered quark flavors charm (c, $\mathcal{C} = +1$), bottom (b, $\mathcal{B} = -1$), and top (t, $\mathcal{T} = +1$), we have the Gell-Mann–Nishijima formula for the charge of a quark or hadron, in units of e, based on its baryon number and flavor quantum numbers:

$$Q = \frac{1}{2}(B + 2T_3 + \mathcal{S} + \mathcal{C} + \mathcal{B} + \mathcal{T}) \tag{1}$$

The quark model was quickly verified by the discovery of a predicted spin-3/2 baryon with $\mathcal{S} = -3$ and $Q = -1$, the Ω, at Brookhaven National Laboratory [47]. The quarks themselves were then observed in 1969 in DIS of an electron against a proton, which showed an excess of large scattering angles consistent with point-like contents of the proton — according to Feynman's parton model,

Table 1: Properties of the six flavors of quarks, including flavor quantum numbers. Masses are computed from fitting of LQCD to known properties of hadrons, except for the top quark, which can be measured directly in event kinematics. All quarks have baryon number $B = +1/3$ and spin $S = 1/2$; their antiquarks have opposite charge and flavor quantum numbers [1].

Generation	Quark name	Symbol	Q	Mass (MeV)	Flavor quantum numbers					
					T	T_3	$\mathcal{S}$	$\mathcal{C}$	$\mathcal{B}$	$\mathcal{T}$
1st	Down	d	$-1/3$	4.70(7)	1/2	$-1/2$	0	0	0	0
	Up	u	$+2/3$	2.16(7)	1/2	$+1/2$	0	0	0	0
2nd	Strange	s	$-1/3$	93.5(8)	0	0	-1	0	0	0
	Charm	c	$+2/3$	1273.0(46)	0	0	0	1	0	0
3rd	Bottom	b	$-1/3$	4183.(7)	0	0	0	0	-1	0
	Top	t	$+2/3$	172570.(290)	0	0	0	0	0	1

these include three real "valence" quarks (two u's and one d), plus an infinite sea of virtual quark–antiquark pairs and gluons that increase in number at small momentum fractions [3].

Table 1 lists the six flavors of quarks and their bare masses. The masses of the valence quarks in a hadron are only a small fraction of the total mass, about 1% of the proton's mass of 938 MeV; the rest comes from the quark and gluon fields (about 32% and 36%, respectively); the sea-quark condensate (about 9%); and the QCD anomaly (about 23%); less than 10% of the proton's mass is due to the quark masses conferred through the Higgs interaction [48]. On the other hand, the pseudoscalar mesons (except η') become massless and indistinguishable if the quark masses are zero [49, 50].

However, some puzzles remained in the quark model; for instance, the Δ^{++} baryon contains 3 up quarks and has symmetric spatial and spin wave functions, but Fermi statistics require a total wave function that is antisymmetric; additionally, the $\pi^0 \to \gamma\gamma$ decay was about 9 times faster than predicted by theory, and hadron production in electron–positron collisions about 3 times more common than predicted [3]. The solution was to introduce a color charge for the quarks, with each quark having one of three "colors", whimsically called red, green, and blue, and antiquarks existing in the opposite colors; the resultant theory of QCD has the quarks interacting by exchange of massless vector bosons called gluons (later identified in DIS data), which themselves have color and cause quarks to group into "white" hadrons. To understand QCD, we will first derive the $\mathrm{U}(1)_q$

gauge symmetry from the QED Lagrangian, and then the SU(N) gauge field theory, following Ref. [3].

3.1 QCD Lagrangian and gauge symmetries

3.1.1 The QED Lagrangian and gauge symmetries

Let us begin with the Lagrangian of QED,

$$\mathcal{L} = \overline{\psi}(i\not{D} - m)\psi - \frac{1}{4}F_{\mu\nu}F^{\mu\nu} \tag{2}$$

where $\overline{\psi} = \psi^\dagger\gamma^0$, the Feynman slash notation means $\not{D} = \gamma^\mu D_\mu$, the covariant derivative is

$$iD_\mu = i\partial_\mu - QeA_\mu, \tag{3}$$

e is the elementary charge in units with $\epsilon_0 = 1$, Q is the charge of the fermion in multiples of e, and the field tensor

$$F^{\mu\nu} = \partial^\mu A^\nu - \partial^\nu A^\mu. \tag{4}$$

Under gauge symmetry, we transform the fields by a scalar function $\alpha(x)$ as:

$$\begin{aligned} \psi' &= e^{iQ\alpha}\psi, \\ A'_\mu &= A_\mu - \frac{1}{e}\partial_\mu\alpha. \end{aligned} \tag{5}$$

From this, we can get

$$iD'_\mu = i\partial_\mu - QeA'_\mu = i\partial_\mu - QeA_\mu + Q\partial_\mu\alpha = iD_\mu + Q\partial_\mu\alpha. \tag{6}$$

$$\begin{aligned} F'^{\mu\nu} &= \partial^\mu A'^\nu - \partial^\nu A'^\mu \\ &= \partial^\mu A^\nu - \frac{1}{e}\partial^\nu\partial^\mu\alpha - \partial^\nu A^\mu + \frac{1}{e}\partial^\mu\partial^\nu\alpha \\ &= F^{\mu\nu}. \end{aligned} \tag{7}$$

Then the transformed action of D'_μ on ψ' is

$$\begin{aligned} iD'_\mu\psi' &= (i\partial_\mu - QeA'_\mu)(e^{iQ\alpha}\psi) \\ &= -Qe^{iQ\alpha}(\partial_\mu\alpha)\psi + ie^{iQ\alpha}\partial_\mu\psi - QeA_\mu\psi + Q(\partial_\mu\alpha)e^{iQ\alpha}\psi \\ &= e^{iQ\alpha}(i\partial_\mu - QeA_\mu)\psi \\ &= e^{iQ\alpha}D_\mu\psi \end{aligned} \tag{8}$$

Altogether, we can verify that the Lagrangian is invariant under the gauge:

$$\begin{aligned} \mathcal{L}' &= \overline{\psi}'(i\not{D}' - m)\psi' - \frac{1}{4}F'_{\mu\nu}F'^{\mu\nu} \\ &= \overline{\psi}e^{-iQ\alpha}(e^{iQ\alpha}\not{D}\psi - me^{iQ\alpha}\psi) - \frac{1}{4}F_{\mu\nu}F^{\mu\nu} \\ &= \overline{\psi}(\not{D} - m)\psi - \frac{1}{4}F_{\mu\nu}F^{\mu\nu} \\ &= \mathcal{L}. \end{aligned} \tag{9}$$

The gauge symmetry of QED is U(1), which is the multiplicative group of complex numbers with absolute value 1 — this is the factor $e^{iQ\alpha}$ within Eq. (5), and it enforces the familiar C-symmetry of electromagnetism and quantization of charge to integer multiples of e.

3.1.2 Constructing the QCD Lagrangian

Let's now consider an SU(N) gauge symmetry with N_f flavors of quark fields $q_f^a(x)$, generically called a Yang–Mills theory. The Lie group SU(N), is the group of $N \times N$ unitary matrices with determinant 1. Any $U \in \mathrm{SU}(N)$ may be written as

$$U = e^{iT_A\theta_A} \tag{10}$$

where T_A are a basis of N^2-1 traceless, Hermitian matrices that form the Lie algebra $su(N)$; they are related by

$$\mathrm{Tr}(T_A T_B) = \frac{1}{2}\delta_{AB}, \tag{11}$$

$$[T_A, T_B] = i f_{ABC} T_C, \tag{12}$$

where f_{ABC} is an antisymmetric rank-3 tensor known as the structure constants.

The quark Lagrangian may then be written as

$$\mathcal{L}_q = \overline{q}_a (i\partial\!\!\!/ - m) q^a, \tag{13}$$

where $a \in \{1, ..., N\}$ is a color index; in other words, we have N colored copies of each quark field.

The gluon field has N^2-1 fields corresponding to the basis matrices of $su(N)$, and may be abbreviated as:

$$\tilde{A}_\mu = A_\mu^A T_A \tag{14}$$

QCD has $N = 3$ colors, so it is an SU(3) gauge theory with three colors of quarks and eight colors of gluons; the $su(3)$ algebra has the basis $T_A = \lambda_A/2$, where λ_A are the Gell-Mann matrices

$$\begin{aligned}
\lambda_1 &= \begin{pmatrix} 0 & 1 & 0 \\ 1 & 0 & 0 \\ 0 & 0 & 0 \end{pmatrix} \quad \lambda_2 = \begin{pmatrix} 0 & -i & 0 \\ i & 0 & 0 \\ 0 & 0 & 0 \end{pmatrix} \quad \lambda_3 = \begin{pmatrix} 1 & 0 & 0 \\ 0 & -1 & 0 \\ 0 & 0 & 0 \end{pmatrix} \quad \lambda_4 = \begin{pmatrix} 0 & 0 & 1 \\ 0 & 0 & 0 \\ 1 & 0 & 0 \end{pmatrix} \\
\lambda_5 &= \begin{pmatrix} 0 & 0 & -i \\ 0 & 0 & 0 \\ i & 0 & 0 \end{pmatrix} \quad \lambda_6 = \begin{pmatrix} 0 & 0 & 0 \\ 0 & 0 & 1 \\ 0 & 1 & 0 \end{pmatrix} \quad \lambda_7 = \begin{pmatrix} 0 & 0 & 0 \\ 0 & 0 & -i \\ 0 & i & 0 \end{pmatrix} \quad \lambda_8 = \frac{1}{\sqrt{3}} \begin{pmatrix} 1 & 0 & 0 \\ 0 & 1 & 0 \\ 0 & 0 & -2 \end{pmatrix}.
\end{aligned} \tag{15}$$

The electroweak theory has $\mathrm{SU}(2) \otimes \mathrm{U}(1)$ gauge symmetry, which produces three W bosons and a B; below the electroweak scale, two of the W's mix into the $W^\pm$ bosons, while the third W and the B mix into the Z boson and photon. The generators of the $su(2)$ algebra are the familiar Pauli

matrices multiplied by $i/2$ [3].

By analogy to QED, we can then define a covariant derivative and a field tensor for the gluons:

$$D_\mu = \partial_\mu + ig\tilde{A}_\mu \tag{16}$$

$$\tilde{F}_{\mu\nu} = \partial_\mu \tilde{A}_\nu - \partial_\nu \tilde{A}_\mu + ig[\tilde{A}_\mu, \tilde{A}_\nu]; \tag{17}$$

the extra commutator of $\tilde{F}_{\mu\nu}$ occurs because SU(N) is non-abelian; in the abelian U(1)$_q$ gauge of QED, this term of the photon $F_{\mu\nu}$ vanishes.

Under the action of a matrix function $u(x) = e^{iT_A\theta_A(x)}$, we have:

$$\begin{aligned} q &\to uq, \\ \tilde{A}_\mu &\to u\tilde{A}_\mu u^\dagger + \frac{i}{g}(\partial_\mu u)u^\dagger. \end{aligned} \tag{18}$$

It is also useful to expand the $N^2 - 1$ components of the $\tilde{A}_\mu$ current. Using the identity

$$A^A_\mu = 2\,\mathrm{Tr}(T_A\tilde{A}_\mu) = 2\,\mathrm{Tr}(T_AT_B)A^B_\mu \tag{19}$$

$$\begin{aligned} F^A_{\mu\nu} &= 2\,\mathrm{Tr}(T_A\tilde{F}_{\mu\nu}) = 2\,\mathrm{Tr}[T_A(\partial_\mu\tilde{A}_\nu - \partial_\nu\tilde{A}_\mu + ig[\tilde{A}_\mu, \tilde{A}_\nu])] \\ &= 2\,\mathrm{Tr}[T_A(\partial_\mu\tilde{A}_\nu - \partial_\nu\tilde{A}_\mu + ig[A^B_\mu T_B, A^C_\nu T_C])] \\ &= 2\,\mathrm{Tr}[T_A(\partial_\mu\tilde{A}_\nu - \partial_\nu\tilde{A}_\mu - gA^B_\mu A^C_\nu f_{BCD}T_D])] \\ &= \partial_\mu A^A_\nu - \partial_\nu A^A_\mu - gf_{BCA}A^B_\mu A^C_\nu \\ &= \partial_\mu A^A_\nu - \partial_\nu A^A_\mu - gf_{ABC}A^B_\mu A^C_\nu \end{aligned} \tag{20}$$

Additionally, we can define an $(N^2-1)\times(N^2-1)$ matrix that is related to the covariant derivative:

$$D^{AB}_\mu = \delta_{AB}\partial_\mu - gf_{ACB}A^C_\mu. \tag{21}$$

One can verify that for a collection of scalars $\tilde{\theta}(x)$, $(D_\mu\theta)_A = D^{AB}_\mu\theta_B$.

Then the Lagrangian of the field contains a field term, a quark term, and an interaction term,

adding up to:

$$\begin{aligned}\mathcal{L} &= \overline{q}(i\not{D} - m)q - \frac{1}{4}\,\mathrm{Tr}(\tilde{F}_{\mu\nu}\tilde{F}^{\mu\nu}) \\ &= \overline{q}_a(i\not{D} - m)^a{}_b q^b - \frac{1}{4}F^A_{\mu\nu}F^{\mu\nu}_A\end{aligned} \tag{22}$$

3.1.3 Symmetries

The most obvious symmetry of the Yang–Mills Lagrangian is the $\mathrm{SU}(N)_c$ color symmtery, which we have already seen. However, focusing only on the massive term, it is straightforward to prove that there is an additional $\mathrm{SU}(n)$ flavor symmetry if two or more of the quarks have equal masses: this rotates the quark flavors under the action of a unitary matrix [3]. The group $\mathrm{U}(n) = \mathrm{U}(1) \otimes \mathrm{SU}(n)$, since any unitary matrix (of any size) can be written as the product of a scalar with absolute value 1 and

$$U = e^{i\alpha/n}U' \tag{23}$$

where $U' \in \mathrm{SU}(n)$ and $\det U = e^{i\alpha}$. Physically, the $\mathrm{SU}(n)$ subgroup rotates the quark flavors, and $\mathrm{U}(1)$ rotates quarks into their respective antiquarks.

Consider the free Lagrangian with $N_f = 2$ and equal quark masses, $q = (u\ d)^T$:

$$\mathcal{L} = \overline{q}(i\not{\partial} - m)q \tag{24}$$

If the two quarks have different masses, then this symmetry is explicitly broken by the additional Lagrangian term $-\overline{q}\,T_3\Delta m\,q$, where $T_3 = \sigma_z/2$ is the isospin operator, $\Delta m = m_u - m_d$, and $m = (m_u + m_d)/2$. In contrast, if the quarks are massless, then they can alternatively be broken into left-handed and right-handed components, q_L and q_R, via the projection operators $P_{L,R} = \frac{1\mp\gamma^5}{2}$, where

$$\gamma^5 = i\gamma^0\gamma^1\gamma^2\gamma^3 = \begin{pmatrix} 0 & I_2 \\ I_2 & 0 \end{pmatrix}. \tag{25}$$

Under this decomposition, we have an extended $\mathrm{SU}(2)_L \otimes \mathrm{SU}(2)_R$ chiral symmetry:

$$\mathcal{L} = \overline{q} i \not{\partial} q = \overline{q}_L i \not{\partial} q_L + \overline{q}_R i \not{\partial} q_R \tag{26}$$

However, this symmetry is explicitly broken by the mass term, as $\overline{q}q = \overline{q}_L q_R + \overline{q}_R q_L$ [3].

In principle, no term of the Yang–Mills Lagrangian enforces CP symmetry. The electroweak sector violates CP, but QCD is observed to respect it. This problem, known as the strong CP problem, is one of the major naturalness problems in the Standard Model; the most common hypothesis is that this symmetry is enforced by a light spin-0 particle called the axion, which may be a major constituent of dark matter [3].

3.1.4 Ghosts

In order to fix unitarity within the perturbative expansion of a non-abelian gauge theory, Faddeev and Popov introduced a fictitious ghost field, which are massless spinless fermions that couple to the gluons, and added a gauge-fixing term:

$$\mathcal{L}_c = -\frac{1}{2\xi}(\partial^\mu \tilde{A}_\mu)^2 - \overline{c}_A \partial^\mu D_\mu^{AB} c_B, \tag{27}$$

where c_A and $\overline{c}_B$ are anticommuting scalar fields, and ξ is a gauge parameter; the Feynman gauge sets $\xi = 1$, while the Landau gauge sets $\xi = 0$. It can be shown that the ghosts cause a local gauge symmetry to be replaced by a global BRST symmetry with infinitesimal transformations

$$\begin{aligned} \delta A_\mu^A &= -\omega D_\mu^{AB} c_B, \\ \delta c_A &= -\frac{1}{2} g \omega f_{ABC} c_B c_C, \\ \delta \overline{c}_A &= \frac{\omega}{\xi} \partial_\mu A_A^\mu \end{aligned} \tag{28}$$

where ω is a global anticommuting parameter. The ghosts cancel out unphysical degrees of freedom in diagrams with loops, and vanish when coupling to an abelian gauge field [51].

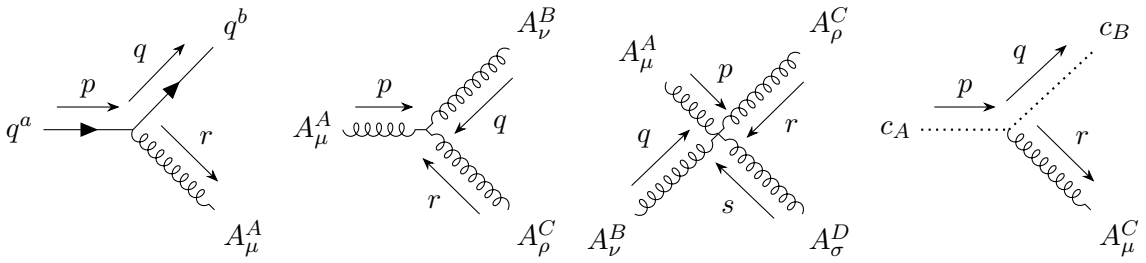

Figure 1: Allowed vertices for QCD, including quarks (solid lines with arrows), gluons (springs), and ghosts (dotted lines).

3.1.5 Feynman rules

The propagators for each particle can be derived from the Lagrangian [3]. In the quark sector,

$$\mathcal{L}_q = \overline{q}_a(i\not{D} - m)q^a, \tag{29}$$

expanding D_μ from Eq. (16) gives a free term and an interacting term,

$$\mathcal{L}_{q0} = \overline{q}_a(i\not{\partial} - m)q^a \tag{30}$$

$$\mathcal{L}_{qg} = -g\overline{q}_a\gamma^\mu\tilde{A}^A_\mu(T_A)^a{}_b q^b \tag{31}$$

The quark propagators are the same as for the electron in QED, except with a color index,

$$S^a_{\alpha\beta}(p) = i\left(\frac{\not{p} + m}{p^2 - m^2 + i\epsilon}\right)_{\alpha\beta}, \tag{32}$$

where $p^2 = p^\mu p_\mu$ is the squared norm; and the quark–gluon vertex contributes a factor of

$$L^\mu_{\alpha\beta} = -ig(\gamma^\mu)_{\alpha\beta}(T_A)^a{}_b. \tag{33}$$

Now, in the gauge sector,

$$\mathcal{L}_{gc} = -\frac{1}{4}F^A_{\mu\nu}F^{\mu\nu}_A - \frac{1}{2\xi}(\partial^\mu\tilde{A}_\mu)^2 - \overline{c}_A\partial^\mu D^{AB}_\mu c_B \tag{34}$$

Setting $g = 0$ isolates the free terms,

$$\mathcal{L}_{gc0} = -\frac{1}{4}(\partial_\mu A^A_\nu - \partial_\nu A^A_\mu)^2 - \frac{1}{2\xi}(\partial^\mu \tilde{A}_\mu)^2 - \bar{c}_A \partial^\mu \partial_\mu c_A. \tag{35}$$

The propagator for the gluons is

$$\Delta^A_{\alpha\beta}(p) = i\frac{-g_{\alpha\beta} + (1-\xi)p^\alpha p^\beta/p^2}{p^2 + i\epsilon}, \tag{36}$$

and the propagator for the ghosts is

$$D^A(p) = \frac{i}{p^2 + i\epsilon}. \tag{37}$$

The remaining terms are

$$\mathcal{L}_{gcI} = -\frac{g}{2}(\partial_\mu A^A_\nu - \partial_\nu A^A_\mu) f_{ABC} A^\mu_B A^\nu_C - \frac{g^2}{4} f_{ABC} A^B_\mu A^C_\nu f_{ADE} A^\mu_D A^\nu_E + g f_{ABC} \bar{c}_A \partial^\mu (A^B_\mu c_C). \tag{38}$$

These terms give three extra vertices: a momentum-dependent gluon 3-vertex, a gluon 4-vertex, and a gluon–ghost vertex. These vertices and the quark–gluon vertex, are drawn in Fig. 1. The gluon 3-vertex is momentum dependent, and upon symmetrizing the 3-gluon term in the Lagrangian, evaluates to

$$G^{(3)}_{\mu\nu\rho} = g f_{ABC}[g_{\nu\rho}(r_\mu - q_\mu) + g_{\rho\mu}(p_\nu - r_\nu) + g_{\mu\nu}(q_\rho - p_\rho)]. \tag{39}$$

The gluon 4-vertex is

$$G^{(4)}_{\mu\nu\rho\sigma} = -g^2[f_{ABE}f_{CDE}(g_{\mu\rho}g_{\nu\sigma} - g_{\mu\sigma}g_{\nu\rho}) + f_{ACE}f_{BDE}(g_{\mu\nu}g_{\rho\sigma} - g_{\mu\sigma}g_{\rho\nu}) + f_{ADE}f_{BCE}(g_{\mu\nu}g_{\rho\sigma} - g_{\mu\rho}g_{\sigma\nu})]. \tag{40}$$

Lastly, the ghost vertex is simply

$$C_\mu = -g f^{ABC} q_\mu. \tag{41}$$

In addition to the -1 factor on quark loops, there is also a -1 factor for each ghost loop and a $+1$

factor for each gluon loop. There are no external ghost lines because the ghosts are not a physical state.

3.2 Confinement and asymptotic freedom

The strong coupling constant $\alpha_s = g^2/4\pi$ depends on the renormalization scheme, a phenomenon related to vacuum-polarization screening of α at high energies in QED [50]. It rescales with energy as

$$\alpha_s(\mu) = \left[\frac{1}{\alpha_s(\mu_0)} - 2b_s \ln\frac{\mu}{\mu_0}\right]^{-1}, \tag{42}$$

where at one loop on the gluon propagator,

$$b_s^{(1)} = \frac{1}{12\pi}(2N_f - 33), \tag{43}$$

where N_f is the number of quark flavors below the mass scale μ — this is the famous result that α_s weakens with energy if $N_f \leq \lfloor 33/2 \rfloor = 16$. This is always true in the real world, where $N_f = 6$.[2] The standard choice of the benchmark scale μ_0 is the Z-boson mass $m_Z = 91.1880(20)$ GeV, where $\alpha_s(m_Z) = 0.1180(9)$ (in the commonly used $\overline{\text{MS}}$ scheme) [1]. This property, called asymptotic freedom, allows QCD to be calculated perturbatively at high energy scales; however, at an energy scale of

$$\Lambda_{\text{QCD}} = m_Z \exp\frac{1}{2b_s\alpha_s(m_z)}, \tag{44}$$

the one-loop renormalized α_s becomes infinite and the perturbative approximation breaks down [50]; the most meaningful choice of cutoff is $N_f = 3$, where $\Lambda_{\text{QCD}} = 246$ MeV, and this predicts a characteristic radius of $\hbar c/\Lambda_{\text{QCD}} = 0.80$ fm for hadronic interactions [50], close to the observed proton charge radius of 0.8414(19) fm [1]. Below this scale, QCD calculations require LQCD [3] or ChEFT, an effective field theory that describes interactions between nucleons via exchange of mesons [50].

[2]The two-loop correction, $b_s^{(2)} = (\alpha_s/96\pi^2)(19N_f - 153)$, can be calculated as well, also causing α_s to weaken at high mass scales if $N_f \leq \lfloor 153/19 \rfloor = 8$; higher-order terms depend on the renormalization scheme but vanish at $\mu \to \infty$ [52].

At low energies, quarks become color-confined into color-neutral hadrons [52]. The most commonly used potential between opposite-colored quark and antiquark above Λ_{QCD} is the Cornell potential [52, 53],

$$A = -\frac{4}{3}\frac{\alpha_s(r)}{r} + kr; \tag{45}$$

the first term is the one-gluon QCD potential, while the second term describes a string with constant tension between the quarks; the value measured from the charmonium ($c\bar{c}$ bound state) energy levels is $k = 0.183\ \mathrm{GeV}^2 = 0.927\ \mathrm{GeV\ fm}^{-1} = 1.49 \times 10^5\ \mathrm{N}$ [53]. Sometimes, the potential is also shifted by a constant in order to recreate the actual masses of the hadrons; the fitted value of this constant and the effective α_s depends on the hadron [53]. However, a rigorous proof of color confinement in QCD, or any other non-perturbative phenomenon at low energy, remains elusive [33].

3.3 Lattice QCD (LQCD)

Lattice field theory is a discrete model of a quantum field theory that localizes the fields onto a four-dimensional Euclidean lattice [13, 3]. This "timeless" spacetime is related to the real-world Minkowski spacetime via a Wick rotation to imaginary time: substituting t with $-i\tau$ yields a metric with all plus signs in East Coast convention, or all minuses in West Coast convention. The Euclidean spacetime does not have a Hamiltonian, so dynamical effects cannot be modeled, but correlation functions can be analyzed [3]. When formulated in the path integral formalism, quantum mechanics in Euclidean spacetime becomes closely analogous to statistical mechanics [54].

Typically, lattice field theory takes place on a tesseractic (4-hypercubic) lattice $\mathbb{Z}^4$ with edge length a. The lattice spacing establishes a UV cutoff to the theory, avoiding the divergences that occur in Feynman diagrams [3]. In computational implementations, the spacetime is limited to a cubic prism with wraparound (an instance of the torus T^4) with N_s sites along each space axis and N_t sites along the time axis, for a total size of $L_t \times L_s^3 = (a^4 N_t \times N_s^3)$ [3, 13]. In a few calculations, the lattice spacing is also shorter on the time axes, which makes it easier to calculate excited states [1]. Discretization errors of the lattice scale as a power of a ($O(a^2)$ in the simplest action), and a

should be chosen such that $1/a$ is much larger than any of the mass scales in the field theory being approximated [1]. The discretization breaks Euclidean rotational invariance, the isometry group for Euclidean space, from SO(4) to chiral tesseractic symmetry ($[4,3,3]^+$ in Coxeter's notation [55]); lattice field theory cannot approximate Minkowski spacetime because there are no Lorentz boosts that preserve the lattice [56]. Additionally, momentum conservation is broken, but an analog of Bloch's theorem guarantees that momentum can change only by vectors in the reciprocal lattice, which for the standard setup is another hypercubic lattice with spacing $2\pi/a$ [56]. Of course, all of these effects vanish in the continuum limit at small a, and this is conjectured to recover the continuum field theory.

On the flipside, the finiteness of LQCD setups also causes special effects if the spacetime is smaller than around 6 fm [1]. Typically with cubic-prism setup, the imaginary-time axis is over twice as long as the spatial axes, so that the longer excited states do not wrap around this axis, and sometimes this axis is not wrapped around (topologically, $T^3 \times B^1$) [57]. The largest effect in simulations of finite systems is the wraparound of the pion field, which scales as $O(e^{-m_\pi L_s})$ and is the prime complication in simulating at the physical quark masses, where $1/m_\pi = 1.5$ fm; calculations are often run at heavier-than-physical quark masses, and then extrapolated to the physical point using ChEFT. This makes it particularly challenging to simulate QCD with very long or very short length scales. These include setups with multiple hadrons (where some effects scale polynomially rather than exponentially with L_s); bottom quarks (with $\sim 1/m_b = 47$ am, often extrapolated with a "heavy-quark effective theory" that mirrors ChEFT for the light quarks); or QED (which has infinite length scale, causing various technical issues).

3.3.1 Lattice gauge action

We seek to build an analog of the continuum action [56],

$$S = \int \mathcal{L}\, d^4x = \int d^4x \left[\overline{q}(i\not{D} - m)q - \frac{1}{4}\,\mathrm{Tr}(\tilde{F}_{\mu\nu}\tilde{F}^{\mu\nu})\right] \tag{46}$$

where traces are taken over the Lie algebra, not spacetime indices. It is conventional to set the Yang–Mills gauge field differently than presented above, under which the action vanishes as $g \to \infty$ [56]:[3]

$$A_\mu := g\tilde{A}_\mu \tag{47}$$

$$\begin{aligned} F_{\mu\nu} :=& \partial_\mu A_\nu - \partial_\nu A_\mu + i[A_\mu, A_\nu] \\ &= g\partial_\mu \tilde{A}_\nu - g\partial_\nu \tilde{A}_\mu + ig^2[\tilde{A}_\mu, \tilde{A}_\nu] \\ &= g\tilde{F}_{\mu\nu} \end{aligned} \tag{48}$$

$$D_\mu := \partial_\mu + iA_\mu = \partial_\mu + ig\tilde{A}_\mu = D_\mu \tag{49}$$

Under this convention, Eq. (46) becomes:

$$S = \int d^4x \left[\overline{q}(i\not{D} - m)q - \frac{1}{4g^2} \operatorname{Tr}(F_{\mu\nu}F^{\mu\nu}) \right] \tag{50}$$

The Wick rotation multiplies the action by $-i$, which inverts potentials:

$$S = \int d^4x \left[\overline{q}(\not{D} + m)q - \frac{1}{4g^2} \operatorname{Tr}(F_{\mu\nu}F^{\mu\nu}) \right] \tag{51}$$

The simplest and most common gauge action on the lattice is the Wilson action. In LQCD, the gluons live on links between adjacent sites, and instead of the Lie algebra degrees of freedom that make the gluon colors, we use the Lie group elements to ensure that the lattice theory does not converge to a discrete quotient of the gauge group [56]:

$$U_\mu := e^{iag\tilde{A}_\mu}. \tag{52}$$

Because the LQCD action is formulated a priori with unitary terms in the propagators, gauge invariance is preserved in LQCD [1], and no cancellative ghost terms are necessary! The measure

[3] This g is in the lattice renormalization. LQCD can be used to recover commonly-used g's in perturbative schemes, but there is no known way of recovering the lattice-scheme g from the perturbative ones [1].

of integration for the path integrals over the gauge group is the Haar measure [54].

To get the gauge-invariant Wilson loop, we can multiply consecutive links to construct a loop. The smallest loop in the lattice is a plaquette, a square 2-face in the lattice formed from four links parallel to arbitrary μ and ν axes. In this case, the Wilson loop is [56, 54]:

$$W_{\mu\nu}(x) = U_\mu(x)U_\nu(x+\hat{e}_\mu)U_\nu^\dagger(x+\hat{e}_\nu)U_\nu^\dagger(x), \tag{53}$$

where $\hat{e}_\alpha$ are the standard basis in $\mathbb{R}^4$. It is trivial to prove that $W_{\nu\mu} = W_{\mu\nu}^\dagger$ and that it describes the loop with opposite orientation. Then at order a^2,

$$\begin{aligned} W_{\mu\nu} &= \exp[ia^2 F_{\mu\nu} + ia^4(\partial_\mu^3 A_\nu - \partial_\nu^3 A_\mu) + O(a^6)] \\ &= 1 + ia^2 F_{\mu\nu} - \frac{1}{2}a^4 F_{\mu\nu}F_{\mu\nu} + O(a^6). \end{aligned} \tag{54}$$

The derivation of the expansion requires the BCH formula, $e^A e^B = \exp[A + B + [A,B]/2 + ...]$. Therefore,

$$\operatorname{Tr}(W_{\mu\nu} - 1) = \frac{1}{2}a^4 \operatorname{Tr}(F_{\mu\nu}F^{\mu\nu}) + O(a^6) \tag{55}$$

In these expressions, we can define the "inverse coupling" $\beta = 2N/g^2$ and then we can get the Wilson action by summing the real part of the Wilson loop over all plaquettes [54]:

$$\begin{aligned} S_g &= \frac{\beta}{2N}\sum_{x,\mu<\nu} \operatorname{Re}\operatorname{Tr}(1 - W_{\mu\nu}) = -\frac{\beta a^4}{4N}\sum_{x,\mu<\nu}\operatorname{Tr}(F_{\mu\nu}F^{\mu\nu}) \\ &\approx -\frac{\beta}{8N}\int d^4x \operatorname{Tr}(F_{\mu\nu}F^{\mu\nu}) = -\frac{1}{4g^2}\int d^4x \operatorname{Tr}(F_{\mu\nu}F^{\mu\nu}). \end{aligned} \tag{56}$$

Here, the extra 1/2 on the right-hand side of the $\approx$ occurs because the expression is summed according to Einstein convention, double-counting the spacetime indices on the left-hand side. The $1/N$ factor is used for the analysis of the large-N expansion for Yang–Mills, which extrapolates the asymptotic expansion at $N \to \infty$ to the physical N of the gauge theory [56]. Different analogs of the Wilson loop can be constructed by replacing the plaquettes with more complex loops; these can be chosen so that the NLO term in the Wilson loop, of order $F_{\mu\nu}D_\mu D^\mu F^{\mu\nu}$, cancels out [56].

3.3.2 Lattice fermions

The implementation of lattice fermions encounters technical issues due to crystal effects and the chiral anomaly [1]. The naïve lattice action begins with the quark term of the QCD Lagrangian and simply approximates the covariant derivative D_μ as the two-point finite difference [54],

$$D_\mu q(x) = \frac{1}{2a}\left[U_\mu(x)q(x+a\hat{e}_\mu) - U_\mu^\dagger(x-a\hat{e}_\mu)q(x-a\hat{e}_\mu)\right]. \tag{57}$$

In total, the naïve action is:

$$\begin{aligned} S_f &= a^4 \sum_{x,\mu} \overline{q}(x)\left\{m\psi + \frac{1}{2a}\left[U_\mu(x)q(x+a\hat{e}_\mu) - U_\mu^\dagger(x-a\hat{e}_\mu)q(x-a\hat{e}_\mu)\right]\right\} \\ &= a^4 \sum_{x,\mu} \overline{q}(m+\gamma^\mu D_\mu)q \approx \int d^4x \overline{q}(\not{D}+\mu)q. \end{aligned} \tag{58}$$

The dispersion relation in the crystal is necessarily periodic, and chiral anomalies do not exist [56]. As such, the Nielsen–Ninomiya theorem states that there are necessarily unphysical extra copies of each fermion species, called "tastes" or "doublers", in lattice theories that have exact chiral symmetry [1],

$$\left\{\gamma^5, D\right\} = 0 \tag{59}$$

For the naïve action in d dimensions, there are 2^d doublers. More precisely, the Nielsen–Ninomiya theorem guarantees equally many left-handed and right-handed fermions [56], so theories that violate P-symmetry, such as the weak force, cannot be implemented on the lattice. There is no known satisfactory means to implement chiral fermions on the lattice [56].

There are several methods for eliminating the doublers. The staggered fermion action modifies the spinor by labeling the sites with integer coordinates $x = a(n^1, n^2, n^3, n^4)$, then multiplies the fermion spinor at each site by gamma matrices:

$$\chi(x) = \prod_\mu (\gamma^\mu)^{n^\mu} q(x). \tag{60}$$

Since the Euclidean gamma matrices are their own inverses, this produces a lattice that alternates along each axis. The effect of this transformation is to distribute one spinor component to each site, reducing the number of doublers in $d = 4$ from sixteen to four. Despite this shortcoming, it is fast to compute, has the same $O(a^2)$ discretization error as the gauge and naive actions, and for some applications, the doubling can be compensated for using a mathematical trick known as rooting [1]. Also, the continuum limit of the staggered fermion is subtly different from the Dirac action: the EoM for staggered fermions is given by the Dirac–Kähler equation, which is expressed in differential forms [56].

The Wilson fermion action explicitly breaks chiral symmetry by adding the Laplacian term [56]:

$$S'_f = -a^3 r \sum_{x,\mu} \overline{q}(x)[q(x + a\hat{e}_\mu) - 2q(x) + q(x - a\hat{e}_\mu)] \approx ar \int d^4x \overline{q}\partial^\mu\partial_\mu q, \tag{61}$$

where r is a dimensionless parameter. It confers a mass of $O(1/a)$ to the unphysical doublers, so only the physical fermion remains in the continuum limit [1]. However, the Wilson action has $O(a)$ discretization errors; a modification called the clover fermion and a related isospin-breaking form called the twisted mass fermion (useful for theories with only up and down quarks, and can be extended also to strange and charm quarks with the baked-in mass difference) reduces the errors to $O(a^2)$. Wilson and related fermions are fast to compute, but not as fast as staggered fermions. This makes them practical for lattice QCD simulations, but the breaking of chiral symmetry requires fine-tuning to compensate unwanted chiral terms [56].

The most practical fermions, and the best candidate for implementation of chiral lattice fermions, are Ginsparg–Wilson fermions [56, 1]. They are Dirac operators that satisfy the chiral relation

$$\left\{\gamma^5, D\right\} = aD\gamma^5 D. \tag{62}$$

There are two mathematically related Ginsparg–Wilson fermions in common usage: domain-wall fermions and overlap fermions, with the domain-wall ones tending to be more computationally efficient. However, both methods are far less computationally efficient than Wilson fermions. Overlap

fermions use a Dirac operator that explicitly satisfies Eq. (62). Domain-wall fermions live in a space with a large fifth dimension, where the fermion mass is dependent on the fifth coordinate y; it is zero at a domain wall, and it approaches a large mass $\pm M$ at long distances from the wall. With this setup, energy states below the mass scale M are confined to a domain wall. In a setup with two domain walls and with the Wilson-fermion action to eliminate doublers, the left-handed and right-handed fermions are segregated to opposite walls.

3.3.3 Applications

Once the gauge action S_g and Dirac operator $\not{D}$ are chosen, the Euclidean partition function is [1]:

$$\begin{aligned} Z &= \int d^{\mathcal{N}}\mathbf{U} \left(\prod_q d\overline{q}\, dq \right) \exp\left\{ S_g(\mathbf{U}) - \sum_q \overline{q}[\not{D}(\mathbf{U}) + m_q]q \right\} \\ &= \int d^{\mathcal{N}}\mathbf{U} e^{-S_g(U)} \prod_q \det[\not{D}(\mathbf{U}) + m_q] \end{aligned} \tag{63}$$

where U are the $\mathcal{N} = N_s^3 \times N_t \times (N^2 - 1) \times 4$ unitary degrees of freedom. By Wick's theorem, the correlation functions

$$\langle \mathcal{A}(U, q, \overline{q}) \rangle = \frac{1}{Z} \int d^{\mathcal{N}}\mathbf{U} \left(\prod_q d\overline{q}\, dq \right) \mathcal{A} \exp\left\{ S_g(\mathbf{U}) - \sum_q \overline{q}[\not{D}(\mathbf{U}) + m_q]q \right\} \tag{64}$$

similarly have the fermion fields integrated out as the fermion determinant times some propagator factors $K_q = (\not{D} + m_q)^{-1}$. Quantities can then be computed using Monte Carlo importance sampling, with statistical error inversely proportional to the square root of the number of evaluations [1]. Various methods exist to avoid evaluating the fermion determinant (of complexity $O[(N_s^3 \times N_t)^3]$), but all methods require successive inversions of $(\not{D} + m_q)$. Another difficulty with light quarks, besides the aforementioned finite-size pion effects, is that the smallest eigenvalue of the fermion operator is $O(m_q)$, and the cost of the inversion is inversely proportional to a power of this eigenvalue. At small lattice spacings, "autocorrelations" between successive Markov-chain Monte Carlo samples, especially in global topological charges, can also affect statistical uncertainties and

dramatically increase the sampling time [57].

The most obvious application, of course, is to interpret Z as a literal partition function, with temperature $T = 1/L_t$ and volume $V = L_s^3$. However, the fermion sign problem makes the Z integral oscillatory, and therefore exponentially hard to evaluate at $\mu_q \neq 0$; the usual workaround is to use an imaginary μ_q (where Z is periodic with period $2\pi iT/3$ and does not have a sign problem) and use analytic continuation to derive a Taylor expansion in finite μ_q [13]. Myriad other relevant low-energy QCD quantities have been calculated, including the quark masses, the relation between the lattice and $\overline{\text{MS}}$ renormalizations of α_s, various weak force-related factors such as f_π and the $K \to \pi\ell\nu$ form factor, and properties of the nucleons such as the $s\bar{s}$ and $c\bar{c}$ condensates [1, 57]. Of particular remarkability is computation of the muon magnetic moment due to contributions from virtual hadrons, needed to isolate a contribution from new physics: The final results from the Muon g-2 experiment at Fermilab, reported in June 2025, are within 1σ of the Standard Model estimate obtained from the averaged LQCD results [58].

3.4 Hadrons

Due to color confinement, quarks combine into "white" combinations with no net color charge. There are two basic categories of color-neutral hadrons: opposite-colored quark-antiquark pairs called mesons, and triplets of red, green, and blue quarks called baryons.

In the general case, there is an approximate SU(3) flavor symmetry between the three light quarks, with the down quark being slightly heaver than the up, and the strange quark being heavier than the other two.[4]

3.4.1 Mesons

Mesons have one quark and one antiquark and zero net baryon number, so they can self-annihilate. This means that they are all unstable, with lifetimes on the order of 10^{-8} s for the weakly decaying

[4] Due to the much greater mass of the charm quark, there is no $\text{SU}(4)_f$ symmetry. However, the charmed hadrons can be predicted from $\text{SU}(4)_f$, and bottom hadrons from $\text{SU}(5)_f$. The top quark decays too quickly (mainly to W^+b) to form hadrons [1].

charged pions ($\pi^{\pm}$) and the charged kaons ($K^{\pm}$); and most of the rest having much shorter lifetimes, which can decay electromagnetically (e.g. π^0) or strongly (e.g. ω, ρ) [1].

The parity operator P is defined on Dirac states as [3]:

$$P\psi(t,\mathbf{x})P^{\dagger} = \eta_P \gamma^0 \psi(t,-\mathbf{x}). \tag{65}$$

The presence of the γ^0 matrix implies that fermions and antifermions have opposite parity. By convention, each quark has positive parity $P = 1$, and each antiquark has parity $P = -1$ [1]. Additionally, the parity of a spherically symmetric wave function is -1^L, where L is the angular momentum of the spatial state, so the total parity of a $q\overline{q}$ state is $(-1)^{L+1}$ [1]. Together with the spin S, which may be 0 or 1, the mesons can then be classified by J^P; the simplest cases are named as followed [1]:

- For $L = 0$, the possible J^P states are 0^- (pseudoscalar) and 1^- (pseudovector).
- For $L = 1$, the possible J^P states are 0^+ (scalar), 1^+ (pseudovector), and 2^+ (tensor).

For the $\mathrm{SU}(3)_f$ symmetry, we find that the nine $q\overline{q}$ states for a given J^P form an octet and a singlet,

$$\mathbf{3} \otimes \overline{\mathbf{3}} = \mathbf{8} \oplus \mathbf{1}. \tag{66}$$

Thus, in each $q\overline{q}$ light-quark nonet, there are three states with $T = 1$ and no strange quarks, one of which is neutral; four states with $T = 1/2$ and $\mathcal{S} = \pm 1$; one neutral octet state with $T = 0$; and the singlet, which is also neutral with $T = 0$ and heavier than the others due to a $U(1)_A$ chiral anomaly in QCD (Fig. 2) [3]. The octet pseudoscalars become massless in the limit of massless quarks [50], but the singlet does not [59]. Table 2 lists the pseudoscalar and vector nonets.

The neutral $T = 1$ state, which we will generically denote a^0, is very close to the ideal flavor wavefunction,

$$|a^0\rangle = \frac{|u\overline{u}\rangle - |d\overline{d}\rangle}{\sqrt{2}}. \tag{67}$$

In the chiral limit, the neutral octet f_8 and singlet f_1 states have flavor wavefunctions orthogonal

Table 2: List of ground-state pseudoscalar and vector mesons [1]. Some lifetimes were reported as Breit–Wigner resonance widths, which have been converted to mean lifetimes via $\tau = \hbar/\Gamma$. Quark contents are approximate due to mixing of the neutral states and of the K^0 states. The ρ and K^* meson masses are for e^+e^- collisions and $\tau^\pm$ decays, and are somewhat lower in hadronic interactions.

Baryon	Quarks	Mass (MeV)	Q	Isospin		$\mathcal{S}$	Mean lifetime (s)
				T	T_3		
π^+	$u\overline{d}$	139.57039(18)	+1	1	+1	0	$2.6033(5)\times10^{-8}$
π^0	$\frac{u\overline{u}-d\overline{d}}{\sqrt{2}}$	134.9768(5)	0	1	0	0	$8.43(13)\times10^{-17}$
π^-	$d\overline{u}$	139.57039(18)	−1	1	−1	0	$2.6033(5)\times10^{-8}$
K^+	$u\overline{s}$	493.677(15)	+1	1/2	+1/2	+1	$1.2380(20)\times10^{-8}$
K^0_S	$\frac{d\overline{s}-s\overline{d}}{\sqrt{2}}$	497.611(13)	0	1/2	$\frac{\lvert-1/2\rangle-\lvert+1/2\rangle}{\sqrt{2}}$	$\frac{\lvert+1\rangle-\lvert-1\rangle}{\sqrt{2}}$	$8.954(4)\times10^{-11}$
K^0_L	$\frac{d\overline{s}+s\overline{d}}{\sqrt{2}}$	497.611(13)	0	1/2	$\frac{\lvert-1/2\rangle+\lvert+1/2\rangle}{\sqrt{2}}$	$\frac{\lvert+1\rangle+\lvert-1\rangle}{\sqrt{2}}$	$5.116(21)\times10^{-8}$
K^-	$s\overline{u}$	493.677(15)	−1	1/2	−1/2	−1	$1.2380(20)\times10^{-8}$
η	$\frac{u\overline{u}+d\overline{d}-2s\overline{s}}{\sqrt{6}}$	547.862(17)	0	0	0	0	$5.02(19)\times10^{-19}$
η'	$\frac{u\overline{u}+d\overline{d}+s\overline{s}}{\sqrt{3}}$	957.78(6)	0	0	0	0	$3.50(11)\times10^{-21}$
ρ^+	$u\overline{d}$	775.11(34)	+1	1	+1	0	$4.41(2)\times10^{-24}$
ρ^0	$\frac{u\overline{u}-d\overline{d}}{\sqrt{2}}$	775.26(23)	0	1	0	0	$4.47(2)\times10^{-24}$
ρ^-	$d\overline{u}$	775.11(34)	−1	1	−1	0	$4.41(2)\times10^{-24}$
K^{*+}	$u\overline{s}$	895.5(8)	+1	1/2	+1/2	+1	$1.42(4)\times10^{-23}$
K^{*0}	$d\overline{s}$	895.55(20)	0	1/2	−1/2	+1	$1.39(1)\times10^{-23}$
$\overline{K}^{*0}$	$s\overline{d}$	895.55(20)	0	1/2	+1/2	−1	$1.39(1)\times10^{-23}$
K^{*+}	$s\overline{u}$	895.5(8)	−1	1/2	−1/2	−1	$1.42(4)\times10^{-23}$
ω	$\frac{u\overline{d}+d\overline{u}}{\sqrt{2}}$	782.66(13)	0	0	0	0	$7.58(11)\times10^{-23}$
ϕ	$s\overline{s}$	1019.461(16)	0	0	0	0	$1.549(5)\times10^{-22}$

to a^0, with the states

$$|f_8\rangle = \frac{|u\overline{u}\rangle + |d\overline{d}\rangle - 2|s\overline{s}\rangle}{\sqrt{6}} \tag{68}$$

$$|f_1\rangle = \frac{|u\overline{u}\rangle + |d\overline{d}\rangle + |s\overline{s}\rangle}{\sqrt{3}} \tag{69}$$

which correspond to the two traceless generators of SU(3) in the adjoint representation. However, the nonzero and distinct masses of the light quarks cause the states to mix into the physical f and

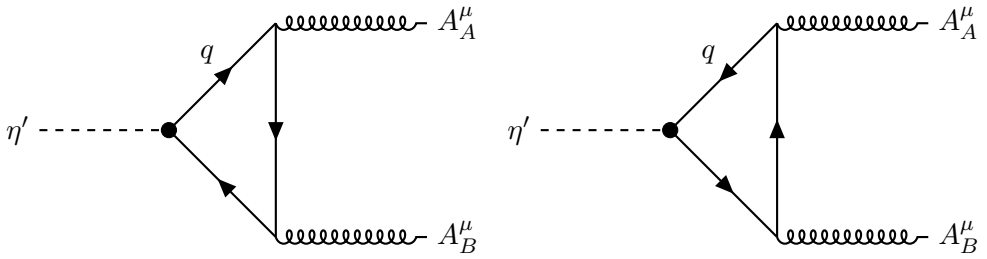

Figure 2: Feynman diagrams which cause the QCD anomaly for the $\mathrm{SU}(3)_f$ singlet, and particularly the higher mass of the η' compared to the η [3].

f' states [1]:

$$\begin{pmatrix} f \\ f' \end{pmatrix} = \begin{pmatrix} \cos\theta & -\sin\theta \\ \sin\theta & \cos\theta \end{pmatrix} \begin{pmatrix} f_8 \\ f_1 \end{pmatrix}. \tag{70}$$

The actual mixing angle for pseudoscalars, as predicted from LQCD, is $\theta_P = -14.1(28)^\circ$ [60]; the state closer to $|f_8\rangle$ is the η and the state closer to $|f_1\rangle$ is the η'. If $\theta = \arctan(1/\sqrt{2}) \approx 35.3^\circ$, then the $u\overline{u}/d\overline{d}$ and $s\overline{s}$ states decouple completely and then $|f\rangle = (|u\overline{u}\rangle + |d\overline{d}\rangle)/\sqrt{2}$ and $|f'\rangle$ is a pure $s\overline{s}$ state. The mixing angle for vectors, as estimated from the meson masses, is $\theta_V \approx 36.5^\circ$, so the ω meson is nearly pure $u\overline{u}/d\overline{d}$ and the ϕ is nearly pure $s\overline{s}$ [1].

Additionally, there is a mixing of the $d\overline{s}$ (K^0) and $s\overline{d}$ ($\overline{K}^0$) states due to the diagram in Fig. 3, which shifts them to the eigenstates K_L^0 and K_S^0. In the limit of no CP violation, K_L^0 is CP-even and K_S^0 is CP-odd; CP-violating effects in the weak sector cause a slight mixing of these eigenstates [3], and a mass difference of $m_L - m_S = 3.484(6) \times 10^{-12}$ MeV [1].

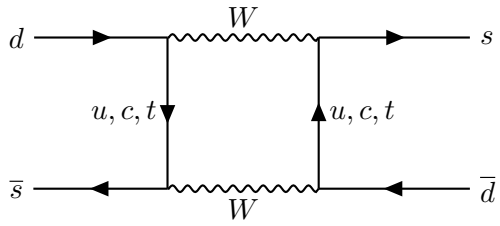

Figure 3: Leading-order Feynman diagram which causes K^0–$\overline{K}^0$ mixing, known as the GIM mechanism [3].

The scalars and pseudovectors are not as well-understood; some of these states are probably

$q\overline{q}$ states, while others could be exotic non-$q\overline{q}$ meson states, such as tetraquarks ($qq\overline{qq}$ states), two-meson molecular states, and states that include real gluons; it is likely that certain states are mixtures of these possibilities [1]. Below 1 GeV, four meson resonances are established experimentally [1]: the $f_0(500)$ (also called σ), the kaon-like $K_0(700)$ (also called κ), the $f_0(980)$, and the $a_0(980)$ isospin triplet (also called δ [61]). There is consensus that these states form a 0^+ nonet, but it is unclear if they are the ground-state $q\overline{q}$ scalars, tetraquarks, or meson molecules [1]. The classification of light-quark scalars above this threshold is unclear — there is a nonet that includes the κ-like $K_0(1430)$, the δ-like $a_0(1450)$, and two of three $T = 0$ resonances ($f_0(1370)$, $f_0(1500)$, and $f_0(1710)$); one of the f_0 resonances is probably the lightest glueball with two gluons, or the three could be mixtures of $q\overline{q}$ and gg states [1].

Table 3: List of mesons in the light scalar nonet [1]. All lifetimes were reported as Breit–Wigner resonance widths, which have been converted to mean lifetimes via $\tau = \hbar/\Gamma$.

Meson	Alt. names	Mass (MeV)	Q	J^P	Isospin		S	Mean lifetime (s)
					T	T_3		
$f_0(500)$	σ	600±200	0	0^+	0	0	0	$1.5^{+5.1}_{-0.6}\times10^{-24}$
$K_0^+(700)$	κ^+	838±11	+1	0^+	1/2	+1/2	+1	$1.422(83)\times10^{-24}$
$K_0^0(700)$	κ^0	838±11	0	0^+	1/2	−1/2	+1	$1.422(83)\times10^{-24}$
$\overline{K}_0^0(700)$	$\overline{\kappa}^0$	838±11	0	0^+	1/2	+1/2	−1	$1.422(83)\times10^{-24}$
$K_0^-(700)$	κ^-	838±11	−1	0^+	1/2	−1/2	−1	$1.422(83)\times10^{-24}$
$a_0^+(980)$	δ^+	980±20	+1	0^+	1	+1	0	$8.8^{+4.4}_{-2.2}\times10^{-24}$
$a_0^0(980)$	δ^0	980±20	0	0^+	1	0	0	$8.8^{+4.4}_{-2.2}\times10^{-24}$
$a_0^-(980)$	δ^-	980±20	−1	0^+	1	−1	0	$8.8^{+4.4}_{-2.2}\times10^{-24}$
$f_0(980)$	σ_s, σ^*, ζ	990±20	0	0^+	0	0	0	$1.2^{+5.4}_{-0.5}\times10^{-23}$

For pseudovectors, there are two nonets in the range 1–2 GeV: one with negative C-parity ($h_1(1170)$, $b_1(1235)$, K_{1B}, $h_1(1415)$), the other with positive C-parity ($a_1(1260)$, $f_1(1285)$, K_{1A}, and either $f_1(1420)$ or $f_1(1510)$); the K_{1A} and K_{1B} states mix with a mixing angle of about $-35°$ to give the $K_1(1270)$ and $K_1(1400)$ [1].

3.4.2 Baryons

Baryons, unlike mesons, can decay only to lighter baryons because of their net baryon number 1 (or −1 for antibaryons); this also means that the lightest baryon, the proton (p), is stable in the

Standard Model. The proton and the slightly heavier neutron (n) constitute the bulk of ordinary matter by mass, respectively weighing about 1836 and 1839 times an electron [62]. There are very tight empirical constraints on baryon number-violating processes, such as $p \to e^+\pi^0$ or neutron self-annihilation, predicted by GUTs [1].

The $\mathrm{SU}(3)_f$ baryon multiplet generically includes a decuplet, two octets, and a singlet [1]:

$$\mathbf{3}^{\otimes 3} = \mathbf{10} \oplus \mathbf{8}_1 \oplus \mathbf{8}_2 \oplus \mathbf{1} \tag{71}$$

With low spin–orbit coupling, this can be extended to SU(6) spin–flavor symmetry, expanding the baryon multiplets to [1]:

$$\begin{aligned} \mathbf{6}^{\otimes 3} &= \mathbf{56} \oplus \mathbf{70}_1 \oplus \mathbf{70}_2 \oplus \mathbf{20} \\ &= ({}^4\mathbf{10} \oplus {}^2\mathbf{8}) \oplus ({}^2\mathbf{10} \oplus {}^4\mathbf{8} \oplus {}^2\mathbf{8} \oplus {}^2\mathbf{1}) \oplus ({}^2\mathbf{10} \oplus {}^4\mathbf{8} \oplus {}^2\mathbf{8} \oplus {}^2\mathbf{1}) \oplus ({}^2\mathbf{8} \oplus {}^4\mathbf{1}) \end{aligned} \tag{72}$$

where on the second line each pair of brackets separates a multiplet in the first line. However, not all of these states actually exist, due to the requirement of Fermi statistics that the wavefunction of identical fermions be antisymmetric under exchange [1]. In particular, in the ground state where all quarks have angular momentum $l = 0$, we get the following restriction:

Theorem 1. *It is impossible for two quarks with the same flavor and spatial wavefunction to coexist in a singlet spin state.*

Proof. The total wave function of two identical quarks must be antisymmetric. As such, the color wavefunction is always antisymmetric. The spatial wavefunction needs to be symmetric in order for the fermions to coexist in this state. If we assume without loss of generality that the pair (called a diquark) is antiblue, then the combined wavefunction is

$$|\psi\rangle = \big|\psi_q(\mathbf{x})\psi_q(\mathbf{x}') + \psi_q(\mathbf{x}')\psi_q(\mathbf{x})\big\rangle \left(\frac{|q_R q_G\rangle - |q_G q_R\rangle}{\sqrt{2}}\right) \left(\frac{\big|q^\uparrow q^\downarrow\big\rangle - \big|q^\uparrow q^\downarrow\big\rangle}{\sqrt{2}}\right), \tag{73}$$

which is symmetric under exchange of the quarks and therefore cancels itself out under Fermi

statistics. □

Using this restriction, we can infer the following properties for "ground state" baryons, where all quarks have orbital angular momentum $l = 0$:

- A baryon with one flavor of quark and $L = 0$ must have all spins aligned, for a total spin of $J^P = 3/2^+$.
- For a baryon with two flavors of quarks, the two quarks with the same flavor have a triplet spin state, which allows two baryons that differ in the spin of the third quark: one with spin $1/2^+$, the other with spin $3/2^+$.
- A baryon with three flavors of quarks has one state with spin 3/2+ and two states with spin 1/2+, the latter differing in how two of the three quarks are symmetrized.

For the three light quarks, there exist 10 different flavor combinations, and this produces two groups of ground-state baryons in the $\mathrm{SU}(3)_f$ gauge: an $\mathbf{8}_1$ octet with spin $1/2^+$, and a **10** decuplet with spin $3/2^+$; the other octet and the singlet (an extra Λ baryon) are excluded by Fermi statistics. The ground-state baryons correspond to the **56** multiplet in the $\mathrm{SU}(6)_{sf}$ gauge [1]. The properties of these baryons are listed in Table 4.

3.4.3 Chiral effective field theory (ChEFT)

ChEFT is a non-renormalizable description of hadronic interactions below $\sim \Lambda_{\mathrm{QCD}}$ in terms of hadrons that interact by exchange of virtual mesons. Such a description is dominated by the pions, which are the only hadrons with mass below this scale [50].

If the masses of the up and down quarks are equal, then the $\mathrm{SU}(2)_f$ symmetry decomposes as $\mathbf{2} \otimes \overline{\mathbf{2}} = \mathbf{3} \oplus \mathbf{1}$ and gives three pions and an isospin-0 particle that, due to the low mass of the strange quark, becomes the η meson [50]. Therefore, the three pions are pseudo-Goldstone bosons for the breaking of chiral symmetry (which can also be spontaneous), with the explicit breaking by

Table 4: List of ground-state octet and decuplet baryons [1]. Some lifetimes were reported as Breit–Wigner resonance widths, which have been converted to mean lifetimes via $\tau = \hbar/\Gamma$.

Baryon	Quarks	Mass (MeV)	Q	J^P	Isospin		S	Mean lifetime (s)
					T	T_3		
p (N^+)	uud	938.27208816(29)	+1	$1/2^+$	1/2	+1/2	0	$> 2.8{\times}10^{37}$
n (N^0)	udd	939.5654205(5)	0	$1/2^+$	1/2	−1/2	0	$8.784(5){\times}10^{2}$
Λ	uds	1115.683(6)	0	$1/2^+$	0	0	−1	$2.617(10){\times}10^{-10}$
Σ^+	uus	1189.37(7)	+1	$1/2^+$	1	+1	−1	$8.018(26){\times}10^{-11}$
Σ^0	uds	1192.642(24)	0	$1/2^+$	1	0	−1	$7.4(7){\times}10^{-20}$
Σ^-	dds	1197.449(29)	−1	$1/2^+$	1	−1	−1	$1.479(11){\times}10^{-10}$
Ξ^0	uss	1314.86(20)	0	$1/2^+$	1/2	+1/2	−2	$2.90(9){\times}10^{-10}$
Ξ^-	dss	1321.71(7)	−1	$1/2^+$	1/2	−1/2	−2	$1.639(15){\times}10^{-10}$
Δ^{++}	uuu	1232.(2)	+2	$3/2^+$	3/2	+3/2	0	$5.63(14){\times}10^{-24}$
Δ^+	uud	1232.(2)	+1	$3/2^+$	3/2	+1/2	0	$5.63(14){\times}10^{-24}$
Δ^0	udd	1232.(2)	0	$3/2^+$	3/2	−1/2	0	$5.63(14){\times}10^{-24}$
Δ^-	ddd	1232.(2)	−1	$3/2^+$	3/2	−3/2	0	$5.63(14){\times}10^{-24}$
Σ^{*+}	uus	1382.83(34)	+1	$3/2^+$	1	+1	−1	$1.818(35){\times}10^{-23}$
Σ^{*0}	uds	1383.7(10)	0	$3/2^+$	1	0	−1	$1.83(25){\times}10^{-23}$
Σ^{*-}	dds	1387.2(5)	−1	$3/2^+$	1	−1	−1	$1.671(89){\times}10^{-23}$
Ξ^{*0}	uss	1531.80(32)	0	$3/2^+$	1/2	+1/2	−2	$7.2(4){\times}10^{-23}$
Ξ^{*-}	dss	1535.0(6)	−1	$3/2^+$	1/2	−1/2	−2	$6.6^{+1.6}_{-1.0}{\times}10^{-23}$
Ω	sss	1672.45(29)	−1	$3/2^+$	0	0	−3	$8.21(11){\times}10^{-11}$

the nonzero quark masses conferring a pion mass

$$m_\pi \approx \sqrt{(m_u + m_d)\frac{\Lambda_m^3}{F_\pi^2}} \tag{74}$$

where $F_\pi = 92$ MeV is a scale related to the weak decay of the charged pion, and $\Lambda_m \approx 289$ MeV is a new scale from the symmetry-breaking term; the ≈ 5 MeV mass difference between the $\pi^\pm$ and π^0 is mostly due to the Coulomb energy of the former. At the cutoff scale of $\Lambda_\chi \approx 4\pi F_\pi = 1160$ MeV, ChEFT includes two quartic vertices that couple pions together, which can interact with each other through two vertices of order 4: one that includes two derivatives, and one that includes a factor of F_π^{-2} [50].

With an averaged mass of $m_N = 939$ MeV, the nucleons (and other baryons) are too heavy to occur as degrees of freedom in ChEFT. Nonetheless, if there are no antibaryons, then it is possible to include the nucleons as non-relativistic particles. The coupling constant of the lowest-order (LO)

$NN\pi$ vertex can be estimated as

$$g_{\pi N} = \frac{g_A m_N}{F_\pi}, \tag{75}$$

where $g_A = 1.25$ is related to the weak decay of a free neutron, and therefore $g_{\pi N} \approx 12.8$ [50]. This vertex, and the two pion–pion quartic vertices, are shown in Fig. 4.

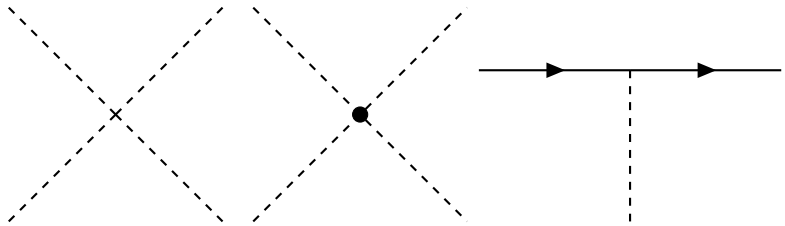

Figure 4: From left to right: Feynman diagrams that represent the two-pion interaction with two derivatives, the interaction with m_π^2, and the simplest pion–nucleon vertex in ChEFT.

In principle, ChEFT has an infinite expansion of coefficients that can be measured experimentally or using LQCD [50], with the LO vertices being the aforementioned $NN\pi$, π^4, and $\pi^2(\partial\pi)^2$ vertices:

$$\begin{aligned}\mathcal{L} &= \mathcal{L}_\pi + \mathcal{L}_N + \mathcal{L}_{\pi N} \\ &= -F_\pi^2 \Lambda_\chi^2 \sum_{m=1}^{\infty} \sum_{n=0}^{\infty} c_{mn} \left(\frac{\sqrt{\partial \boldsymbol{\pi}^2}}{\Lambda_\chi F_\pi} \right)^{2m} \left(\frac{\boldsymbol{\pi}}{F_\pi} \right)^{2n} + m_\pi^2 F_\pi^2 \cos \frac{\sqrt{\boldsymbol{\pi} \cdot \boldsymbol{\pi}}}{F_\pi} + O(\Delta m_\pi) \\ &\quad - \overline{N}(\not{\partial} + m_N) N - \frac{i g_A}{2F_\pi} \overline{N} (\gamma^\mu \gamma^5 \boldsymbol{\tau} \cdot \partial_\mu \boldsymbol{\pi}) N - \frac{i}{2F_\pi^2} (\overline{N} \gamma^\mu \boldsymbol{\tau} N) \cdot (\boldsymbol{\pi} \times \partial_\mu \boldsymbol{\pi}) + \ldots + O(\Delta m_N)\end{aligned} \tag{76}$$

Similar logic within $\mathrm{SU}(3)_f$ can describe the kaons and η meson as five additional pseudo-Goldstone bosons (with the η' left over) —these are still well below Λ_χ, but with $m_s/\Lambda_{\mathrm{QCD}} \approx 0.38$, the ChEFT approximation is less accurate for hadrons containing strange quarks [50].

4 Finite nuclei

Protons and neutrons make up the bulk of ordinary matter, forming the atomic nucleus. Nucleons can join into finite nuclei due to a residual strong force which, according to ChEFT, includes an

attractive two-body force due to exchange of pions governed by the Yukawa potential

$$V(r) = -\frac{g_\pi^2}{4\pi}\frac{e^{-m_\pi r}}{r}, \tag{77}$$

additional attractive Yukawa forces by the σ and δ scalars, and repulsive Yukawa forces due to the ρ and ω mesons; the interactions are dependent on spin and isospin [63, 64].

4.1 Nuclear drip lines

The table of nuclides (Fig. 5) includes all nuclei sorted by atomic number (Z) and neutron number (N), generally denoted by the shorthand ${}^{A}Z$ where $A = Z + N$ is the mass number of the nucleus (equivalent to baryon number), and Z is the chemical symbol of the element (e.g. C for $Z = 6$). It is bounded between the proton and neutron drip lines, beyond which it is no longer energetically favorable to add more protons or neutrons, respectively — they occur because, as fermions, adding a proton or neutron places it into the lowest available energy state, and when there are enough protons or neutrons, there are no more available bound states [65]. The location of the proton drip line is known for most elements up to neptunium, including all of the odd-Z elements in this range [66], but the neutron drip line is known only up to $N = 29$ [67]. The proton drip line can be reached using the fusion–evaporation process, where two lighter nuclei are collided, and several neutrons are ejected while the combined compound nucleus settles into its ground state [68]. In contrast, neutron-rich nuclei, such as ^{60}Ca, can be produced in fragmentation of heavier nuclei [69], but known processes that can synthesize neutron-rich nuclei are expected to reach the neutron drip line only for $N \lesssim 60$ and shortly after the $N = 82$ shell closure; the approximate location of the neutron drip line is well-known from models, with an expected minimum proton fraction of $Z/A \sim 0.30$ at large N, but little is known about the properties of neutron-rich nuclei; understanding this region is crucial to the r-process of stellar nucleosynthesis [68].

Most nuclei beyond the drip lines have very short lifetimes, but for protons there is a large Coulomb barrier at high Z that inhibits proton emission for nuclei just beyond the proton drip

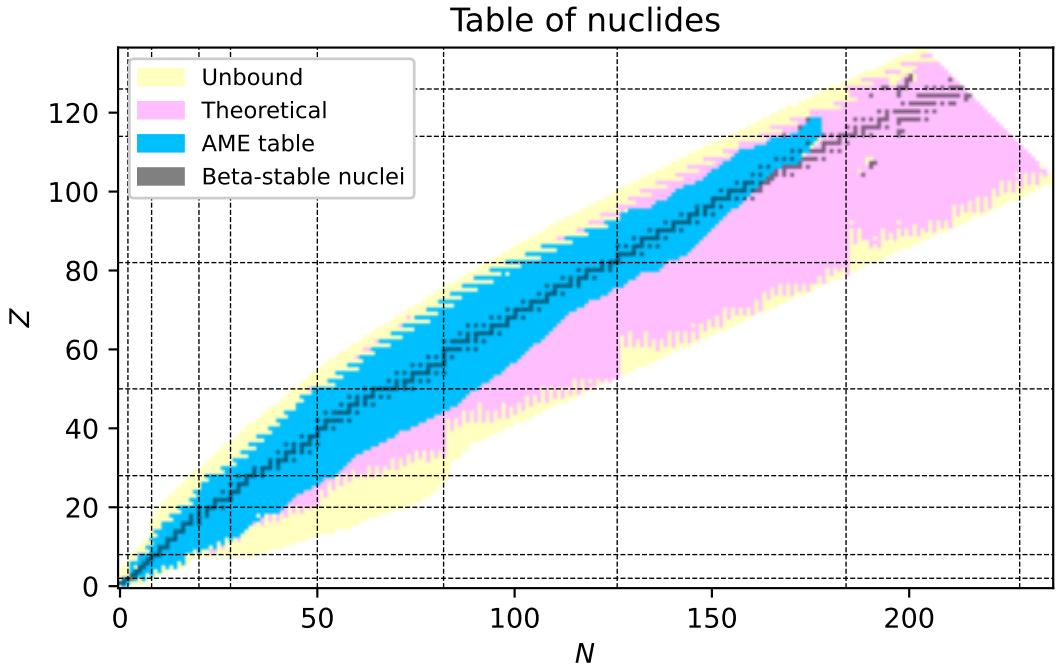

Figure 5: The table of nuclides between the drip lines up to $A = 339$, including the AME20 table [4] and theoretical predictions from the FRDM12 model [5].

line, and results in longer lifetimes for these nuclei [68]; for example, the half-life of ^{11}N is $5.85(7) \times 10^{-22}$ s, while that of ^{155}Ta is $3.2(13) \times 10^{-3}$ s [70] Both proton and neutron emission are also inhibited by an angular-momentum barrier, which may result in long-lived post-neutron-drip nuclei as well [68].

4.2 Nuclear binding and β-stability

When mass per nucleon is plotted for each nucleus in the table of nuclides, there is a long valley that bottoms out at ^{56}Fe [71] (Fig. 6);[5] lighter nuclei tend to release energy upon fusion, while heavier ones tend to release energy upon fission. After $A = 208$ and for some very proton-rich nuclei above $A = 150$, nuclei become increasingly unstable toward α decay[6] (emission of a tightly-bound ^{4}He cluster) and then spontaneous fission [73]. Additionally, along each A the nuclear masses (including

[5]Although for binding energy, the energy needed to separate an atom into hydrogen atoms and neutrons, the global minimum is attained at ^{62}Ni [71] at $-8.7945556(68)$ MeV/nucleon [4].

[6]In theory, α decay is possible for most naturally-occurring nuclei with $A \geq 142$, but predicted half-lives for most of them are far longer than can be detected by experiment [72].

the electron cloud) form a U-shaped profile (Fig. 7), with weak β decay processes

$$\begin{aligned} {}^{A}Z &\rightarrow {}^{A}(Z+1) + e^{-} + \overline{\nu}_e && (\beta^{-} \text{ decay}) \\ {}^{A}Z + e^{-} &\rightarrow {}^{A}(Z-1) + \nu_e && (\text{electron capture}) \\ {}^{A}Z &\rightarrow {}^{A}(Z+1) + e^{-} + \overline{\nu}_e && (\beta^{+} \text{ decay}) \end{aligned} \tag{78}$$

tending to cause nuclei to move toward the bottom of the valley, known as the line of β-stability [73].

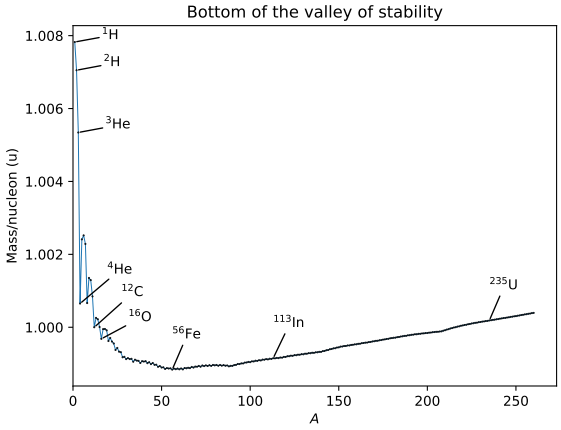

Figure 6: Mass per nucleon for the known β-stable nuclei, as calculated from the AME20 empirical mass table [4] up to $A = 260$, following the center of the valley of stability.

4.3 Nuclear shell states and pairing

Like electrons in atoms, nucleons in atomic nuclei organize into quantized shell bands, which can be further broken up into subshell states that correspond to the spatial wavefunctions; there are separate sets of shells for protons and for neutrons. This results in so-called magic numbers of protons or neutrons, analogous to the closed electron shells of noble gases, which have closed nuclear shells and are especially stable[74]. For spherical nuclei far from the drip lines, these include $Z = 2$, 8, 20, 28, 50, and 82 for protons; and $N = 2$, 8, 20, 28, 50, 82, and 126 for neutrons. The next neutron magic numbers are expected to be $N = 184$ and 228. The next proton magic numbers

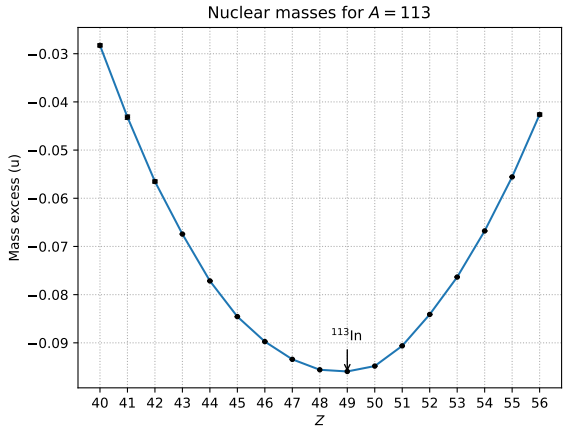

Figure 7: Mass excess, defined as the mass in atomic mass units minus A, for the $A = 113$ isobar series within AME20 [4]. For this series, the unique β-stable isobar is ^{113}In.

are not well-constrained either empirically or theoretically [75, 76], but it is likely $Z = 114$ or 120, which corresponds to the expected location of the long-sought island of stability near the probably doubly magic ^{298}Fl. The next magic number is probably $Z = 126$, and a third island of stability is expected to lie at the doubly-magic ^{472}164.

Nuclei near the magic numbers tend to be spherical, except for some nuclei very far from the line of β-stability, such as the prolate ^{32}Mg and ^{40}Mg [77, 78]. In contrast, most nuclei far from the magic numbers are prolate spheroids (elongated along one axis) [79], like ^{238}U. The tendency of actinides to undergo nuclear fission is due to their prolate ground states, which elongates and breaks apart during the nuclear fission process [80]. Nuclei just below magic numbers, such as ^{197}Au, tend to be oblate (flattened along one axis) [81]. The nuclear shells shift for deformed, ellipsoidal nuclei, and this can result in alternative magic numbers in regions with deformed nuclei — the nucleus ^{270}Hs is one empirically known example [82]. Nuclei near and beyond the first island of stability are expected to become extremely deformed due to the extreme Coulomb forces of the protons, with some nuclei becoming hollow or partially hollow bubbles [83], and other nuclei becoming donut-shaped [84].

In nuclei, it is energetically more stable for two nucleons of the same type to enter a singlet spin state in the same subshell, where the attractive nuclear force brings them into a lower energy

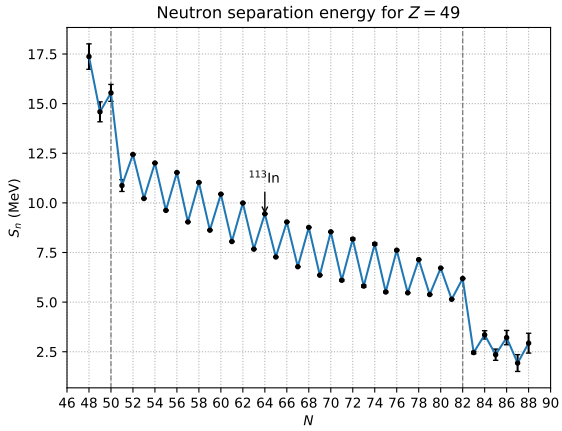

Figure 8: Energy needed to remove one neutron for the indium isotope series from ^{97}In to ^{137}In, as calculated from AME20 [4]. The odd-N and even-N sub-series are staggered due to nucleon pairing, and there are sharp drops after the neutron shell closures at $N = 50$ and 82.

state than if they were in different subshells [85]. For this reason, nuclei with even Z and even N tend to be more stable than those with odd A or with odd Z and odd N [85]; all nuclei with even Z and even N have $J^P = 0^+$ [70]; and bulk nuclear matter is a superfluid at low temperatures [35]. The pairing gap, which is the effective binding energy of these nucleon pairs [86], is well-described by the BCS model for most nuclei that are far from the drip lines, and all bound nuclei can be described by the more sophisticated Lipkin–Nogami model [87, 85]. Fig. 8 shows the combination of pairing and nuclear shell effects in the energy needed to remove one neutron, akin to the sudden drop in ionization energy after each noble gas.

5 QCD phase diagram

Bulk QCD matter refers to phases that contain quark and gluon degrees of freedom, either as a deconfined liquid (often called quark matter); as large masses of hadrons that resemble infinite nuclei (hadronic matter); or as mixtures of these two states (quarkyonic or baryquark matter). There are a number of situations in which QCD matter can occur in the real world, such as collisions of heavy atomic nuclei [8], core-collapse SNe, and NSs that condense during some types of core-collapse SNe [45][44]. The properties of QCD matter are related to the properties of finite nuclei, such as the

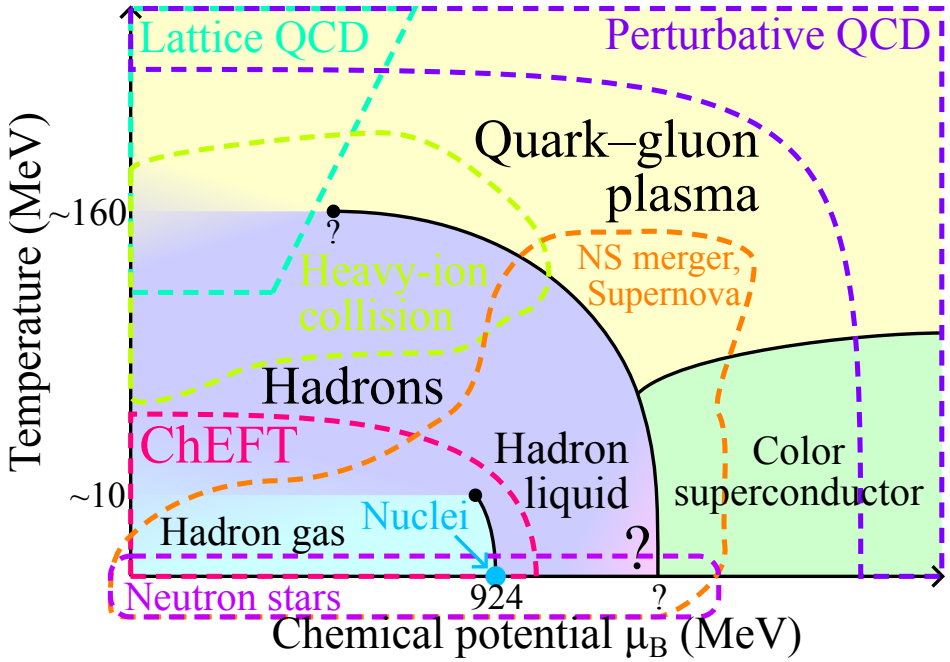

Figure 9: The QCD phase diagram with labels, including regions where the EoS is well-constrained [6, 7, 8, 9] and where interesting phenomena such as NSs and SNe occur [10, 11]. Not to scale.

superfluid nature of bulk nuclear matter corresponding to nucleon pairing [35][16]. Despite this, the properties of QCD matter are poorly understood in most conditions, including the important case of moderately high densities obtained in NSs and SNe.

The EoS of QCD matter is well-explored in three regions of temperature and baryon chemical potential (μ_B): at low temperatures below saturation density, at high temperatures and low density, and at high temperature or density (Fig. 9). At low temperature, the QCD phase diagram is well understood up to the saturation density of nuclear matter, which is the ground state of this material and happens near a mass density of $\rho_0 = 2.5 \times 10^{14}$ g cm^{-3} [35], a number density of $n_0 = 0.150 \pm 0.010$ fm^{-3} [88], and a baryon chemical potential near $\mu_B^0 = 924$ MeV [9]. The properties of this phase are easy to model microscopically using ChEFT, to within a margin of about 24% up to 1.1 n_0; very low densities also clump into discrete nuclei and behave in predictable manners [7]. At high temperature, LQCD can estimate the properties of QCD matter at zero μ_B, and various tricks can be used to generate a power-series expansion of the EoS if $\mu_B/T \lesssim 2.5$ [89]. Also, at very high temperatures or μ_B, such as densities $\gtrsim 20\ n_0$, QCD enters the perturbative

regime, which can calculate asymptotic properties of the EoS at high density [90]. From this, we know of at least four phases of QCD matter (Fig. 9): a high-temperature QGP, a low-temperature, high-density color superconductor, and two phases of color-confined hadronic matter [9]. The remainder of the diagram, which is believed to include the critical point and phase boundary between the confined and deconfined phases, is poorly understood, but can possibly be reached in high-energy collisions at particle colliders [8].

5.1 Quark–gluon plasma (QGP)

In the 1960s, the observation of the cosmic microwave background prompted investigation on what kind of matter filled the early universe. Hagedorn's bootstrap model predicted exponentially many hadron resonances at increasing masses and therefore an upper limit to the temperature of a hadron gas, empirically in the range $150 < T_H < 200$ MeV, making it meaningless above this cutoff [91]. A solution was proposed with the 1975 discovery of asymptotic freedom by Collins and Perry, from which Cabibbo and Parisi deduced that same year that the hadrons should break down into a liquid of quarks. This phase, called QGP, was ultimately identified in the early 2000s at RHIC as a liquid phase that forms and equilibrates rapidly (in around 10^{-24} s) in HICs; one of its characteristic signatures is that the hadrons produced in HICs during the freeze-out phase are rich in strange quarks and antiquarks, which are less massive than T_c and are about as abundant in neutral QGP as the u and d quarks.

LQCD calculations as early as 1990 established that the transition from QGP to hadronic matter occurs around $T \sim 160$ MeV and is continuous, but rapid, at zero μ_B [92]; there is expected to be a critical point in the T–μ_B plane beyond which the transition is first-order [13], but very little is known, empirically or from LQCD, about its location, except that it is likely at a temperature slightly below T_c and that $\mu_B \gtrsim 250$ MeV at this point [8]. QGP also has the unusual property of being the most perfect fluid known, with a viscosity-to-entropy density ratio close to the lower bound of $1/4\pi$ predicted by the AdS/CFT correspondence [93]. This property is due to the strong coupling between quarks and gluons, and this coupling is also reflected in HIC data by a suppression

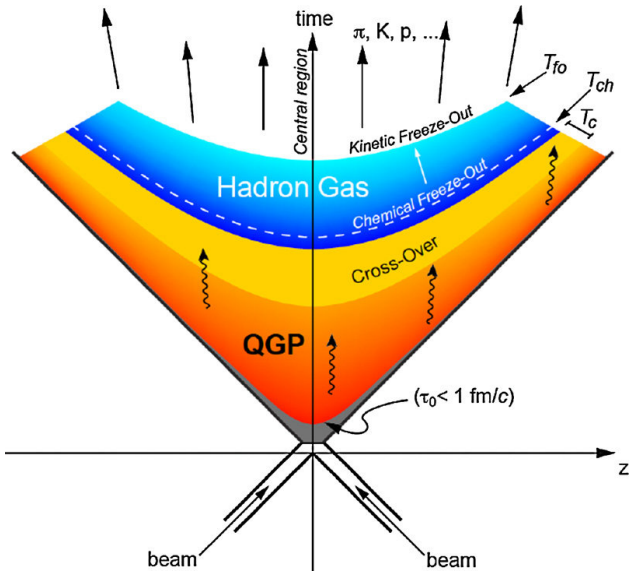

Figure 10: Spacetime diagram of the formation of QGP and its subsequent hadronization in a HIC, where two large nuclei such as gold are collided at high speeds. Figure taken from [12].

of high-momentum hadrons and charmonium produced during hadronization [91].

5.1.1 LQCD calculation

For $T \gtrsim \Lambda_{\mathrm{QCD}}$, the QGP EoS can be calculated by perturbative expansion; the normal perturbative expansion breaks down after the term of order g^6, but better estimates can be provided through techniques such as partial resummation of the expansion [9]. Below this temperature, it is necessary to use LQCD to conduct this analysis. The fermion sign problem prevents ab initio calculation except at $\mu_B = 0$, and the calculation also becomes increasingly hard below $T \sim 100$ MeV, but this is enough to expand the pressure of QCD matter as a Taylor series in powers of μ_B/T:

$$\frac{P(T,\mu_B)}{T^4} = \sum_{n=0}^{\infty} c_{2n}(T) \left(\frac{\mu_B}{T}\right)^{2n}. \tag{79}$$

The terms can be extracted directly, and more precisely, by calculating at imaginary μ_B, where the sign problem can be avoided; even more precise estimates can be obtained by resumming this power series and recovering the original coefficients [34]. In expanding this formula, it is also possible to estimate the location of the QGP–hadron critical point from the series' radius of convergence, since

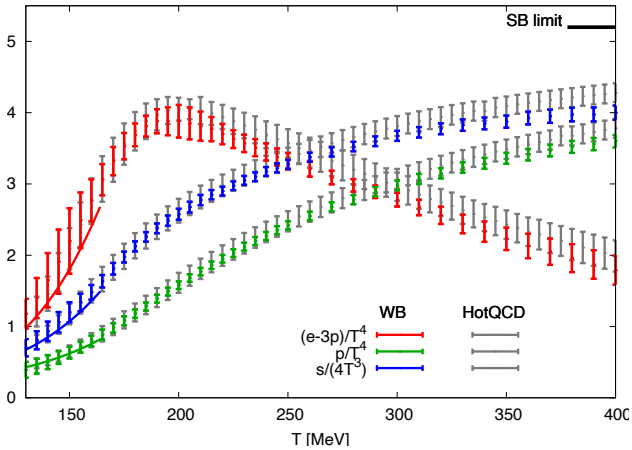

Figure 11: LQCD results for $N_f = 2 + 1$ (u, d, s) with physical quark masses at $\mu_B = 0$ and extrapolated to the continuum. Figure taken from Fig. 1a of [13].

at this point there is a singularity in the thermal susceptibilities [13],

$$\chi^{BSQ}_{lmn} = T^{-4+l+m+n} \frac{\partial^{l+m+n} P}{\partial \mu_B^l \partial \mu_S^m \partial \mu_Q^n}. \tag{80}$$

The QCD matter EoS has been computed at the physical quark masses for $N_f = 2 + 1 + 1$ [94]. Charm quarks become a significant component of QGP when $T \gtrsim 300$ MeV — in contrast, at $T = 0$, charm quarks do not appear until $\mu_B \geq 3m_c = 3819(14)$ MeV [9].

5.2 Color superconductor

In an electrical conductor, the BCS theory describes the formation of superconductivity when the electron–phonon interaction is weak. The electron–phonon interaction is most attractive slightly below the Debye frequency, and if it is strong enough, then at low temperatures they bind together into a singlet Cooper pair, which has a binding energy Δ known as the pairing gap [86]. The $U(1)$ symmetry of electromagnetism is spontaneously broken to Z_2, which causes the photon to gain a nonzero effective mass — this leads to the well-known Meissner effect, where the magnetic field in a bulk superconductor attenuates exponentially with depth [9, 95].

At high densities, the Fermi momenta of quarks become high, and above the cutoff $\Lambda_{\text{QCD}} \approx$ 200 MeV, they become deconfined and form quark matter [9]. Additionally, at low temperatures,

the force between different-colored quarks (which is always attractive, unlike in superconductors) causes them to join into diquarks and form a color superconductor. For densities $\gtrsim 20\ n_0$, it is possible to use a perturbative expansion of QCD to derive the EoS [90]. The pairing gap in this case has the asymptotic expression [90]

$$\Delta/\mu_B \sim 845.7 g^{-5} e^{-3\pi^2/(g\sqrt{2})} \tag{81}$$

While such densities are too high to occur in NSs, observed properties of NSs can constrain the CFL pairing gap by requiring stability and causality, which implies that the speed of sound,

$$c_s = \sqrt{\left(\frac{\partial P}{\partial \epsilon}\right)_{(s/n)}} \tag{82}$$

is between 0 and 1 inclusive in natural units; and thermodynamic consistency at intermediate densities. At $\mu_B = 2600$ MeV ($n_B \approx 40\ n_0$), Ref. [90] calculates an upper bound for Δ at 95% level as 457 MeV using these assumptions, or 216 MeV assuming that $c_s \leq 1/\sqrt{2}$. (For comparison, $c_s = 1/\sqrt{3}$ in conformal field theories, and for $\mu_B \gtrsim 2200$ MeV the speed of sound in quark matter approaches this value from below [7][90].) Like in superconductors, the color superconductor has a second-order phase transition to QGP at high temperatures, on the order of the BCS-theory prediction

$$T_c \approx \frac{e^\gamma}{\pi}\Delta = 0.5669\Delta, \tag{83}$$

where $\gamma \approx 0.5772$ is the Euler–Mascheroni constant [9].

For the $N_f = 3$ case, the color superconductor phase formed is the CFL phase, which has an SU(3) gauge symmetry that combines flavor and color, if $\Delta \gtrsim 3m_s^2/(2\mu_B)$ [90]. In CFL, all eight gluons acquire a nonzero effective mass and there is an additional Goldstone boson from the breaking of the $U(1)_V$ baryon number symmetry, which corresponds to the diquark condensate in color superconductor and the H dibaryon condensate in hadronic matter [9]. There is possibly an alternative mode of superconductivity at densities intermediate between nuclear matter and the

CFL phase, such as the 2-color superconductivity case where $N_f = 2$, only two of the three colors form pairs, and there are five massive gluons. On the other hand, the symmetry of the CFL is the same as for nuclear matter upon formation of an H-dibaryon condensate [9], which leads to the hypothesis that the transition from hadronic to quark matter is in fact continuous at low T [96]. Some researchers have even proposed that cold quark matter is more stable than nuclear matter, and could exist in nature as small dense chunks called strangelets (if they contain significant strange quark content) or quark nuggets [97][98].

5.3 Hadronic phase

At low temperature and density, quarks are confined into hadrons and can be studied using ChEFT [99, 6]. At high temperatures, but below the QGP transition, the best known description of hadronic matter is the hadron resonance gas, where various hadron states exist in chemical equilibrium and behave as a quantum van der Waals gas [100]. Another common class of models are the RMF and (D)BHF models, which focus on exchange of mesons between baryons treated as fields averaged over space [41], with scalar mesons contributing an attractive force and vectors a repulsive force [101]. There is no net contribution from pseudoscalar or pseudovector interactions, or from exchange of non-neutral mesons such as the $\rho^{\pm}$ and K^*, in RMF because the strong force preserves parity; (D)BHF, however, does include the lowest-order local interactions due to these particles [101, 102, 103].

Below saturation density, nuclear matter decomposes spinodally into a heterogeneous condensate [100], with densely-packed nuclei at low densities, and then several nuclear pasta phases where the nuclei become deformed into complex structures and a relatively sparse, neutron-rich gas fills the gaps [35]. However, very little is known about nuclear matter above saturation density; above 2 n_0 there is likely a new, exotic phase with additional hadron species such as Λ's and kaons, and it is possible that QCD matter enters the color-superconductor phase at this point [35, 14, 41].

Around T = 10–20 MeV, there is another critical point that separates the hadron gas from a liquid phase where the attractive scalar-meson force dominates [100, 9]. The liquid phase dominates

the interior of an NS and is a superfluid [35, 104] — a property closely related to nucleon pairing in finite nuclei [85]. Finite nuclei live on this phase boundary at $T = 0$ [9].

5.4 Symmetry energy and derivatives

Around the saturation density, the binding energy of cold symmetric nuclear matter, with equally many protons as neutrons, can be expanded in derivatives of the baryon density, typically parametrized as $x = (n_B - n_0)/3n_0$ [16]:

$$B(n_B) = B_0 + \frac{K}{2}x^2 + \frac{Q}{6}x^3 + O(x^4). \tag{84}$$

The binding energy of symmetric nuclear matter, ignoring the pressure due to electrons, is $B_0 = -16 \pm 1$ MeV/nucleon. The incompressibility K (also 9 times the bulk modulus) for symmetric matter has been measured as 240 ± 20 MeV [105]. It can also be expanded in terms of the fraction of nuclei that are protons (Y_p) in terms of the asymmetry $\beta = 2Y_p - 1$; due to the approximate $\mathrm{SU}(2)_f$ symmetry, this expansion contains only even powers of β [105]. That is,

$$B(n_B, Y_p) = B(n_B, 1/2) + S\beta^2 + O(\beta^4). \tag{85}$$

The parameter S is known as the symmetry energy of nuclear matter. If the series is cut off at order β^2, then the binding energy of pure neutron matter, with $\beta = -1$, is equal to S plus the binding energy of symmetric matter, and the symmetry energy is sometimes instead defined as this difference [16]. If disambiguation is necessary, we will denote the derivative-based definition as S_2, and the next higher order term in Eq. (85) is $S_4\beta^4$. It expands around n_0 as

$$S(n_B) = S_0 + Lx + K_{\mathrm{sym}}x^2 + Q_{\mathrm{sym}}x^3 + O(x^4) \tag{86}$$

The saturation-density symmetry energy S_0 and the slope L, as constrained from nuclear masses and the difference in rms radii between the protons and neutrons in asymmetric nuclei (a.k.a. the

neutron skin), are respectively calculated in Ref. [16] as 32.0 ± 1.1 MeV and 53 ± 13 MeV. As with symmetry energy, we will denote the slope of S_2 as L_2 where disambiguation is necessary.

5.5 Single-particle potential

In general, the energy of a baryon i in the nuclear medium has an additional correction that depends on density and momentum:[99]

$$E_i(p) = \sqrt{p^2 + m_i^2} + U_i(n_B, p) \tag{87}$$

The quantity U_i is the single-particle potential, which is the potential energy of a baryon in bulk nuclear matter relative to the surrounding empty space. The lowest nontrivial correction of this type is due to two-body interactions with other baryons, but three-body interactions can also be added. In this dissertation, we will assume that the baryon is embedded in nuclear matter, i.e. with only nucleons except possibly the baryon i. The Hartree approximation assumes that U_i is independent of p, but with an effective Dirac mass m_i^* which is not necessarily the same as in vacuum [41].

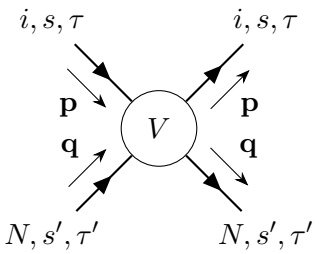

Figure 12: Feynman diagram representing the i–nucleon interaction for the single-particle potential $U_i(p, n_B)$ in nuclear matter; the momenta, spins, and isospins of the particles are unchanged.

The two-body interaction can be described by the Feynman diagram in Fig. 12, where the S-matrix $V_{s,s',\tau,\tau'}(\mathbf{p}, \mathbf{q})$ can be computed using ChEFT [99]. Let $f(\mathbf{p})$ be the probability of occupation by a nucleon for the eigenstate with momentum $\mathbf{p}$. Then we can integrate V over the entire medium,

assuming that i is a single baryon with momentum $\mathbf{p}$:

$$\begin{aligned} G_{s,s',\tau,\tau'}(\mathbf{p},\mathbf{q}) &= \frac{f_{N,s',\tau'}(\mathbf{q})}{V^2}\int \frac{d^3\mathbf{x}\; d^3\mathbf{x}'}{(2\pi)^6} e^{i\mathbf{p}\cdot\mathbf{x}} e^{i\mathbf{p}'\cdot\mathbf{x}'} V_{s,s',\tau,\tau'}(\mathbf{p},\mathbf{q}) e^{-i\mathbf{p}'\cdot\mathbf{x}'} e^{-i\mathbf{p}\cdot\mathbf{x}} \\ &= f_{N,s',\tau'}(\mathbf{q}) V_{s,s',\tau,\tau'}(\mathbf{p},\mathbf{q}) \end{aligned} \tag{88}$$

At fixed $\mathbf{p}$ and $\mathbf{q}$, the diagram then evaluates to:

$$\begin{aligned} M_{s,s',\tau,\tau'}(\mathbf{p},\mathbf{q}) &= a^\dagger_{i,s,\tau}(\mathbf{p}) a^\dagger_{N,s',\tau'}(\mathbf{q}) \langle 0|G_{s,s',\tau,\tau'}(\mathbf{p},\mathbf{q})|0\rangle a_{N,s',\tau'}(\mathbf{q}) a_{i,s,\tau}(\mathbf{p}) \\ &= \langle \mathbf{p}_i, \mathbf{q}_N | G(\mathbf{p},\mathbf{q}) | \mathbf{p}_i, \mathbf{q}_N \rangle \end{aligned} \tag{89}$$

We can integrate the above expression over $\mathbf{q}$ to get the single-particle potential [99]:

$$U_{i,\tau}(n_B,\mathbf{p}) = \int \frac{d^3\mathbf{q}}{8\pi^3} \sum_{ss'\tau'} M_{s,s',\tau,\tau'}(\mathbf{p},\mathbf{q}). \tag{90}$$

In order to actually evaluate Eq. (90) and solve the EoS of ChEFT, we must solve it self-consistently with the Bethe–Goldstone equation. If we define ω as the combined energies of the two baryons (including rest mass and potentials), then excluding baryon-mixing terms, it becomes [99][106]:

$$G(\omega) = V_{iN} + \lim_{\epsilon\to 0} \sum_{\mathbf{p},\mathbf{q}} V_{iN}|\mathbf{p}_i,\mathbf{q}_N\rangle \frac{[1-n_i(\mathbf{p})][1-n_N(\mathbf{q})]}{\omega + i\epsilon - E_{\mathbf{p},i} - E_{\mathbf{q},N}} \langle \mathbf{p}_i,\mathbf{q}_N| G(\omega), \tag{91}$$

where $E_{\mathbf{p},i} = \sqrt{\mathbf{p}^2 + m_i^2}$. The baryon-mixing terms are similar, except that in the sum the baryons may be different from i and the nucleon.

If the nuclear medium is symmetric, then $U_{i,\tau}$ is independent of isospin. In neutron matter, there is a splitting of isospin states where the potentials of baryons with positive τ_3 are lowered by the ρ interaction compared to symmetric matter with the same density, and those with negative τ_3 are raised [41].

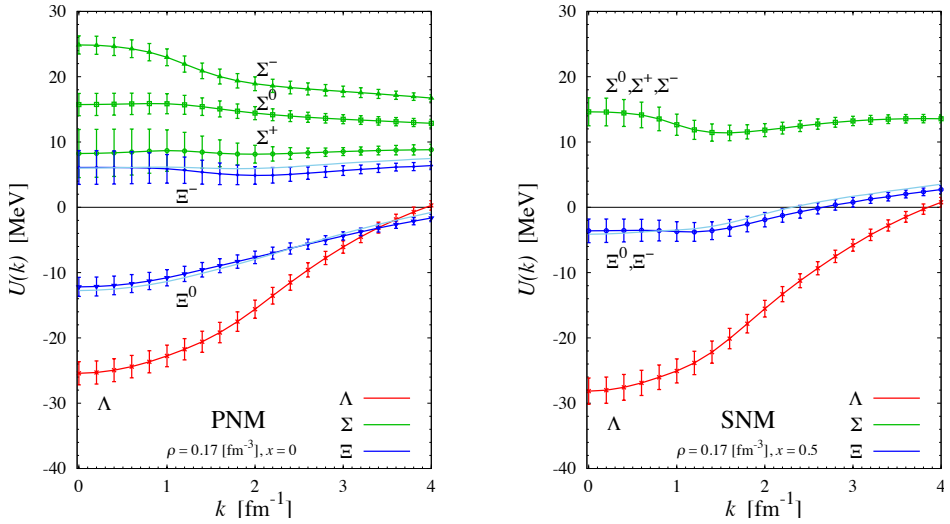

Figure 13: Single-particle potentials of the hyperons in neutron matter (left) and symmetric matter (right), as estimated from LQCD calculations by the HALQCD Collaboration [2]. The light-blue lines are for the Ξ baryon potentials after correcting for SU(3)$_f$ breaking, which contributes around 0.5–1.5 MeV.

6 Neutron stars (NSs)

NSs are extremely dense degenerate objects, $\sim$ 10 km in radius and about 1.4–2.2 $M_\odot$ in mass, formed when a star with initial mass 8–25 $M_\odot$ reaches the end of its life and goes SN [35]. Very little is known about their internal structure, their precise radius, or the maximum attainable mass before it collapses into a BH, as this information is related to the poorly-understood intermediate-density, low-temperature regime of QCD matter [35].

About 4% of known NSs are part of a binary system; the companion is most often a white dwarf [107]. Most interesting are binary NSs, thought to form from close OB binaries [108], as a probe for the study of GWs and the likely major source of r-process elements [109]. Indeed, the first indirect observation of GWs was from the timing of the shrinking orbital period of the PSR B1913+16 binary system, which is in close agreement with the predictions of general relativity [110]. The final merger of a binary NS was finally observed as GWs from the GW170817 event, and could be correlated with simultaneous electromganetic observations in several bands, from gamma rays to radio waves, in the galaxy NGC 4993 [111]. The end product of such a collision is most likely a BH

[108]. Together with direct X-ray observations of NSs by the NICER telescope, GW observations of binary-NS and NS–BH collisions provide important constraints on the QCD EoS above saturation density, particularly the NS radius R and the tidal deformability Λ [16].

6.1 Internal structure

6.1.1 Outer layers

The outer layers of an NS are well characterized from the known region of the QCD matter EoS. There is a $\sim$ 0.1–10 cm-thick atmosphere that is mostly hydrogen and helium plasma, on top of a solid outer crust of iron with a surface density of about $\rho = 10^6$ g cm^{-3} [35]. Nuclei in this region are forced into β-equilibrium:

$$\begin{aligned} p + e^- &\rightarrow n + \nu_e \\ n &\rightarrow p + e^- + \overline{\nu_e} \end{aligned} \tag{92}$$

In free space, the average charge per baryon (designated as Y_q) tends toward 0.5 for the smaller nuclei and 0.4 for the heavier ones. At higher density, the Fermi pressure of the electron gas pushes the β-equilibrium toward increasingly neutron-rich matter. Then, at around $\rho = 4 \times 10^{11}$ g cm^{-3}, the nuclei reach the neutron drip line, and the system deforms into a complex series of phases known as nuclear pasta. The nuclear pasta phases feature various complex and disordered arrangements of nuclear matter within a superfluid of neutrons, such as lasagna and spaghetti [35].

The nuclear pasta phase dissolves at around 0.5 ρ_0 into a uniform superfluid of nucleons, which forms the outer core of the NS [35].

6.1.2 Inner core

Beyond $\sim$ 2–3 ρ_0 lies the inner core, where the QCD matter EoS is unknown, but is expected to be a new, exotic phase. Various models have been constructed for this phase [41] (Fig. 14), positing exotic phases such as deconfined quark matter, hyperons, Δ baryons, condensates of the H-dibaryon (a hypothetical six-quark state with composition $uuddss$ [112]), and π^- and K^- meson condensates [35].

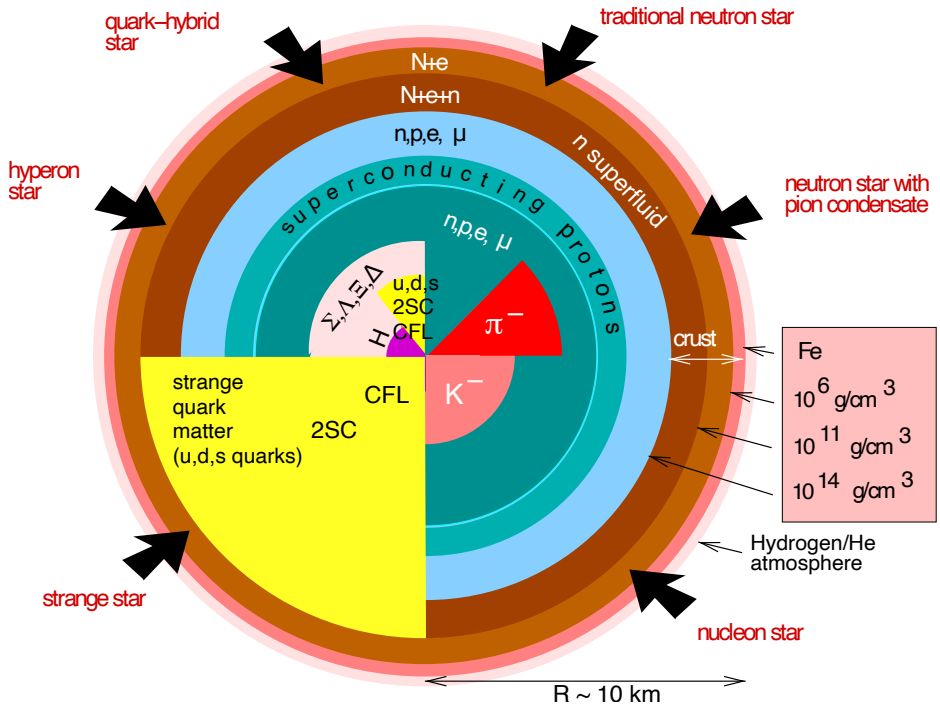

Figure 14: Various models of the interior of an NS, clockwise from top: pure nuclear matter, π^- and K^- condensates, quark star, hyperon core with possible H-dibaryon condensate, and hyperons followed by quark matter [14].

Deconfined quark matter is the most probable contents of the inner core for the most massive NSs, based on astrophysical constraints on $M_{\rm max}$ and Λ; NSs with quark cores are sometimes called hybrid stars [113]. This is likely to happen if the speed of sound in dense hadronic matter is not substantially greater than $1/\sqrt{3}$, and the transition from hadronic to quark matter is first-order or nearly so. In contrast, a small range of EoSs satisfying the constraints and maximal speed of sound over $\sqrt{0.7}$ do not have any stable NSs with quark cores, and it is likely that 2 $M_\odot$ NSs do not have quark cores if $M_{\rm max} > 2.25\ M_\odot$ [7]. If the low-T transition from hadronic to quark matter is first-order, then hybrid stars should have a layer containing a series of mixed "quarkyonic" spinodal phases similar to the nuclear pasta layer [113]. There may even be compact stars made entirely of quark matter —these so-called quark stars would be substantially smaller than NSs, and in contrast to NSs and white dwarfs, their radius would increase with mass up to shortly before the maximum mass. The formation of a quark star would produce a short-lived gamma-ray burst [114].

The K^+p interaction is well-studied through scattering experiments and is observed to be moderately repulsive. Less data exist for the K^-p interaction, but it has been measured in correlation functions from pp and HICs by the ALICE experiment at the LHC, as well as limited scattering data and the energy levels of kaonic hydrogen, in which the electron is replaced by a K^-. From this data, the interaction is dominated at low energies by an attractive contribution from the $\Lambda(1405)$ resonance, which has $J^P = 1/2^-$ and is generally accepted to be a $\overline{K}N$ molecular state with a binding energy of -26.8 MeV [41]. From measurements of larger K^- atoms, there is a strongly attractive single-particle potential of $U_{\overline{K}} = -150$–200 MeV in symmetric matter. As such, a K^- condensate might form in dense QCD matter if the Dirac effective mass $m^*_{K^-}$ drops below μ_e. ChEFT models do not tend to predict that $m^*_{K^-}$ declines fast enough for this to happen, but some RMF and (D)BHF models do predict this [41]. The πN interaction can be studied more easily through ChEFT from the study of the nuclear force. The existence of a π^- condensate is disfavored by a repulsive πN interaction in the s-wave ($L = 0$) channel [115], but if a π^- condensate exists at low Y_q and densities around 2–3 n_0, it would cause a first-order phase transition that would be easily detected as large glitches in pulsar rotation periods and as a secondary neutrino burst during the cooling of a proto-NS [116][117].

It is also possible that the Fermi pressure of dense nuclear matter can be relived through the formation of hyperons via various weak decays, again above 2–3 n_0 [41]. It is well-established from the study of hypernuclei that the ΛN and ΞN interactions are attractive, but the ΣN interaction is repulsive; the Λ single-particle potential in symmetric matter at saturation density is well-established to be near -30 MeV [118]. Little data exist on hyperon–hyperon interactions, but the few existent observations of 2Λ hypernuclei and LQCD results from the HALQCD collaboration support a weakly attractive $\Lambda\Lambda$ interaction that is much shallower than the $N\Lambda$, and not strong enough to form a bound H-dibaryon (although the $p\Xi^-$ dibaryon with the same quark contents would be bound) [119]; additionally, LQCD analyses from the HALQCD collaboration have evaluated most of the two-baryon forces for the $\mathrm{SU}(3)_f$ octet baryons as well as the Ω baryon [41]. The Ξ nuclear potential is estimated at around -15 MeV in experiments, though LQCD results

from the HALQCD calculation predict a shallower potential of about -4 MeV —however, the Ξ^- potential (which splits from the Ξ^0 in asymmetric matter) becomes repulsive in neutron-rich matter [41]. Therefore, Λ's can be expected to be significant in the NS core, but Σ's and Ξ's probably would not [41]. However, models with hyperons have difficulty achieving an NS maximum mass consistent with the heaviest pulsars because without sufficient repulsive YY or three-body YNN interactions, the EoS becomes too soft above this density threshold [41], and the onset of hyperons at a low baryon density causes excessively rapid cooling through weak decay modes, particularly the Urca processes,[7] such as $\Lambda \to p + e^- + \overline{\nu}_e$ [30, 121, 122]. Proposed solutions include the repulsive ϕ meson interaction between hyperons and the three-body ΛNN interaction which is expected to be repulsive [41]. Additionally, the Δ baryons, which have attractive ΔN interactions, and are expected to have a single-particle potential comparable to nucleons, could occur in the same density range; they would have minimal effect on the NS maximum mass but would significantly decrease the radius, and if the ΔN interaction is stronger than the NN interaction, then they would slightly stiffen the EoS of hyperon-rich nuclear matter [41, 43]. Since Δ baryons also have spin 3/2, they are possibly even more favored in highly magnetized ($\sim 10^{13}$–10^{15} G, up to $\sim 10^{16}$ G in the interior [123]) NSs called magnetars [124].

6.2 Mass–radius relation

The mass–radius relation of an NS is sensitive to the EoS of QCD matter [125, 16], and possibly also the presence and properties of dark matter surrounding it [126]. For an isolated, non-rotating NS, it can be related to the EoS by the general-relativistic TOV equation (in geometrized units where $G = c = 1$) [127, 35]:

$$\begin{aligned} \frac{dP}{dr} &= -\frac{m\epsilon}{r^2}\frac{(1 + P/\epsilon)(1 + 4\pi r^3 \epsilon/m)}{1 - 2mr} \\ \frac{dm}{dr} &= 4\pi r^2 \epsilon \end{aligned} \tag{93}$$

[7] Named after a former casino in Rio de Janeiro, where George Gamow and Mario Schenberg first proposed the mechanism, and a Russian colloquial word for "robber" in Odesa [120].

where $m(r)$ is the total mass within radius r of the center, and ϵ and P are the energy density and pressure, respectively, as determined by the EoS; the total mass is then $M = \int_0^R 4\pi r^2 \epsilon dr$, where R is the radius of the NS. In order to approximate the structure of a rotating NS, one can use the Hartle–Thorne perturbative approximation, in which the following effects are calculated in order: the total angular momentum of the star, the increased mass and a monopole correction to internal pressure due to rotational kinetic energy, and its deformation and a quadrupole correction to internal pressure [35].

There is a minimum size for a compact object, below which it will become a BH [127]. If we define the dimensionless compactness $C = M/R$, then the simplest bound is the Schwarzschild radius of a non-rotating, uncharged BH, which is $C = 1/2$; for comparison, the value for the Sun is $C = 2 \times 10^{-6}$ [128]. For a uniform body, Buchdahl's theorem also establishes a stricter bound of $C = 4/9$, at which point the internal pressure becomes infinite — this is physically unreasonable because the causality condition $c_s \leq 1$ from Eq. (82) implies that $P \leq \epsilon$ for all materials; the causality bound for this case is $C \approx 0.355$ [128].

The minimum NS mass that can be made in a core-collapse SN is estimated at around 1.17 $M_\odot$, close to the measured mass of the light pulsar PSR J0453+1559 [129]. The theoretical minimum mass that is stable under gravity is estimated at around 0.087–0.093 $M_\odot$, and is insensitive to the properties of the QCD EoS in this region [130]. The maximum mass can be constrained from below by simply finding massive NSs, such as the 2.08 ± 0.07 $M_\odot$ NS PSR J0740+6620 [131]. The heaviest measured NS to date is PSR J0952−0607, which has been measured at 2.35 ± 0.17 $M_\odot$, implying a maximum mass at 1σ (3σ) confidence of at least 2.19 $M_\odot$ (2.09 $M_\odot$) [24]. From the GW170817 data, Rezzolla *et al.* (2018) estimated a maximum mass of $2.16^{+0.17}_{-0.15}$ $M_\odot$ [26].

6.3 Tidal deformability

Tidal deformability is a measure of how much a body deforms under a non-uniform gravitational field, which is responsible for the tides. In the Newtonian limit, the tidal force $\mathcal{E}_{ij}$ is the Hessian of

the gravitational force field [132]. The quadrupole moment is

$$Q_{ij} = \int d^3\mathbf{x}\ \epsilon(3x_i x_j - \delta_{ij} r^2) \tag{94}$$

Then at low field strengths, the tidal deformation will be asymptotically linear in $\mathcal{E}_{ij}$, as

$$\frac{1}{3} Q_{ij} = -\lambda \mathcal{E}_{ij} \tag{95}$$

where λ has length dimension 5 in geometrized units. In the strong field case, the quadrupole moment and tidal forces can be defined in the asymptotically flat region (using East Coast sign convention) as [133]

$$\frac{1 - g_{00}}{2} = -\frac{M}{r} - \frac{Q_{ij}}{2r^3}\left(\frac{x^i x^j}{r^2} - \frac{1}{3}\delta^{ij}\right) + O\left(\frac{1}{r^3}\right) + \frac{1}{2}\mathcal{E}_{ij} x^i x^j + O(r^3). \tag{96}$$

There are two dimensionless numbers that can be derived from λ: the Love number $k_2 = \frac{3}{2}\lambda R^{-5}$ and the tidal deformability $\Lambda := \lambda M^{-5}$ [132]. From GW170817, the LIGO/VIRGO team measured a deformability of $\Lambda = 190^{+390}_{-120}$ for an NS mass of 1.4 $M_\odot$ [23].

6.4 Moment of inertia

Angular momentum in general relativity is defined (in East Coast sign convention) as [134]:

$$J = \int T^{\mu\nu} \xi^\nu \sqrt{-g}\ d^3x \tag{97}$$

where ξ is a Killing vector in the axial direction; g is the determinant of the metric tensor; and T is the stress–energy tensor, which for a body made of a perfect fluid (approximately true for most real stars) is

$$T^{\mu\nu} = (\epsilon + P) u^\mu u^\nu + p g^{\mu\nu}, \tag{98}$$

with u being a unit timelike velocity vector. For a spherically symmetric star with angular velocity Ω much lower than the maximum before breaking up (on the order of 1 kHz), the moment of inertia $I = dJ/d\Omega$ is

$$I \approx \frac{8\pi}{3} \int_0^R (\epsilon + P) \frac{e^{-\phi(r)}}{1 - 2m(r)/r} r^4 \frac{\overline{\omega}}{\Omega} dr \tag{99}$$

where $m(r)$ is integrated mass up to r, $\overline{\omega} = \Omega - \omega$ is the relative angular velocity of a layer, and $\overline{\omega}$ and ϕ obey the differential equations

$$\frac{d\phi}{dr} = m(r) \left[1 + \frac{4\pi r^3 P}{m(r)}\right] \left[1 - \frac{2m(r)}{r}\right]^{-1} \tag{100}$$

$$0 = \frac{1}{r^3} \frac{d}{dr} \left[r^4 j \frac{d\overline{\omega}}{dr}\right] + 4\overline{\omega} \frac{dj}{dr} \tag{101}$$

where

$$j := e^{-\phi} \sqrt{1 - \frac{2m(r)}{r}}. \tag{102}$$

The empirical formula of Lattimer & Schutz (2005) describes moment of inertia well for NSs under most nucleonic EoS's [134]:

$$I \approx [0.237(8)] M R^2 \left[1 + (4.2 \text{ km } M_\odot^{-1}) \frac{M}{R} + (90 \text{ km}^4 \ M_\odot^{-4}) \left(\frac{M}{R}\right)^4\right]. \tag{103}$$

Measurements of PSR J0737−3039A, which has mass 1.3381(7) $M_\odot$ and $\Omega/2\pi = 44.05$ Hz [135], constrain it to have a moment of inertia less than 150 $M_\odot$ km^2 [29], based on the double pulsar's post-Keplerian parameters. The actual value should be around 65 $M_\odot$ km^2 if it is a neutron or hybrid star, or 78 $M_\odot$ km^2 if it is a quark star [28].

6.5 Empirical and semi-empirical constraints on the QCD EoS at low T

6.5.1 Finite nuclei

As defined in Eq. (84), the incompressibility of nuclear matter is

$$K = 9n_B^2 \frac{\partial^2 B}{\partial n_B^2}. \tag{104}$$

For symmetric matter, the consensus value at saturation density is $K(n_0) = 240 \pm 20$ MeV. This is experimentally measured using GMRs, where all nucleons in a nucleus are collectively excited with an energy of about 10–30 MeV, of the magic-N nuclei ^{90}Zr and ^{208}Pb [105]. However, GMR measurements of nuclei that do not have closed neutron shells find significantly softer (lower) values of $K(n_0)$ than those fitted from magic nuclei; for example, GMR measurements for the stable even-N isotopes of tin ($^{112\text{–}124}$Sn) seem to favor a value of $K(n_0)$ near 215 MeV, with the heavier isotopes being softer than the lighter ones. The origin of this discrepancy is unknown, but is probably related to the properties of partially open nuclear shells.

For symmetry energy, the primary experimental constraint is from measurement of the neutron skin of nuclei with more neutrons than protons, which is the difference in radii between the proton and neutron distributions in a nucleus [41]; it is strongly correlated with the slope $L = 3n_B(\partial S/\partial n_B)$ as defined in Eq. (86), and more weakly dependent on symmetry energy itself [16]. One way of measuring neutron skin is through weak parity violation in elastic electron–nucleus scattering; since the Z boson couples much more strongly to neutrons than to protons, this provides an accurate measurement of the collective neutron wavefunction. For ^{208}Pb ($N-Z = 44$), the best measurement to date with this method is $R_{\text{skin}} = 0.280 \pm 0.071$ fm [136]. Another study, based on analysis of hydrodynamics in HICs, found a similar value of $R_{\text{skin}} = 0.217 \pm 0.058$ fm for the same nucleus [137]. At saturation density, $S = 32.0 \pm 1.1$ MeV and $L = 53 \pm 13$ MeV; little is known about the values of the higher-order derivatives K_{sym} and Q_{sym} [16].

6.5.2 ChEFT

ChEFT is the most accurate known low description for the properties of low-density, low-temperature hadronic matter [16, 6]. By calculating the single-particle nucleon potential and the Bethe–Goldstone equation as outlined in Section 5.5, one can deduce the thermodynamic properties of nuclear matter and obtain an EoS, including estimates on the ChEFT truncation error [99, 15]. In contrast to symmetric matter being easier to study experimentally because stable nuclei are close to symmetric, ChEFT is more reliable for neutron matter than for symmetric matter. This is because the properties of symmetric matter are sensitive to the poorly-measured three-body interactions which begin at $\mathrm{N^2LO}$, but in neutron matter two of the $\mathrm{N^2LO}$ forces do not occur due to the Pauli exclusion principle [16][15]. The most recent ChEFT models for cold, β-equilibrated hadronic matter have constrained the pressure–energy-density relation at $T = 0$ to around 24% precision, and agree well with finite-nucleus and astrophysical data [7].

6.5.3 NS observables

For NSs in binary systems, it is possible to measure the masses of both objects and their orbital inclination relative to Earth's line of sight [110]. For a generic binary system, four Keplerian parameters can be measured precisely: the orbital period P, the eccentricity e, and time T_0 and longitude ω_0 (w.r.t. the line of sight) of periastron [41]. Often, one can also measure either the projection of one body's semi-major axis ($x = a_1 \sin i$, where i is the inclination w.r.t. Earth's line of sight), or the peak radial velocity K, which are related by [138, 107]:

$$K = \frac{2\pi a_1 \sin i}{P} \tag{105}$$

Together, these observables allow the calculation of the mass function [138, 41]

$$f = \frac{m_2^3 \sin^3 i}{(m_1 + m_2)^2} = \frac{PK^3}{2\pi G}(1 - e^2)^{3/2}. \tag{106}$$

To determine the masses and inclination, two additional independent parameters need to be measured; for example, for some planetary systems one can measure the mass of the host star (easily estimated from spectral properties) and its inclination (through astrometry, or if the planet transits the face of its host star as seen from Earth) [139]. For compact binaries with at least one pulsar, neither of these can be observed, but it is often possible to measure at least two of five post-Keplerian parameters that quantify general-relativistic effects [41]: the apsidal precession of the orbit $\dot{\omega}$; the parameter γ, which is the combined amplitude of the transverse Doppler effect and gravitational redshift; the rate of orbital decay $\dot{P}$ due to gravitational radiation [140]

$$\dot{P} = \frac{192\pi G^{5/3}}{5c^5} m_1 m_2 (m_1 + m_2)^{-1/3} \left(1 + \frac{73}{24}e^2 + \frac{37}{96}e^4\right)(1 - e^2)^{-7/2} \left(\frac{P}{2\pi}\right)^{-5/3}; \tag{107}$$

and the range r and shape s of Shapiro delay, which is the delay of a pulsar signal due to the system's gravitational well. Measurements of the Shapiro delay must be corrected by the Einstein and Rømer delays, as well as the same delay effects within the Solar System [141].

The mass and radius of an NS can also be measured from X-ray emissions from the atmosphere, but not much is known about NS atmospheres apart from it likely being fully ionized, hotter than normal stars, and composed of light elements. For PSR J0740+6620, the second most massive pulsar measured to date, the NICER experiment measured X-ray emissions, and assuming a fully ionized hydrogen or helium atmosphere with hot spots, estimated its radius as $12.39^{+1.30}_{-0.98}$ km and calculated a surface temperature as $9.8^{+1.2}_{-1.3} \times 10^5$ K [20]; the measured mass of $2.072^{+0.067}_{-0.066}\ M_\odot$ is in close agreement with the dynamically measured mass (with its ultra-low-mass $0.253^{+0.006}_{-0.005}\ M_\odot$ white dwarf companion) of $2.08^{+0.07}_{-0.07}\ M_\odot$ from Ref. [131].

GW signals from binary NS mergers can be split into an inspiral, a merger, and a ringdown phase. During the inspiral, the dominant effect that can distinguish binary-NS merger from a binary BH merger is the tidal deformability Λ of an NS [23], since this quantity is zero for a BH [111].

Also, a reduced mass-like function called the *chirp mass* can be precisely measured because it

affects the GW inspiral waveform at first PN order [27]:

$$\mathcal{M} = \frac{(m_1 m_2)^{3/5}}{(m_1 + m_2)^{1/5}} = \mu^{3/5} M^{2/5} \tag{108}$$

The ratio of the two masses and the spin component parallel to the orbital angular momentum occur at $1\frac{1}{2}$ PN order [27], while the correction due to Λ first appears at fifth PN order [23]. Few compact objects are known to have masses between that of PSR J0740+6620 and about 5 $M_\odot$, so any object below the lower rim is likely an NS, and any object over the upper rim must be a BH; the nature of most objects within the mass gap, such as the $2.31^{+0.41}_{-0.22}$ $M_\odot$ companion of PSR J0514−4002E, is unknown [142, 143].

Some properties of high-density matter can be measured around the time of merger and during the ringdown, during which the merger remnant settles down, lasting a few milliseconds to a few minutes before collapsing to a BH [11]. The GW170817 remnant was a hyper-massive magnetar that spun down rapidly and lasted for at least 10 seconds after the merger [144].

7 Our model

7.1 Density-dependent relativistic mean-field (DD-RMF) models

Our model is based on the BHB$\Lambda\phi$ [44][8] and DD2Y [145] models of hadronic matter, which are in turn extensions of the DD-RMF model called DD2 [146]; however, it is more similar to the DDB model introduced in Ref. [147]. The NS outer crust is assumed to be only nucleons and contain bound nuclei as described by the NSE model of Hempel and Schaffner-Bielich [45], hereforth "HS", consistent with a given RMF model for the nuclear liquid. In the nuclear liquid phase, BHB14 introduces the Λ hyperon and DD2Y includes the complete ground-state octet.

In RMF models, the nucleons are treated as relativistic Fermi gases which couple to classical meson fields. At the mean-field level, the fields are treated as uniform throughout space, and due to

[8] Because this is the only model constructed by the authors and accepted on an empirical basis, we will use the alternative name "BHB14".

the symmetries of the strong force, the only meson fields which are nonzero are the neutral scalar mesons and the timelike component of neutral vectors [101, 102]. The Lagrangian of DD2, which includes the nucleons, the scalar $f_0(500)$ (σ), and the ρ and ω vector mesons, has the form [146]:

$$\begin{aligned}\mathcal{L} = &\sum_{i\in B} \overline{\psi}_i(i\gamma_\mu\partial^\mu - m_i + g_{\sigma i}\sigma - g_{\omega i}\gamma_\mu\omega^\mu - g_{\rho i}\gamma_\mu\boldsymbol{\tau}_i\cdot\boldsymbol{\rho}^\mu)\psi_i \\ &+ \frac{1}{2}(\partial_\mu\sigma\partial^\mu\sigma - m_\sigma^2\sigma^2) - \frac{1}{4}\omega_{\mu\nu}\omega^{\mu\nu} + \frac{1}{2}m_\omega^2\omega_\mu\omega^\mu - \frac{1}{4}\boldsymbol{\rho}_{\mu\nu}\cdot\boldsymbol{\rho}^{\mu\nu} + \frac{1}{2}m_\rho^2\boldsymbol{\rho}_\mu\cdot\boldsymbol{\rho}^\mu\end{aligned} \tag{109}$$

where bold symbols are vectors in isospin space,[9] i is summed over all baryons, τ is the same as isospin except normalized to ±1 for the up and down quarks, and

$$\begin{aligned}\omega^{\mu\nu} &= \partial^\mu\omega^\nu - \partial^\nu\omega^\mu \\ \boldsymbol{\rho}^{\mu\nu} &= \partial^\mu\boldsymbol{\rho}^\nu - \partial^\nu\boldsymbol{\rho}^\mu.\end{aligned} \tag{110}$$

When the expectation value of the fields is taken, the timelike component of the vector fields and the third isospin component of the ρ field (the ρ^0 meson) are isolated, and Eq. (109) becomes

$$\begin{aligned}\mathcal{L} = &\sum_{i\in B} \overline{\psi}_i(i\gamma_\mu\partial^\mu - m_i + g_{\sigma i}\sigma - g_{\omega i}\gamma^0\omega_0 - g_{\rho i}\gamma^0\tau_{3i}\rho_{03})\psi_i \\ &- \frac{1}{2}m_\sigma^2\sigma^2 + \frac{1}{2}m_\omega^2\omega_0^2 + \frac{1}{2}m_\rho^2\rho_{03}^2,\end{aligned} \tag{111}$$

and in the treatise that follows the component subscripts of the ω and ρ fields will sometimes be dropped for brevity.

Immediately from this averaged Lagrangian, one can derive the EoMs that relate the meson fields to the baryon densities. From the Euler–Lagrange equation, we can define the density $n_i := \overline{\psi}_i\gamma^0\psi_i$

[9] Hence, $T = 1$ hadrons such as the ρ and the $a_0(980)$ are often called isovectors.

and scalar density $n_i^s := \overline{\psi}_i \psi_i$, which gives [148]:

$$\sigma = \frac{1}{m_\sigma^2} \sum_i g_{\sigma i} n_i^s \tag{112}$$

$$\omega_0 = \frac{1}{m_\omega^2} \sum_i g_{\omega i} n_i \tag{113}$$

$$\rho_{03} = \frac{1}{m_\rho^2} \sum_i g_{\rho i} \tau_{3i} n_i. \tag{114}$$

A property of RMF is that in infinite nuclear matter, the couplings and meson masses always appear as the dimension--2 combination g_{mi}/m_m^2 [149], except in flavor-symmetry relations between different couplings [44]. In finite nuclei, the Lagrangian EoMs (in the mean-field form as Eq. (111)) can be solved numerically as explained in Ref. [150], and because the meson Klein–Gordon equations contain the meson masses by themselves, meson masses do matter in finite nuclei, and it is necessary to fit the poorly-constrained σ mass in models intended for finite nuclei [146].

The baryon–meson couplings are equal for both nucleons due to isospin symmetry, but the nucleon masses may be different (as is actually the case). It is common for RMFs to include nonlinear terms which couple mesons to other mesons in order to reproduce the empirical value of K for symmetric matter [149]; DD-RMFs account for this effect non-perturbatively by instead treating the baryon–meson couplings as dependent on the total baryon density $n_B = \sum_i n_i$. For mesons $m \in \{\sigma, \omega\}$ in DD2, this is of the form [146]

$$g_{mi}(n_B) = g_{mi}^0 a_m \frac{1 + b_m(x + d_m)^2}{1 + c_m(x + d_m)^2} \tag{115}$$

where $x = n_B/n_0$. They set $c_m = 1/3d_m^2$ (which enforces $g''_{mi}(0) = 0$ and ensures that Σ^r is well-behaved at low density [151]), and a_m is calibrated so that $g_{mi}(n_0) = g_{mi}^0$. Some models, such as DD-MEB2 [151], also use this form for the ρ. However, DD2 and DDB use an exponential form for the ρ coupling, which diminishes its effect in dense matter:

$$g_{\rho i}(n_B) = g_{\rho i}^0 e^{a_\rho (1-x)}. \tag{116}$$

DDB used a simplified form of the isoscalar coupling, which is a stretched exponential [147]:

$$g_{mi}(n_B) = g^0_{mi} e^{1-x^{a_m}}. \tag{117}$$

The stated advantage is that it has one parameter (thus simplifying their Bayesian analysis), and the derivative of both Eqs. (116) and (117) $[\partial g/\partial n_B]_{n=n_0} = -g^0 a/n_0$. However, the derivative blows up in free space if $0 < a < 1$ (although it does not cause unphysical low-density behavior, since the Σ^r term for this interaction still vanishes at low density); and if $a > 0$ there is the unnatural relation $g(0)/g(m) = e$, which the exponential form does not do. We propose the alternate form for low density:

$$g_{mi}(n_B) = g^0_{mi} \exp\left[1 - \left(\frac{x+1}{2}\right)^{2a_m}\right], \tag{118}$$

which still has $g'_{mi}(n_0) = -g^0 a/n_0$ and similar behavior at intermediate densities, but does not change dramatically at low density. Our model welds this form smoothly to a high-density regime with constant couplings, which we believe better reproduces the qualitative behavior of the DBHF results in Ref. [152]:

$$\begin{aligned} g_{mi}(n_B) = g^0_{mi}\Bigg\{ &\exp\left[1 - \left(\frac{x+1}{2}\right)^{2a_m}\right] \frac{1 - \tanh[(x-c_m)/d_m]}{2} \\ &+ b_m \frac{1 + \tanh[(x-c_m)/d_m]}{2}\Bigg\}. \end{aligned} \tag{119}$$

This form also decouples the high-density behavior from the low-density regime, which proved crucial for fitting to HIC data on the behavior of dense nucleonic matter.

In addition to the hyperons, BHB14 and DD2Y also add the ϕ meson, whose contribution to the Lagrangian is similar in form to the ω's and which contributes a repulsive force between hyperons [44, 145]. This supports the higher maximum NS mass needed to avoid the hyperon puzzle; BHB14 has a maximum mass of 2.10 $M_\odot$, whereas without ϕ it would be an unacceptably low 1.95 $M_\odot$ [44].

The couplings of hyperons to the ω and ϕ mesons are set by $\mathrm{SU}(3)_f$ symmetry in terms of the

mixing angle θ from the ideal octet and singlet isoscalar states, the coupling ratio $z = g_8/g_1$ between these states, and the ratio $\alpha = F/(D+F)$ which relates the antisymmetric (F) and symmetric (D) coupling modes in $\mathbf{8} \otimes \mathbf{8} \to \mathbf{8}$ processes [153]; they may be computed using SU(3) CG coefficients [154]. Explicitly [145, 155]:

$$\begin{aligned}
g_{\omega N} &\propto 1 - \frac{z}{\sqrt{3}}(1-4\alpha)\tan\theta, \quad & g_{\phi N} &\propto -\tan\theta - \frac{z}{\sqrt{3}}(1-4\alpha), \\
g_{\omega \Lambda} &\propto 1 - \frac{2z}{\sqrt{3}}(1-\alpha)\tan\theta, \quad & g_{\phi \Lambda} &\propto -\tan\theta - \frac{2z}{\sqrt{3}}(1-\alpha), \\
g_{\omega \Sigma} &\propto 1 + \frac{2z}{\sqrt{3}}(1-\alpha)\tan\theta, \quad & g_{\phi \Sigma} &\propto -\tan\theta + \frac{2z}{\sqrt{3}}(1-\alpha), \\
g_{\omega \Xi} &\propto 1 - \frac{z}{\sqrt{3}}(1+2\alpha)\tan\theta, \quad & g_{\phi \Xi} &\propto -\tan\theta - \frac{2z}{\sqrt{3}}(1+2\alpha).
\end{aligned} \tag{120}$$

In $\mathrm{SU}(6)_{sf}$, $z = 1/\sqrt{6}$, $\theta = \arctan(1/\sqrt{2}) \approx 35.3°$, and $\alpha = 1$. Empirically, $\theta_V = 36.5°$ is close to the ideal mixing for vector mesons [1]. In particular, nucleons do not couple to ϕ, and the couplings are proportional to valence-quark contents. The breaking of the $\mathrm{SU}(6)_{sf}$ to approximate $\mathrm{SU}(3)_f$ in nature is mostly due to the $s\bar{s}$ condensate inside the proton as seen in LQCD simulations, via which the ϕ can couple to nucleons [153]. The quark model allows $0 \le z \le 2/\sqrt{6}$ and $0 \le \alpha \le 1$ for $q\bar{q}$ mesons [153], allowing us to choose between varying z and varying α. We chose the former, which we found to be sufficient to calibrate U_Λ and U_{Σ^0}.

Some models also attempt to introduce an attractive $f_0(980)$ meson (variously abbreviated as σ^*, σ_s, or ζ) which couples only to hyperons and has a similar Lagrangian term as the σ's. However, we do not include $f_0(980)$ in our model, and neither do BHB14 or DD2Y, because the $\Lambda\Lambda$ two-body force is poorly measured but known to be much weaker than the ΛN force [44, 118, 41]; an attempt by the authors of DD2Y to include it lowered the maximum NS mass from 2.04 $M_\odot$ to 1.87 $M_\odot$ [145]. As such, we do not include $\mathrm{SU}(3)_f$ relations for the scalar sector and leave $g_{\sigma i}/g_{\sigma N}$ as free parameters.

The $a_0(980)$ meson, or δ, has also been used in hadronic models [151]. It has a similar Lagrangian

term as the σ, except with isospin:

$$\mathcal{L}_\delta = \sum_{i\in B} \overline{\psi}_i (g_{\delta i} \boldsymbol{\tau}_i \cdot \boldsymbol{\delta}) \psi_i + \frac{1}{2}(\partial_\mu \boldsymbol{\delta} \cdot \partial^\mu \boldsymbol{\delta} - m_\delta^2 \boldsymbol{\delta} \cdot \boldsymbol{\delta}), \tag{121}$$

which averages to isolate the third isospin component (the δ^0 meson):

$$\mathcal{L}_\delta = \sum_{i\in B} \overline{\psi}_i (g_{\delta i} \tau_{3i} \delta_3) \psi_i - \frac{1}{2} m_\delta^2 \delta_3^2, \tag{122}$$

and therefore we can abbreviate δ_3 as δ, and its EoM is

$$\delta_3 = \frac{1}{m_\delta^2} \sum_i g_{\delta i} \tau_{3i} n_i^s. \tag{123}$$

We do not include the δ in the model due to poor constraints on the nucleon effective Landau mass splitting [156], and some RMF models predict a relatively smaller coupling compared to the ρ [157].

Since the ρ's are octet mesons, the $\mathrm{SU}(3)_f$ relations for the ρ^0 are proportional to z, but otherwise depend only on α:[10]

$$\begin{aligned}
g_{\rho N}\tau_{3N} &= g_1 z\, 8\sqrt{3}\, C^{1/2,t_{3N}}_{1/2,t_{3N};1,t_{3\rho}} = 4 g_1 z\, \tau_{3N}, \\
g_{\rho\Lambda} &= 0, \\
g_{\rho\Sigma}\tau_{3\Sigma} &= g_1 z\, 8\sqrt{2}\, \alpha\, C^{1,t_{3\Sigma}}_{1,t_{3\Sigma};1,t_{3\rho}} = 4 g_1 z\, \alpha\, \tau_{3\Sigma}, \\
g_{\rho\Xi}\tau_{3\Xi} &= g_1 z\, 8\sqrt{3}(-1+2\alpha)\, C^{1,t_{3\Xi}}_{1,t_{3\Xi};1,t_{3\rho}} = 4 g_1 z(-1+2\alpha)\tau_{3\Xi},
\end{aligned} \tag{124}$$

where $C^{J,M}_{j_1,m_1;j_2,m_2}$ is an SU(2) CG coefficient. However, the ρ effective coupling tends to vary differently than the ω's in nuclear matter [159, 152], and the HALQCD isospin splitting of the Σ and Ξ multiplets in neutron matter is too small to be explained if there is only a ρ meson with $\alpha = 1$, so we do not extend $\mathrm{SU}(3)_f$ to the ρ and adjust $g_{\rho i}/g_{\rho N}$ as free parameters. Nonetheless, the combination of ρ and δ mesons should allow $\mathrm{SU}(3)_f$ to be restored to the ρ sector.

[10] Refs. [154, 158] quote a $g_{\rho\Sigma}$ which is twice this value, which incorrectly compensates for the Σ's having $\tau = 2$. Proper handling of the SU(2) CG coefficients should yield $g_{\rho\Sigma} = \alpha g_{\rho N}$, as we do here and as quoted by Ref. [155] for the $\mathrm{SU}(6)_{sf}$ case.

The model also includes an electron gas whose charge density cancels out that of the baryons. Based on the energy in a Coulomb gas,

$$E = \frac{2.2099 \text{ Ry}}{r_s^2} - \frac{0.9163 \text{ Ry}}{r_s} + O\left(\frac{1}{\sqrt{r_s}}\right) \tag{125}$$

where $r_s = a_0(3/4\pi n)^{1/3}$ and 1 Ry $\approx$ 13.6 eV is the Rydberg unit. Since $n_e \gg a_0^{-3}$ (about 7×10^{-15} fm^{-3}) even at the lowest density in the model, Coulomb interactions between electrons are negligible and we can treat the electrons as an ideal Fermi gas [86]. The muon can also be treated as such above $n_\mu \gg (m_\mu/m_e)^3 a_0^{-3} \approx 6 \times 10^{-8}$ fm^{-3}.

7.2 Isospin dependence

A major weakness of the BHB14 and DD2Y models is that the U_Λ cannot be accurately fitted to the predicted potential in neutron matter.

Theorem 2. *In cold, dense nuclear matter with equal nucleon masses, $\sum_i n_i^s$ for neutron matter is asymptotically $2^{-1/3}$ times that of symmetric matter at the same density.*

Proof. For $T = 0$, the density and scalar density of a fermion field are:

$$n = \frac{d}{2\pi^2}\int_0^{k_F} k^2 dk = \frac{dk_F^3}{6\pi^2} \tag{126}$$

$$n^s = \frac{d}{2\pi^2}\int_0^{k_F} k^2 dk \frac{m}{\sqrt{k^2+m^2}} = \frac{d}{4\pi^2}\left(mk_F\sqrt{k_F^2+m^2} - m^3 \operatorname{arcsinh}\frac{k_F}{m}\right) \tag{127}$$

where k_F is the Fermi momentum. At low k_F, Taylor expansion of Eq. (127) gives [149]:

$$\begin{aligned} n^s &\sim \frac{d}{4\pi^2}\left[m^2 k_F\left(1+\frac{k_F^2}{2m^2}\right) - m^3\left(\frac{k_F}{m} - \frac{k_F^3}{6m^3}\right)\right] \\ &= \frac{d}{4\pi^2}\left(\frac{k_F^3}{2} + \frac{k_F^3}{6}\right) = \frac{dk_F^3}{6\pi^2} = n \end{aligned} \tag{128}$$

Meanwhile, at high k_F, the asymptotic form $\operatorname{arcsinh} x \sim \ln(2x)$ gives

$$\begin{aligned} n^s &\sim \frac{d}{4\pi^2}\left[-m^3 \ln\frac{2k_F}{m} + mk_F^2\left(1+\frac{m^2}{2k_F^2}\right)\right] = \frac{d}{4\pi^2}\left(mk_F^2 + \frac{m^3}{2} - m^3\ln\frac{2k_F}{m}\right) \\ &\sim \frac{d}{4\pi^2} m\left(\frac{6\pi^2 n}{d}\right)^{2/3} = \left(\frac{9d}{16\pi^2}\right)^{1/3} mn^{2/3} \end{aligned} \tag{129}$$

Then for dense nuclear matter at fixed n_B and Y_q, the ratio of $\sum_i n_i^s$ between this state and neutron matter is

$$\frac{n_B^s(Y_q)}{n_B^s(0)} \sim \frac{(Y_q n_B)^{2/3} + [(1-Y_q)n_B]^{2/3}}{n_B^{2/3}} = Y_q^{2/3} + (1-Y_q)^{2/3}. \tag{130}$$

At $Y_q = 1/2$, this ratio equals $2 \times (1/2)^{2/3} = 2^{1/3}$. □

Since ω depends only on n_B and Λ does not couple to ρ, there are no degrees of freedom for Y_q dependence of U_Λ in nuclear matter; once n_B and Y_q are fixed, both σ and the σ-dependent term of Σ^r are completely determined. In DD2Y and BHB14, we find that U_Λ is actually deeper in neutron matter (Fig. 15), which is the opposite of what's predicted by HALQCD [2]!

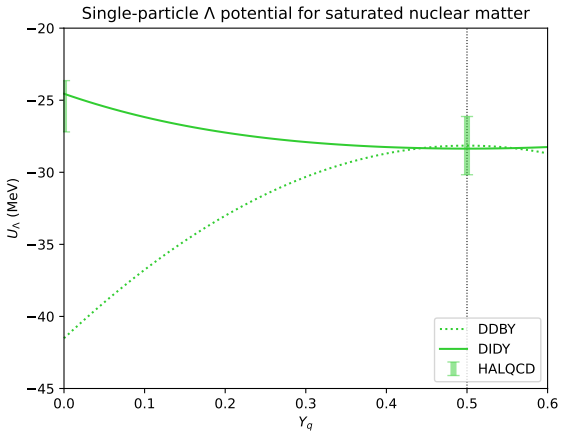

Figure 15: Plot of U_Λ at saturation density as a function of Y_q for DDBY and our new model, DID, that includes isospin-dependent couplings, versus the U_Λ estimates from Ref. [2].

In a nonlinear density-independent RMF, the Y_q dependence of σ in nuclear matter per Theorem 2 would also change the values of other meson fields that couple to σ. DBHF models also tend to predict isospin-dependent effective couplings due to Fock terms [152]. Therefore, we resolve

this by introducing an additional isospin-dependent term into the couplings. Let $\beta = \sum_i \tau_{3i} n_i / n_B$. For all mesons, we interpolate over β^2 between two copies of Eq. (119) with different parameters, for symmetric matter ($\beta = 0$) and neutron matter ($\beta = -1$), but also modified to ensure isospin independence at zero density, so that Σ^t vanishes at zero density:

$$g_{mi}(n_B, \beta) = g_{mi}^{S(0)} a_m \frac{1 + b_m(x + d_m)^2}{1 + c_m(x + d_m)^2} \left(1 - \beta^2 \tanh \frac{x}{e}\right) + g_{mi}^{N(0)} a_m \frac{1 + b_m(x + d_m)^2}{1 + c_m(x + d_m)^2} \beta^2 \tanh \frac{x}{e}. \tag{131}$$

We set $e = 1/3$ to preserve nuclear clusters against the sparse medium at low density and temperature. We extrapolate this form if we reach a regime with $|\beta| > 1$ for strange nuclear matter. Because pressure and energy are roughly quadratic in β for nuclear matter [16], we do not introduce isospin dependence for the ρ; doing so would cause the ρ field's pressure to scale non-quadratically in β and introduce unacceptable discrepancy between S_2 and S (L_2 and L).

7.3 Thermodynamic and microscopic properties

The baryonic part of the mean-field Lagrangian (Eq. (111) with an extra ϕ term) consists of the sum of several Dirac equations:

$$\mathcal{L}_B = \sum_{i \in B} \overline{\psi}_i (i\partial\!\!\!/ - m_i + g_{\sigma i}\sigma - g_{\omega i}\gamma^0\omega - g_{\phi i}\gamma^0\phi - g_{\rho i}\gamma^0\tau_{3i}\rho)\psi_i \tag{132}$$

By comparing this formula to the Dirac equation in a generic four-potential V_μ [3],

$$\mathcal{L} = \overline{\psi}(i\partial\!\!\!/ - m - \gamma^\mu V_\mu)\psi, \tag{133}$$

we immediately conclude that the Dirac effective mass within this DD-RMF is

$$m_i^* = m_i - \Sigma_i^s = m_i - g_{\sigma i}\sigma. \tag{134}$$

There is also a Landau effective mass, which is not used internally but can be correlated with empirical measurements [160, 161]:

$$\begin{aligned} m_i^L &= k_{Fi}\left[\frac{\partial E_{ki}^*}{\partial k}\right]_{k=k_{Fi}}^{-1} = k_{Fi}\left(\frac{\partial}{\partial k}\left[\sqrt{m_i^{*2}+k^2}+U\right]_{k=k_{F_i}}\right)^{-1} \\ &= k_{Fi}\left(\frac{k_{Fi}}{\sqrt{m_i^{*2}+k_{Fi}^2}}\right)^{-1} = \sqrt{m_i^{*2}+k_{Fi}^2} = \sqrt{m_i^{*2}+\left(\frac{6\pi^2 n_i}{d_i}\right)^{2/3}} \end{aligned} \tag{135}$$

However, the chemical potential receives an effective correction from the rearrangement terms Σ^r and Σ^t [102], which we will explain later:

$$\nu_i = \mu_i - \Sigma_i^v = \mu_i - g_{\omega i}\omega - g_{\phi i}\phi - g_{\rho i}\tau_{3i}\rho - \Sigma^r - (\tau_{3i}-\beta)\Sigma^t \tag{136}$$

The single-particle potential in RMF is then [145]:

$$U_i = \Sigma_i^v - \Sigma_i^s = -g_{\sigma i}\sigma + g_{\omega i}\omega + g_{\phi i}\phi + g_{\rho i}\tau_{3i}\rho + \Sigma^r + (\tau_{3i}-\beta)\Sigma^t \tag{137}$$

Given the occupation fraction for fermions at single-particle energy $E_{ki}^* = \sqrt{k^2+m_i^{*2}}$,

$$f_i(k) = \frac{1}{e^{(E_{ki}^*-\nu_i)/T}+1}, \tag{138}$$

the density and scalar density of a particular baryon species, not including antibaryons, is [44]:

$$n_i = \frac{d_i}{2\pi^2}\int_0^\infty k^2 dk f_i, \tag{139}$$

$$n_i^s = \frac{d_i}{2\pi^2}\int_0^\infty k^2 dk f_i \frac{m_i^*}{E_{ki}^*}, \tag{140}$$

and the energy density, including the meson fields f_m, is [44]:

$$\epsilon = \sum_{m\in M}\frac{1}{2}m_m f_m^2 + \frac{d_i}{2\pi^2}\int_0^\infty k^2 dk f_i E_{ki}^*. \tag{141}$$

The meson fields have no entropy, so the entropy per unit volume reduces to that from the Gibbs entropy formula:

$$s_i = -\frac{d_i}{2\pi^2}\int_0^\infty k^2 dk[f_i \ln f_i + (1-f_i)\ln(1-f_i)] \tag{142}$$

The baryon energy-density term can also be converted using the easily-derived relation

$$\frac{E^*_{ki} - \nu_i}{T} = \ln\frac{1-f_i}{f_i} \tag{143}$$

into

$$\epsilon_i = \frac{d_i}{2\pi^2}\int_0^\infty k^2 dk f_i \left(T\ln\frac{1-f_i}{f_i} + \nu_i\right). \tag{144}$$

From the Euler relation, we can then calculate the pressure:

$$\begin{aligned}
P &= \sum_{i\in B}\mu_i n_i + Ts_i - \epsilon \\
&= \sum_i \left\{\mu_i \frac{d_i}{2\pi^2}\int_0^\infty k^2 dk f_i - \frac{d_i T}{2\pi^2}\int_0^\infty k^2 dk[f_i\ln f_i + (1-f_i)\ln(1-f_i)]\right\} \\
&\quad - \frac{1}{2}\sum_{m\in M} m_m^2 f_m^2 - \sum_i \frac{d_i}{2\pi^2}\sum_0^\infty k^2 dk f_i\left(T\ln\frac{1-f_i}{f_i} + \nu_i\right) \\
&= -\frac{1}{2}\sum_m m_m^2 f_m^2 + \sum_i\left\{(\mu_i - \nu_i)n_i - \frac{d_i T}{2\pi^2}\int_0^\infty k^2 dk\left[\ln(1-f_i) + f_i\ln\frac{f_i}{1-f_i} - f_i\ln\frac{1-f_i}{f_f}\right]\right\} \\
&= \sum_i\Bigg[-\frac{1}{2}(g_{\sigma i}n_i^s\sigma + g_{\omega i}n_i\omega + g_{\phi i}n_i\phi + g_{\rho i}\tau_{3i}n_i\rho) + n_i(g_{\omega i}\omega + g_{\phi i}\phi + g_{\rho i}\tau_{3i}\rho + \Sigma^r + (\tau_{3i}-\beta)\Sigma^t) \\
&\qquad - \frac{d_i T}{2\pi^2}\int_0^\infty k^2 dk\ln(1-f_i)\Bigg] \\
&= \frac{1}{2}(-m_\sigma^2\sigma^2 + m_\omega^2\omega^2 + m_\phi^2\phi^2 + m_\rho^2\rho^2) + \sum_i\left[n_i\Sigma^r + \Sigma^t\sum_i n_i(\tau_{3i}-\beta) + \frac{d_i T}{2\pi^2}\int_0^\infty k^2 dk\ln\frac{1}{1-f_i}\right] \\
&= \frac{1}{2}(-m_\sigma^2\sigma^2 + m_\omega^2\omega^2 + m_\phi^2\phi^2 + m_\rho^2\rho^2) + n_B\Sigma^r + \Sigma^t\sum_i n_i(\tau_{3i}-\beta) \\
&\quad + \sum_i \frac{d_i T}{2\pi^2}\int_0^\infty k^2 dk\ln[1 + e^{-(E^*_{ki}-\nu_i)/T}] \\
&= \frac{1}{2}(-m_\sigma^2\sigma^2 + m_\omega^2\omega^2 + m_\phi^2\phi^2 + m_\rho^2\rho^2) + n_B\Sigma^r + \Sigma^t\sum_i n_i(\tau_{3i}-\beta) + \sum_i P_i.
\end{aligned}$$

We find that $\partial P_i/\partial \nu_i = n_i$ and $\partial P_i/\partial m_i^* = -n_i^s$, which can be verified by differentiating the integral with respect to this variable.

The antibaryons have effective chemical potential exactly opposite of the corresponding baryon,

$$\overline{f}_i(k) = \frac{1}{e^{(E_{ki}^* + \nu_i)/T} + 1} \tag{145}$$

so after including the antibaryons, the various thermodynamic quantities become [44]:

$$\begin{aligned} P = &\frac{1}{2}(-m_\sigma^2\sigma^2 + m_\omega^2\omega^2 + m_\phi^2\phi^2 + m_\rho^2\rho^2) + n_B\Sigma^r + \Sigma^t\sum_i n_i(\tau_{3i} - \beta) \\ &+ \sum_i \frac{d_i T}{2\pi^2}\int_0^\infty k^2 dk(\ln[1 + e^{-(E_{ki}^* - \nu_i)/T}] + \ln[1 + e^{-(E_{ki}^* + \nu_i)/T}]) \end{aligned} \tag{146}$$

$$n_i = \frac{d_i}{2\pi^2}\int_0^\infty k^2 dk(f_i - \overline{f}_i) \tag{147}$$

$$n_i^s = \frac{d_i}{2\pi^2}\int_0^\infty k^2 dk \frac{m_i^*}{E_{ki}^*}(f_i + \overline{f}_i)] \tag{148}$$

$$\epsilon = \frac{1}{2}\sum_m m_m^2 f_m^2 + \sum_i \frac{d_i}{2\pi^2}\int_0^\infty k^2 dk E_{ki}^*(f_i + \overline{f}_i) \tag{149}$$

$$s = \sum_i \frac{d_i}{2\pi^2}\int_0^\infty k^2 dk E_{ki}^* \left[f_i \ln f_i + \overline{f}_i \ln \overline{f}_i + (1 - f_i)\ln(1 - f_i) + (1 - \overline{f}_i)\ln(1 - \overline{f}_i)\right] \tag{150}$$

7.3.1 Rearrangement term

Thermodynamic consistency requires that at $T = 0$, $\mu_i = \partial\epsilon/\partial n_i$ for each $i \in B$, which allows us to solve for the rearrangement terms Σ^r and Σ^t. In this proof, we will consider a generic model where g_{mi} is inferred to contain a necessary τ_{3i} factor. Then, ignoring leptons:

$$\begin{aligned} \mu_i &= \sum_{s\in S} m_s^2 f_s \frac{\partial f_s}{\partial n_i} + \sum_{v\in V} m_v^2 f_v \frac{\partial f_v}{\partial n_i} + \sum_j \frac{\partial \epsilon_j}{\partial n_i} \\ &= \sum_{sj} n_j^s g_{sj}\frac{\partial f_s}{\partial n_i} + \sum_{vj} f_v\left(g_{vj}\frac{\partial n_j}{\partial n_i} + n_j\frac{\partial g_{vj}}{\partial n_i}\right) + \sum_j \frac{\partial \epsilon_j}{\partial n_i} \\ &= \sum_{sj} n_j^s g_{sj}\frac{\partial f_s}{\partial n_i} + \sum_{vj} f_v n_j \frac{\partial g_{vj}}{\partial n_i} + \sum_v f_v g_{vi} + \sum_j \frac{\partial \epsilon_j}{\partial n_i} \end{aligned} \tag{151}$$

where ϵ_i is the integral in Eq. (149). The derivative in ϵ_j expands as:

$$\frac{\partial \epsilon_j}{\partial n_i} = \left(\frac{\partial \epsilon_j}{\partial n_i}\right)_{m_j^*} + \frac{d_j}{2\pi^2}\int_0^{k_{Fj}} k^2 dk \frac{m_j^*}{E_{kj}^*}\frac{\partial m_j^*}{\partial n_i} = \delta_{ij}\nu_j - n_j^s \sum_s \left(g_{si}\frac{\partial f_s}{\partial n_i} + \frac{\partial g_s}{\partial n_i} f_s\right). \tag{152}$$

Substituting back in, we get:

$$\mu_i = \nu_i + \sum_v f_v g_{vi} - \sum_{sj} n_j^s g_{si}\frac{\partial g_{sj}}{\partial n_i} + \sum_{vj} f_v n_j \frac{\partial g_{vj}}{\partial n_i}. \tag{153}$$

Since our EoS's meson couplings depend only on baryon and isospin density, each partial derivative expands as

$$\frac{\partial}{\partial n_i} = \frac{\partial}{\partial n_B} + \frac{\partial}{\partial n_i}\frac{\sum_j \tau_{3j} n_j}{n_B}\frac{\partial}{\partial \beta} = \frac{\partial}{\partial n_B} + \frac{\tau_{3i} n_B - \sum_j \tau_{3j} n_j}{n_B^2}\frac{\partial}{\partial \beta} = \frac{\partial}{\partial n_B} + \frac{\tau_{3i} - \beta}{n_B}\frac{\partial}{\partial \beta}. \tag{154}$$

This means that there are two copies of the latter two terms in Eq. (153): one with $\partial/\partial n_B$ and the other with $(\tau_{3i} - \beta)\partial/\partial\beta$. Comparing to Eq. (136), our rearrangement terms are thus:

$$\Sigma^r = \sum_i \left(-\sum_s \frac{\partial g_{si}}{\partial n_B} f_s n_i^s + \sum_v \frac{\partial g_{vi}}{\partial n_B} f_v n_i\right) \tag{155}$$

$$\Sigma^t = \frac{1}{n_B}\sum_i \left(-\sum_s \frac{\partial g_{si}}{\partial \beta} f_s n_i^s + \sum_v \frac{\partial g_{vi}}{\partial \beta} f_v n_i\right). \tag{156}$$

7.3.2 Chemical equilibrium

There are four independent charges that are conserved by the electromagnetic and strong forces within $N_f = 3$ QCD: baryon number, electric charge, strangeness, and lepton number. Based on this, chemical equilibrium (attained in around $\sim 10^{-23}$ s) allows us to fix the baryon chemical potential from each, and we can also define a lepton chemical potential if neutrinos have escaped.

$$\mu_i = \mu_B + Q_i\mu_Q + S_i\mu_S \tag{157}$$

$$\mu_e = \mu_L - \mu_Q \tag{158}$$

We also include the criterion that $\mu_S = 0$, since this charge equilibrates via the weak force on a timescale of $\sim 10^{-10}$ s [118], and in cold NS matter, electrons and muons are in equilibrium with each other on timescales longer than a few milliseconds. (Tauons are equilibrated on similar timescales as strangeness, but, like charm quarks, are too massive to occur in the hadronic phase.) Since neutrinos are light enough to escape the NS, cold β-equilibrium, which takes several seconds to reach, would enforce $\mu_L = 0$ (equivalent to $\mu_p + \mu_n = \mu_e$ in nucleonic matter). Actual SN and NS-merger simulations assume that leptons are not in chemical equilibrium, and as such nuclear EoS's built for this purpose are typically calculated with electrons only [44].

7.4 The HS model of the NS crust

In general, pressure (excluding leptons) of a symmetric-matter RMF is negative below saturation density, and the saturation density is defined as the point where the hadronic pressure is zero [149]. Therefore, the RMF is unstable and decomposes spinodally into a sparse gas and small nuclear clusters. Because of nuclear shell effects, the masses of the clusters are not the same as an equal-volume chunk of nuclear matter; the beta-decay rate of low-density nuclear matter is also sensitive to the properties of the clusters. Therefore, Hempel and Schaffner-Bielich invented a model [45], hereforth called HS, which self-consistently includes these clusters into the NS crust.

7.4.1 Composition

The HS model assumes that below saturation density, finite nuclei with $A \geq 2$ are embedded as a non-relativistic van der Waals gas with Coulomb interactions within an RMF sea of unbound nucleons [45]. The nuclei float freely in the nuclear fluid, which therefore causes a volume exclusion effect on the latter. Although the fluid is a quantum system, it can also be treated for $n_B < n_0$ as a liquid with free nucleons floating through empty space (Fig. 16). In this picture, we can describe their relative mole fractions in terms of two quantities: the fraction $\kappa = 1 - n_B/n_0$ of empty space,

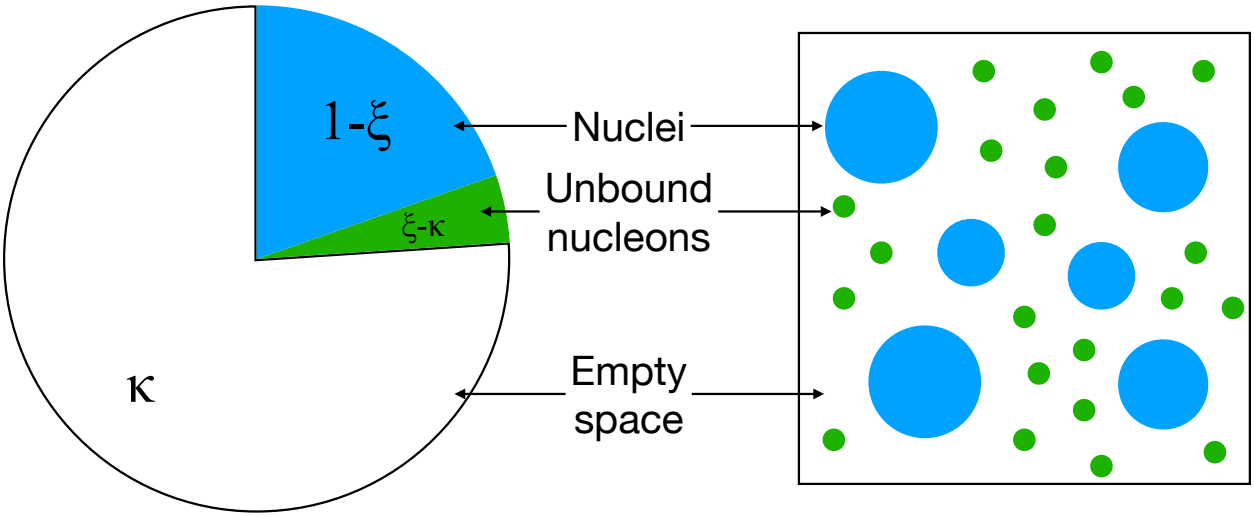

Figure 16: Cartoon representation of the DD2 model as a heterogeneous mixture of unbound nucleons (green) and bound nuclei (blue), and the corresponding fractions of space.

and the fraction of space that is not occupied by nuclei,

$$\xi = 1 - \frac{1}{n_0} \sum_{AZ} A n_{AZ}. \tag{159}$$

If $n_B \geq n_0$, then there are no nuclei and the HS model becomes a pure RMF.

We can define n_i' as the density of unbound nucleons within the space unoccupied by nuclei, so that

$$n_B = \xi(n_p' + n_n') + \sum_{AZ} A n_{AZ} \tag{160}$$

$$n_p = \xi n_p' + \sum_{AZ} Z n_{AZ} \tag{161}$$

$$n_n = \xi n_n' + \sum_{AZ} (A - Z) n_{AZ} \tag{162}$$

We can also calculate the baryon fractions X_i for *free* baryons and clusters:

$$X_p = \xi n'_p / n_B \tag{163}$$

$$X_n = \xi n'_n / n_B \tag{164}$$

$$X_A = \sum_{AZ} A n_{AZ} / n_B. \tag{165}$$

We will also define the *total* baryon fraction Y_i of a specific baryon species, so that:

$$Y_p = X_p + \sum_{AZ} Z n_{AZ} / n_B \tag{166}$$

$$Y_n = X_n + \sum_{AZ} (A - Z) n_{AZ} / n_B \tag{167}$$

Y_p is also the same as the charge fraction Y_q. In RMF, there are no clusters, and the definitions of X_i and Y_i coincide.

The original version of HS (which used a nonlinear RMF called TMA) [45] and the authors of BHB14 [44] calculated X_A separately for $Z \leq 5$ and $Z \geq 6$. Their CompOSE tables instead isolated the fraction of nuclei with $A \leq 4$. We have not implemented either of those statistics here. However, we will use the average nuclear properties as a proxy for the overall composition of the system, such as for the various sublayers of the NS crust:

$$\langle A \rangle = \frac{\sum_{AZ} A n_{AZ}}{\sum_{AZ} n_{AZ}} \tag{168}$$

$$\langle Z \rangle = \frac{\sum_{AZ} Z n_{AZ}}{\sum_{AZ} n_{AZ}} \tag{169}$$

BHB14 included nuclei only up to $T = 50$ MeV; at higher temperatures, nuclei are sparse and anti-nuclei contribute to the EoS at low densities, so we also include this cutoff in our model.

We use the AME20 mass table (including systematic extrapolations, which are expected to be more accurate than theoretical models) and the FRDM12 droplet model for unknown nuclei with $Z, N \geq 8$ and $A \leq 339$ [4, 5], instead of the older AME03 and FRDM92 tables that BHB14 used

[44]. We cut off the table at the neutron drip line (including S_n or S_{2n}), but not the proton drip line; with this exclusion, there are 8244 nuclei within our model (Fig. 17). Since the mass values in nuclear tables include electron clouds and the nuclei in HS do not have them, we apply the additional post-hoc mass correction using the semi-empirical formula from FRDM12 [5]

$$m_{AZ} = m^0_{AZ} - Zm_e - cZ^p \tag{170}$$

where $c = 14.33$ eV and $p = 2.39$. However, nuclear binding energies and the position of the drip line are not subject to this correction.

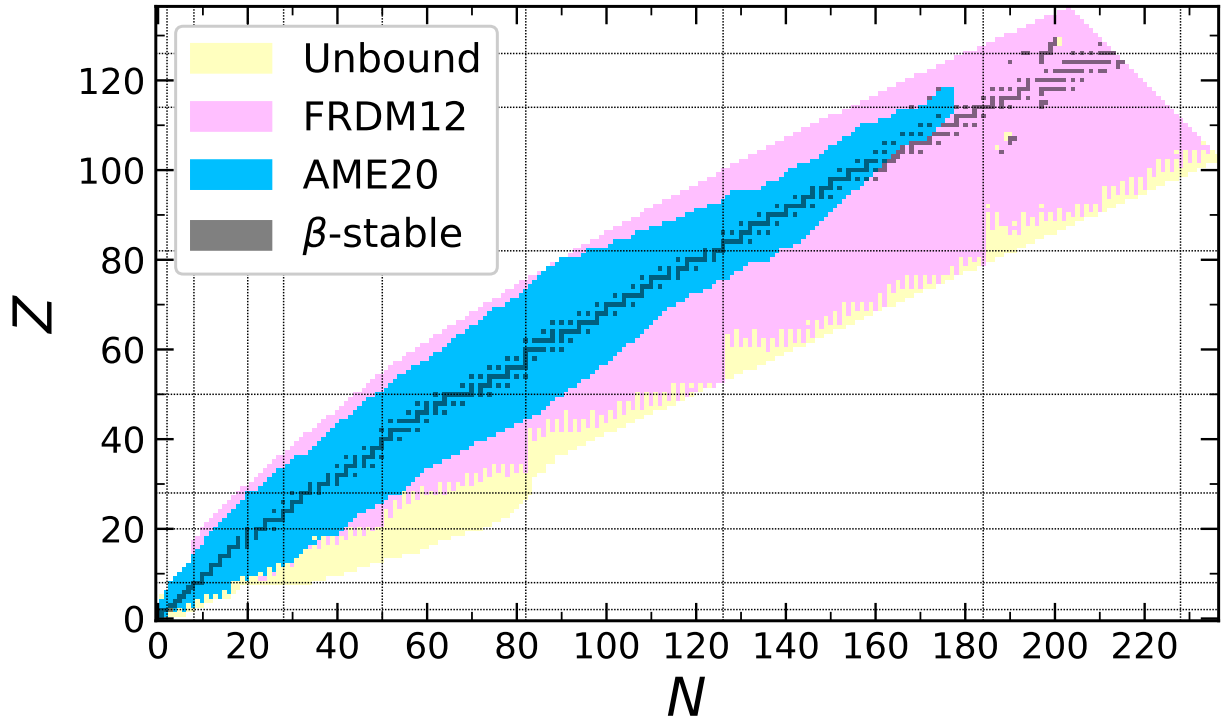

Figure 17: The table of nuclides used in our model; masses from AME20 are in blue and masses from FRDM12 are in pink; light-yellow nuclei are excluded by the neutron-drip cutoff. The β-stable nuclei are also shaded in dark colors.

7.4.2 Nuclear properties

Nuclei are often not perfect spheres, but up to the $A = 339$ cutoff, most are rounded enough that in DD2, we can treat the nuclei as spherical with nucleon density equal to n_0 [45]. This implies a radius of

$$R_{AZ} = \left(\frac{3A}{4\pi n_0}\right)^{1/3}. \tag{171}$$

Then the Coulomb energy of the nucleus can be determined from the density of electrons in the surrounding medium. This formula is

$$\begin{aligned} E^c_{AZ} &= -\frac{3}{10}\frac{Z^2\alpha}{R_{AZ}}(3x - x^3) \\ x &= \left(\frac{n_e A}{n_0 Z}\right)^{1/3} \end{aligned} \tag{172}$$

where $\alpha = 0.0072973525643(11)$ [62] is the fine-structure constant, and $n_e = Y_p n_B$ is the density of electrons in the system.

Instead of computing the large number of energy levels for each nucleus, the partition function of an individual nucleus is handled using the semi-empirical model of Fai & Randrup (1982) [45]:

$$g_{AZ} = g^0_{AZ} + \frac{c_1}{A^{5/3}}\int_0^{B_{AZ}} e^{-E/T+\sqrt{2aE}}dE, \tag{173}$$

where B_{AZ} is the binding energy before applying the mass correction in Eq. (170),

$$a = \frac{A}{c_2}(1 - c_3 A^{-1/3}), \tag{174}$$

g^0_{AZ} is the spin degeneracy of the ground state, $c_1 = 0.2$ MeV^{-1}, $c_2 = 8$ MeV, and $c_3 = 0.8$. Spin degeneracies are obtainable from NUBASE20 [70] for the empirical and systematic nuclei, and Ref. [162] for the theoretical FRDM12 nuclei or where the NUBASE20 spin assignment of the ground state is unknown or uncertain (e.g. ^{45}Ar).

In HS, we can compute the following effective chemical potential for nuclei in terms of properties

of the RMF at n_i', hereforth denoted by a superscript zero:

$$\nu_{AZ} = Z\mu_p^0 + (A-Z)\mu_n^0 - m_{AZ} - E_{AZ}^c - P^0 V_{AZ} \tag{175}$$

We will also define the coefficient

$$L_{AZ} = \kappa g_{AZ} \left(\frac{m_{AZ}T}{2\pi}\right)^{3/2}, \tag{176}$$

Then the number density of a nucleus is:

$$n_{AZ} = L_{AZ} e^{\nu_{AZ}/T}. \tag{177}$$

7.4.3 Thermodynamic properties

In addition to the unbound nucleons, the nuclei contribute to the pressure as in an ideal gas, plus the Coulomb interaction [45]:

$$P_{AZ} = \frac{T n_{AZ}}{\kappa} + P_{AZ}^c \tag{178}$$

where

$$P_{AZ}^c = -\frac{3}{10} n_{AZ} \frac{Z^2 \alpha}{R_{AZ}} (x - x^3) \tag{179}$$

and x is the same as in Eq. (172). Therefore (not including electrons),

$$P = P^0(T, n_i') + \sum_{AZ} P_{AZ}. \tag{180}$$

The chemical potentials of the nucleons receive a correction due to the presence of the nuclei [45]:

$$\mu_i = \mu_i^0(T, n_i') + \frac{1}{\kappa} \sum_{AZ} \frac{T n_{AZ}}{n_0}. \tag{181}$$

The nuclei receive a correction as well, compared to the van der Waals gas, due to both the nucleons

and the Coulomb interaction:

$$\mu_{AZ} = m_{AZ} - T \ln \frac{L_{AZ}}{n_{AZ}} + E^c_{AZ} + V_{AZ} \left[P^0(T, n'_i) + \frac{T}{\kappa} \sum_{AZ} n_{AZ} \right]. \tag{182}$$

The formula for n_{AZ} in Eq. (177) comes from setting $\mu_{AZ} = Z\mu_p + (A - Z)\mu_n$. Free energy can be computed for each nucleus as:

$$f_{AZ} = n_{AZ} \left[m_{AZ} - T \left(1 + \ln \frac{L_{AZ}}{n_{AZ}} \right) \right] + n_{AZ} E^c_{AZ} \tag{183}$$

Then the total free energy is:

$$f = \sum_{AZ} f_{AZ} + \xi f^0(T, n'_i). \tag{184}$$

The entropy of nuclei in the system is:

$$s_{AZ} = n_{AZ} \left(\frac{5}{2} + \frac{T}{g_{AZ}} \frac{\partial g_{AZ}}{\partial T} + \ln \frac{L_{AZ}}{n_{AZ}} \right). \tag{185}$$

Then

$$s = \xi s^0(T, n'_i) + \sum_{AZ} s_{AZ}. \tag{186}$$

Finally, the energy density of nuclei is:

$$\epsilon_{AZ} = n_{AZ} \left(m_{AZ} + \frac{3}{2} T + \frac{T^2}{g_{AZ}} \frac{\partial g_{AZ}}{\partial T} \right) + n_{AZ} E^c_{AZ}. \tag{187}$$

Then the full energy density due to hadrons is given by

$$\epsilon = \xi \epsilon^0(T, n'_i) + \sum_{AZ} \epsilon_{AZ}. \tag{188}$$

The $\ln(L_{AZ}/n_{AZ})$ term in the entropy density diverges to $-\infty$ at zero temperature, so HS cannot be used to model $T = 0$. Nonetheless, $T = 0.1$ MeV is often a close approximation to the zero-temperature crust, which requires inter-nuclear forces such as that which results in crystallization

[45].

The properties of electrons in HS are identical to the ideal gas, except for their chemical potential, which is corrected by the Coulomb interaction with the nuclei:

$$\mu_e = \mu_e^0(T, n_e) + \frac{1}{n_e} \sum_{AZ} P_{AZ}^c \tag{189}$$

where μ_e^0 is the ideal chemical potential from the RMF model. No formulae of HS describing either the nuclei or the Coulomb energy change if muons are admixed, since only the total lepton density enters these expressions.

7.4.4 Microscopic properties

In addition to the properties computed by HS [45], we also computed the potentials and effective masses of particles in the crust using a crude model designed for intermediate temperature. While free neutrons scatter off the nuclear pasta clumps at low temperatures [163], high-energy nucleons can scatter through unoccupied levels in the clumps, and hyperons (while not present) can simply pass through since they ignore the Pauli exclusion principle with respect to nucleons.

The single-particle potential in HS is corrected from uniform matter due to the non-uniform nuclear forces in the medium. In this case, we must use first-order perturbation theory to calculate the effect on energy eigenstates. In a homogeneous system with fixed volume and assuming the Hartree approximation, this is simply

$$\psi_k(x) = \frac{1}{\sqrt{V}} e^{i[\mathbf{k}\cdot\mathbf{x} - (E_k^* + \gamma^0 U)t]}, \tag{190}$$

where $E_k^* = \sqrt{k^2 + m^{*2}}$. It turns out that at first order, the perturbed ground-state energy depends only on the shifted potential U' in the system:

$$U' = U + \frac{1}{V} \int d^3\mathbf{x}\, \Delta U(\mathbf{x}). \tag{191}$$

In particular, the interaction potential can be unambiguously shifted by the total contribution of all the nuclei in the system:

$$\begin{aligned} U_i &= U_i(\mathbf{n}') + \sum_{AZ} n_{AZ}\Delta_i^{AZ} \\ \Delta_i^{AZ} &= \int d^3\mathbf{x} U_i^{AZ}(\mathbf{x}). \end{aligned} \tag{192}$$

The Δ_i^{AZ} is model-dependent, but to avoid introducing any new parameters, we modeled the U_i^{AZ} as a finite spherical well filled with RMF with the same absolute depth as in vacuum, continuing the cartoon model from Fig. 16:

$$U_i^{AZ}(\mathbf{x}) = \left[U_i\left(n_0, \frac{Z}{A}\right) - U_i(\mathbf{n}')\right]\theta(R_{AZ} - r), \tag{193}$$

where θ is the Heaviside function. As such,

$$U_i = \xi U_i(\mathbf{n}') + \sum_{AZ} U_i(n_0, Z/A) V_{AZ} n_{AZ}. \tag{194}$$

It is highly tedious to calculate $U_i(n_0, Z/A)$ for ≈ 8000 nuclei and ≈ 5000 distinct Z/A values.[11] In practice, the range of nuclei is often small, and the Y_q dependence of the meson fields is close to linear. Then we can approximate $U_i(n_0, Y_q)$ as linear in Y_q, in which case

$$\begin{aligned} U_i &\approx \xi U_i(\mathbf{n}') + \sum_{AZ}\left(c_0 + c_1\frac{Z}{A}\right) V_{AZ} n_{AZ} \\ &= \xi U_i(\mathbf{n}') + \sum_{AZ} \frac{n_{AZ}}{n_0}(c_0 A + c_1 Z) \\ &= \xi U_i(\mathbf{n}') + \frac{1}{n_0}(c_0\langle A\rangle + c_1\langle Z\rangle)\sum_{AZ}\frac{n_{AZ}}{n_0} \\ &= \xi U_i(\mathbf{n}') + \frac{1}{n_0}\left(c_0 + c_1\frac{\langle Z\rangle}{\langle A\rangle}\right)\sum_{AZ}\frac{A n_{AZ}}{n_0}, \end{aligned}$$

or:

$$U_i \approx \xi U_i(\mathbf{n}') + (1-\xi) U_i\left(n_0, \frac{\langle Z\rangle}{\langle A\rangle}\right). \tag{195}$$

[11] Around $6/\pi^2$ times the total number of nuclei, by an elementary result on the GCD [164]. Our table of nuclides contains exactly 5005 distinct Z/A values, including the two nucleons.

where $\mathbf{n}'$ is shorthand for all the n_i''s. Qualitatively, this approximation shuffles the nucleons uniformly between the clusters, so that they all have the same Z/A.

In contrast, the Hartree approximation no longer holds — the energy $E_k^* = \sqrt{k^2+m^2} + \gamma^0\Sigma_i^v$ of the particle is an average of E_k^* over all space, which in general is not that of a free particle:

$$\begin{aligned} E_k^* &= \xi E_{ki}^*(\mathbf{n}') + \sum_{AZ} E_{ki}^*\left(n_0, \frac{Z}{A}\right) V_{AZ} n_{AZ} \\ &\approx \xi E_{ki}^*(\mathbf{n}') + (1-\xi) E_{ki}^*\left(n_0, \frac{\langle Z\rangle}{\langle A\rangle}\right). \end{aligned} \tag{196}$$

This means that Σ_i^s varies with momentum. To derive the Dirac mass, we compare the Dirac equation [161]

$$(\not{k} - m_i^* + \gamma^0\Sigma_i^v)u_k = 0 \tag{197}$$

to Eq. (196), from which we infer:

$$E_{ki}^* = \sqrt{k^2 + m_i^{*2}} + \gamma^0\Sigma_i^v \tag{198}$$

Since the vector potential in RMF contains no momentum-dependent terms, Σ_i^v does not vary with momentum, and it has the same form as Eq. (196). Then the Dirac mass at momentum $\mathbf{k}$ is:

$$\begin{aligned} m_i^*(k) &= \sqrt{(E_{ki}^* - \gamma^0\Sigma_i^v)^2 - k^2} \\ &= \left\{ \left[\xi\sqrt{k^2 + m_i^*(\mathbf{n}')^2} + \sum_{AZ} \sqrt{k^2 + m_i^*\left(n_0, \frac{Z}{A}\right)^2} V_{AZ} n_{AZ} \right]^2 - k^2 \right\}^{1/2} \\ &\approx \left\{ \left[\xi\sqrt{k^2 + m_i^*(\mathbf{n}')^2} + (1-\xi)\sqrt{k^2 + m_i^*\left(n_0, \frac{\langle Z\rangle}{\langle A\rangle}\right)^2} \right]^2 - k^2 \right\}^{1/2}. \end{aligned} \tag{199}$$

It is straightforward to verify that at zero momentum, m_i^* is an average over the whole material and has a similar form as Eq. (196).

Landau effective mass is the harmonic mean of $\sqrt{m_i^{*2} + k_{Fi}^2}$ over the whole volume, where k_F

is for the whole material and m^* is the Dirac effective mass at each point:

$$\begin{aligned} m_i^L = k_{Fi}\left[\frac{\partial E_{ki}^*}{\partial k}\right]_{k=k_{Fi}}^{-1} &= \left[\frac{\xi}{\sqrt{k_{Fi}^2 + m_i^*(\mathbf{n}')^2}} + \sum_{AZ}\frac{V_{AZ}n_{AZ}}{\sqrt{k_{Fi}^2 + m_i^*(n_0, Z/A)^2}}\right]^{-1} \\ &\approx \left[\frac{\xi}{\sqrt{k_{Fi}^2 + m_i^*(\mathbf{n}')^2}} + \frac{1-\xi}{\sqrt{k_{Fi}^2 + m_i^*(n_0, \langle Z\rangle/\langle A\rangle)^2}}\right]^{-1}. \end{aligned} \tag{200}$$

7.4.5 Maxwell transition

In principle, HS is fully thermodynamically consistent if the RMF is consistent and the table of nuclides is complete. In principle, at low temperatures $\langle A\rangle$ and $\langle Z\rangle$ should increase without limit, and X_A should approach unity, as the baryon density approaches saturation density, but we applied a cutoff of $A \leq 339$ on our table, so states with $\langle A\rangle > 339$ need to be approximated [45]. Additionally, some nuclei with $A > 339$ are strongly non-spherical — in particular, the authors of Ref. [84] predict regions of donut-shaped nuclei near $^{342}136$ and $^{466}156$ — and the denser phases of nuclear pasta should also have non-spherical clusters, including infinite clumps with shapes such as spaghetti strands or lasagna sheets [35]. Therefore, HS applies a Maxwell construction across the liquid-gas transition, which seems to be consistent with simulations of the pasta phase's structure [45]; both phases have local charge neutrality (equal Y_q) and are in thermal equilibrium, and the pressure P and the "total" chemical potential defined by

$$\mu = (\mu_p + \mu_e)Y_q + \mu_n(1 - Y_q) = \mu_B + Y_q\mu_L \tag{201}$$

are equal at both endpoints of the transition. Pressure and μ are constant, so c_s is zero within the transition zone; the surface tension of the boundary between the two phases is infinite [113]. The volumes of the two phases change linearly with density across the phase transition from the less dense phase to the more dense one [165]. This contrasts with the Gibbs construction, where Y_q is not locally fixed (but still *globally* conserved), the transition is smooth [165], and the phase boundary has zero surface tension [113].

Theorem 3. *In a consistent nucleonic RMF, μ increases monotonically with density at fixed T.*

Proof. Close inspection of Eq. (201) finds that it is equal to Gibbs energy per baryon (including electrons):

$$\frac{g}{n_B} = \frac{1}{n_B}\left(\sum_{i\in N}\mu_i n_i + \mu_e n_e\right) = \sum_i \mu_i Y_i + \mu_e Y_q = \mu_p Y_q + \mu_n(1-Y_q) + \mu_e Y_q = \mu. \tag{202}$$

Now consider the differential

$$dG = -SdT + VdP + \mu dN, \tag{203}$$

where G is total Gibbs energy of the system so $\mu = G/N$. If N and T are constant (the latter imposed by baryon-number conservation), then the requirement from mechanical stability that $(\partial P/\partial n)_{N,T} \geq 0$ implies that

$$\left(\frac{\partial\mu}{\partial n}\right)_{T,N} = -\frac{V^2}{N^2}\left(\frac{\partial G}{\partial V}\right)_{T,N} = -\frac{V^3}{N^2}\left(\frac{\partial P}{\partial V}\right)_{T,N} = \frac{V}{N}\left(\frac{\partial P}{\partial n}\right)_{T,N} = \frac{1}{n}\left(\frac{\partial P}{\partial n}\right)_{T,N} \geq 0. \tag{204}$$

□

Because of this result, the transition between the liquid and gas phases at fixed T and Y_q can thusly be calculated geometrically by finding the intersection of their (P,μ)-curves. We can also use the above theorem to check the consistency of a nucleonic RMF with electrons; the Maxwell transition may fail if this is not true below n_0.

8 Implementation

The DDRMF program is written in Python and C++; the main algorithm is written in Python, while some frequent, arduous tasks are compiled in C++. The C++ modules connect to the main Python code via Swig and are compiled with CMake; they require the GNU Scientific Library (GSL) for certain calculations. All C++ functions and global variables named in their associated header (`*.h`) files can be accessed from `fermi.py`. The main algorithm, `bhb14.py`, calculates and

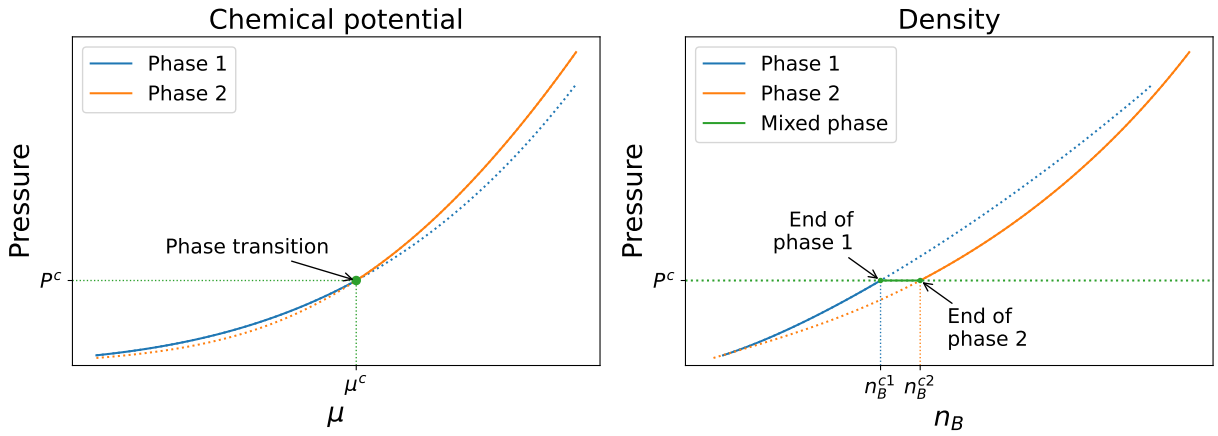

Figure 18: Schematic for the construction of the Maxwell transition between a lower-density phase 1 and the higher-density phase 2. At all μ's except the transition, the stable phase is the one with higher pressure; the actual (P, μ)-curve of the system will be the solid line.

records the EoS.

8.1 Input files

8.1.1 Mesons, baryons, and leptons

The file `props.dat` defines and names the baryons, mesons, and leptons. The first row contains the saturation density (in fm^{-3}); and then the number of baryons, mesons, and leptons. In this section, the number of types of particle will be designated as N_B for baryons, N_m for mesons, and N_L for leptons. Each row contains the name (in plaintext and TEX) of a particle: first the baryons, then the mesons, and finally the leptons. The architecture of the program requires that the proton be listed first, and then the neutron.

Because all leptons have charge -1, the only tunable property of the leptons is their masses, and it is stored in `leptons.dat`. The baryons are stored in `baryons.dat`, which includes the following information:

0. Mass (in MeV).

1. Spin degeneracy. This is always an even number, like all fermions; the ground-state octet has

$d = 2$ and the ground-state decuplet has $d = 4$.

2. Doubled isospin τ_3.

3. Charge (in multiples of e).

4. Strangeness (not currently used).

Lastly, the mesons are stored in `mesons.dat`. Each meson occupies $N_B + 1$ rows. The first row in each block includes the mass in MeV, spin degeneracy ($d = 1$ for scalars and $d = 3$ for vectors), and isospin degeneracy ($e = 1$ for isoscalars and $e = 3$ for isovectors). Then each subsequent row includes the couplings of that meson to the ith baryon:

0. An integer code for the type of density dependence (Table 5).

1–2. g_0 and g_1 (respectively, for $\beta = 0$ and $\beta = \pm 1$).

3–6. Shape parameters a_0, b_0, c_0, d_0 for $\beta = 0$.

7–10. Shape parameters a_1, b_1, c_1, d_1 for $\beta = \pm 1$.

The data within these files are read and accessed within `gm.py`. Importing `config.py` at the beginning of a Python program will automatically load these data.

8.1.2 Nuclei

The program `mass_1.py` automatically combines AME and theoretical mass tables, with AME data overriding theoretical data where it exists, into `nuclei.dat`. Both the inputs and the output are formatted as a table containing Z, A, m_{AZ} (in micro-u), and ground-state spin degeneracy. The micro-u can be converted to MeV via the conversion [62]:

$$1\ \mu\text{u} = 9.3149410372(29) \times 10^{-4}\ \text{MeV}. \tag{205}$$

The output table is sorted in increasing order of A, then by Z, which places the neutron first and hydrogen second.

The data in `nuclei.dat` are processed and accessed in `az.py`. It computes one composite quantity, the binding energy B_{AZ}, that is used in the model. Masses are stored internally in MeV, and are subject to the FRDM bare-nucleus correction in Eq. (170). Entries are checked for duplicate nuclei and nuclei with negative binding energy, which may yield undesirable results.

8.2 Couplings

Four types of meson-coupling density dependence are available (Table 5), and are indexed by integer codes. The equations themselves, and their derivatives, are stored in `couplings.cpp`. The isospin dependence is always of the form

$$g_{mi}(n_B,\beta) = \left(1-\beta^2\tanh\frac{x}{e}\right) f(n_B; g_0, a_0, b_0, c_0, d_0) + \beta^2 \tanh\frac{x}{e} f(n_B; g_1, a_1, b_1, c_1, d_1), \qquad (206)$$

where $\beta = \sum_{i\in B} \tau_{3i} Y_i$ is the isospin fraction, and $e = 1/3$ is fixed. The coupling constants and its derivatives in n_B and β are accessible in `gm.py` via the method `ghiif`.

Table 5: List of available density-dependencies for the couplings, where $x = n_B/n_0$.

Code	Label	Form
10	`poly`	$g(a+bx+cx^2+dx^3)$
11	`witch`	Eq. (115)
12	`expo`	Eq. (116)
13	`fermilike`	$g\frac{a}{e^{bx}+1}$
14	`stretch`	Eq. (117)
15	`pareto`	$g\left[b+(1-b)\left(\frac{x+1}{2}\right)^{-2a}\right]$
16	`modstretch`	$g\left\{b+(1-b)\exp\left[1-\left(\frac{x+1}{2}\right)^{2a}\right]\right\}$
17	`comstretch`	$g\left\{c+(1-c)\exp\left[1-\left(\frac{x+1}{b+1}\right)^{(b+1)a}\right]\right\}$
18	`modstretcht`	Eq. (119)
19	`modstretchsp`	$g\left\{\exp\left[1-\left(\frac{x+1}{2}\right)^{2a}\right]+b\ln\left[1+e^{(x-c)/d}\right]\right\}$

8.3 Fermi integrals

In the ideal Fermi gas, we can define the integral

$$H_k(\eta,\mu) := \int_0^\infty x^k dx \ln\left(1+e^{\eta-\sqrt{x^2+\mu^2}}\right), \tag{207}$$

so that the pressure is [44]:

$$\begin{aligned} P &= \frac{dT}{2\pi^2}\int_0^\infty k^2 dk \left\{\ln\left[1+e^{-(E_k-\mu)/T}\right]+\ln\left[1+e^{-(E_k+\mu)/T}\right]\right\} \\ &= \frac{dT^4}{2\pi^2}\left[H_2\left(\frac{\mu}{T},\frac{m}{T}\right)+H_2\left(-\frac{\mu}{T},\frac{m}{T}\right)\right] \end{aligned} \tag{208}$$

This integral converges if $k > -1$, and we will also introduce the variable

$$E = \sqrt{x^2+\mu^2}. \tag{209}$$

We will introduce a general notation for derivatives of H, collectively Fermi integrals, with respect to its parameters:

$$H_k^{mn}(\eta,\mu) := \frac{\partial^{m+n}}{\partial\eta^m\partial\mu^n}H_k(\eta,\mu) \tag{210}$$

The H integral itself is then $H_k^{00}(\eta,\mu)$. For $m>0$ or $n>0$, this will be an integral expression with an integrand involving rational functions of E, μ, and $e^{\eta-E}$. We will also define for an ideal Fermi gas the quantities

$$P^{mn} = \frac{\partial^{m+n}P}{\partial^m\mu\partial^n m} = \frac{dT^{4-m-n}}{2\pi^2}\left[H_2^{mn}\left(\frac{\mu}{T},\frac{m}{T}\right)+(-1)^m H_2^{mn}\left(-\frac{\mu}{T},\frac{m}{T}\right)\right]. \tag{211}$$

The density $n = P^{10}$ and the scalar density $n^s = -P^{01}$; higher-order P^{mn}'s have no special name.

At $T=0$, the expression for P in Eq. (208) becomes indeterminate. However, we do have an

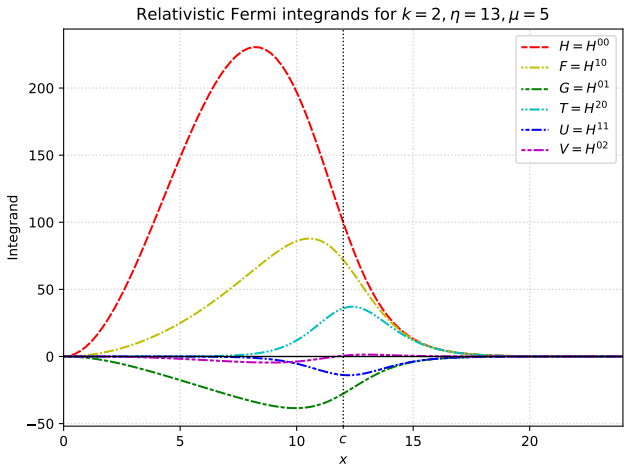

Figure 19: Plot of the relativistic Fermi integrands up to second order for $k = 2$, $\eta = 13$, and $\mu = 5$. For these parameters, $c = \sqrt{\eta^2 - \mu^2}$ is exactly 12.

identity for the ramp function, derivable using l'Hôpital's rule:

$$\begin{aligned} R(x) &:= \begin{cases} x, & x \geq 0 \\ 0, & x < 0 \end{cases} \\ &= \lim_{T \to 0^+} T \ln(1 + e^{x/T}) = \lim_{T \to 0^+} \frac{x}{1 + e^{-x/T}}. \end{aligned} \tag{212}$$

Therefore, we may define:

$$\begin{aligned} \hat{H}_k(\eta, \mu) &:= \lim_{t \to 0^+} T^{k+2} H_k\left(\frac{\eta}{T}, \frac{\mu}{T}\right) = \lim_{t \to 0^+} T^{k+2} \int_0^\infty x^k dx \ln\left(1 + e^{\eta/T - \sqrt{x^2 + (\mu/T)^2}}\right) \\ &= \lim_{t \to 0^+} T \int_0^\infty u^k du \ln\left[1 + e^{\left(\eta - \sqrt{u^2 + \mu^2}\right)/T}\right] = \begin{cases} 0, & \eta \leq |\mu| \\ \int_0^c x^k (\eta - E), & \eta > |\mu|, \end{cases} \end{aligned} \tag{213}$$

where $c := \sqrt{\eta^2 - \mu^2}$. Then

$$\begin{aligned} P &= \frac{dT}{2\pi^2} \int_0^\infty k^2 dk \left[R(\mu - E_k) + R(-\mu - E_k)\right] \\ &= \frac{d}{2\pi^2} \left[\hat{H}_2\left(\frac{\mu}{T}, \frac{m}{T}\right) + \hat{H}_2\left(-\frac{\mu}{T}, \frac{m}{T}\right)\right], \end{aligned} \tag{214}$$

and $\hat{H}^{mn}$ and the $T = 0$ expression for P^{mn} can be constructed as derivatives of $\hat{H}$, analogously to the $T > 0$ case.

Each integral we use will need its own implementation, but we conjecture that all H^{mn} integrals can be split in a similar manner as the H integral, with two small parts involving $e^{\eta - E}$ and an analytically evaluable large part which is a scaled version of the $\hat{H}^{mn}$ integral. The C++ file `FermiIntegrals.cpp` includes Fermi integrals up to second order.

8.3.1 Fermi H integral (H^{00})

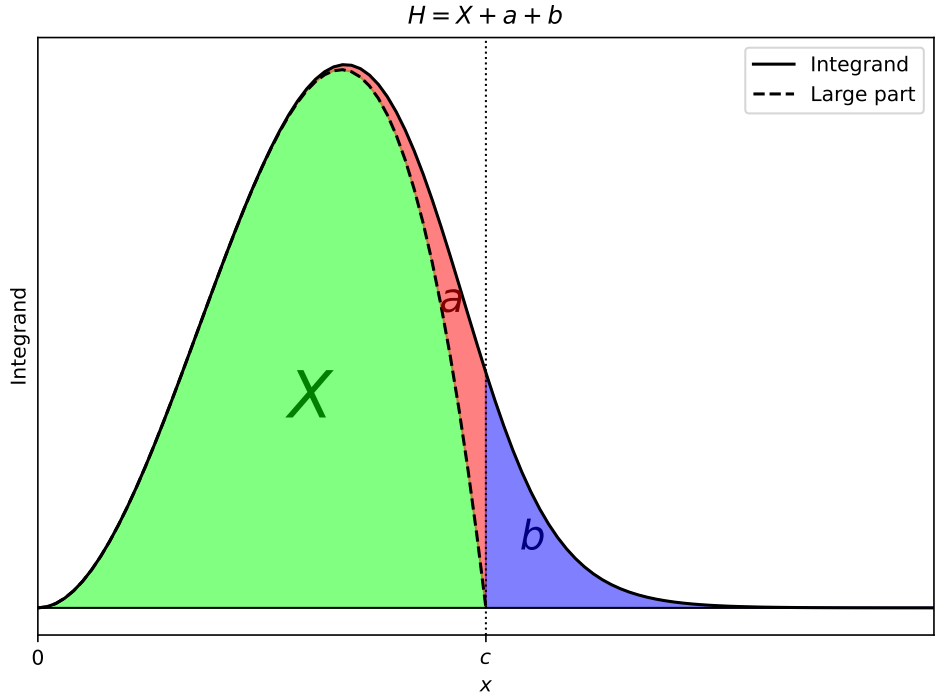

Figure 20: Decomposition of the Fermi H integral into a large part (X) and two small parts (a and b) if $\eta > |\mu|$.

If $\eta \leq |\mu|$, then the exponential factor in the integrand is small, and we can efficiently evaluate the H integral directly. Otherwise, we will divide the integral into two parts by cutting at c, where the exponent is zero. Then using the identity

$$\ln(1 + e^a) = a + \ln(e^{-a} + 1), \tag{215}$$

the H integral can be split into two small parts and a large part (Fig. 20):

$$\begin{aligned} H_k(\eta,\mu) &= \int_0^c x^k dx \ln\left(1+e^{\eta-E}\right) + \int_c^\infty x^k dx \ln\left(1+e^{\eta-E}\right) \\ &= \int_0^c x^k dx(\eta-E) + \int_0^c x^k dx \ln\left(1+e^{E-\eta}\right) + \int_c^\infty x^k dx \ln\left(1+e^{\eta-E}\right) \\ &= \int_0^c x^k dx(\eta-E) + \int_0^c x^k dx \ln\left(1+e^{E-\eta}\right) + \int_c^\infty x^k dx \ln\left(1+e^{\eta-E}\right). \end{aligned} \tag{216}$$

The large part can be evaluated analytically using a hypergeometric function:

$$\int_0^c x^k dx(\eta-E) = \frac{c^{k+1}}{k+1}\left[\eta - \mu\ {}_2F_1\left(-\frac{1}{2}, \frac{k+1}{2}; \frac{k+3}{2}; -\frac{c^2}{\mu^2}\right)\right], \tag{217}$$

but in the actual code it is evaluated numerically using ordinary quadrature.

8.3.2 Fermi F integral (H^{10})

The Fermi F integral is the first derivative of H with respect to η:

$$F_k(\eta,\mu) = H_k^{10}(\eta,\mu) = \int_0^\infty \frac{x^k dx}{e^{E-\eta}+1}. \tag{218}$$

The F integral is small and easy to evaluate if $\eta \le |\mu|$. Using the identity

$$\frac{1}{e^a+1} = \frac{1}{2}\left(1 - \tanh\frac{x}{2}\right), \tag{219}$$

we can break the F integrand in a similar manner as H if $\eta > |\mu|$, with the largest part having a simple analytic expression (Fig. 21):

$$\begin{aligned} F_k(\eta,\mu) &= \int_0^\infty \frac{x^k}{2} dx \left(1 - \tanh\frac{E-\eta}{2}\right) \\ &= \int_0^c x^k dx + \int_0^c \frac{x^k}{2} dx \left(-1 - \tanh\frac{E-\eta}{2}\right) + \int_c^\infty \frac{x^k dx}{e^{E-\eta}+1} \\ &= \frac{c^{k+1}}{k+1} - \int_0^c \frac{x^k dx}{e^{\eta-E}+1} + \int_c^\infty \frac{x^k dx}{e^{E-\eta}+1}. \end{aligned} \tag{220}$$

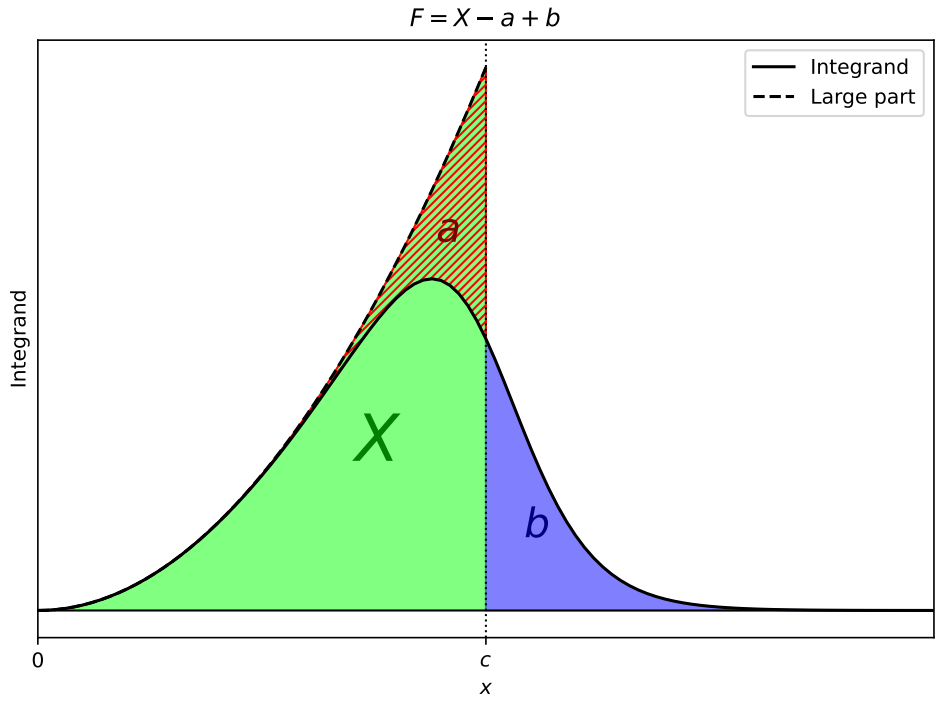

Figure 21: Same as Fig. 20, but for the F integral. Hatched regions have negative signed area.

Also, assuming $\eta > |\mu|$,

$$\hat{F}_k(\eta,\mu) = \hat{H}_k^{10}(\eta,\mu) = \int_0^c x^k dx = \frac{c^{k+1}}{k+1}. \tag{221}$$

The density of an ideal Fermi gas can be expressed in terms of F integrals:

$$\begin{aligned} n &= \frac{d}{2\pi^2}\int_0^\infty k^2 dk \left\{ \left[e^{(E_k-\mu)/T}+1\right]^{-1} + \left[e^{(E_k+\mu)/T}+1\right]^{-1} \right\} \\ &= P^{10} = \frac{dT^3}{2\pi^2}\left[F_2\left(\frac{\mu}{T},\frac{m}{T}\right) - F_2\left(-\frac{\mu}{T},\frac{m}{T}\right)\right] \end{aligned} \tag{222}$$

8.3.3 Fermi G integral (H^{01})

The Fermi G integral is the first derivative of H with respect to μ:

$$G_k(\eta,\mu) = H_k^{01}(\eta,\mu) = -\int_0^\infty \frac{\mu}{E}\frac{x^k dx}{e^{E-\eta}+1}. \tag{223}$$

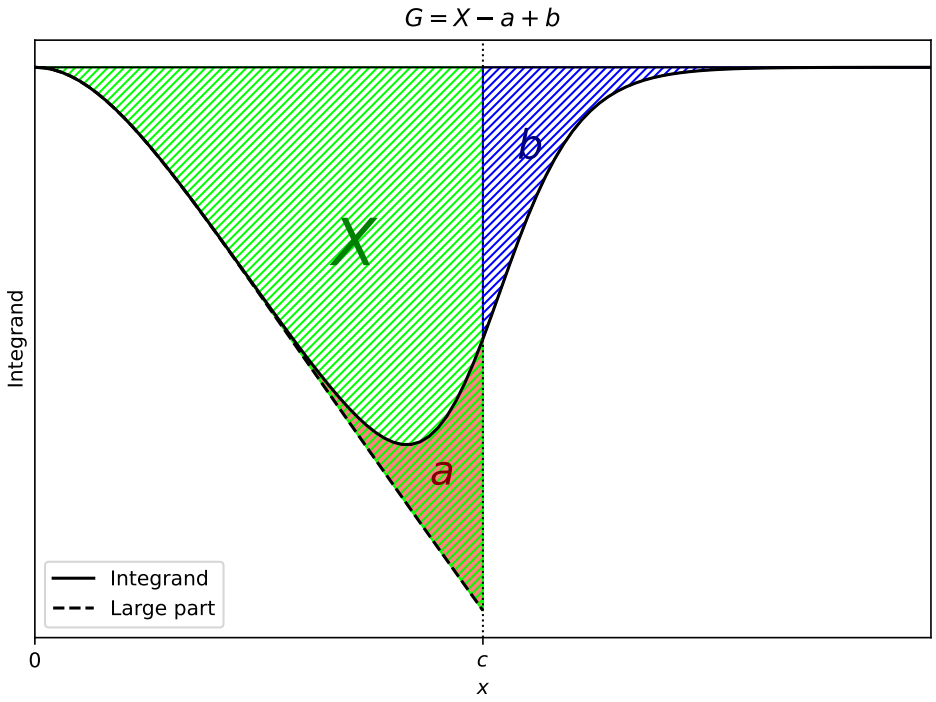

Figure 22: Same as Figs. 20 and 21, but for the G integral.

For $\eta > |\mu|$, the G integral can be split in a similar manner as F (Fig. 22):

$$\begin{aligned} G_k(\eta,\mu) &= -\int_0^\infty \frac{x^k\mu}{E}dx\left(1-\tanh\frac{E-\eta}{2}\right) \\ &= -\int_0^c \frac{x^k\mu}{E}dx - \int_0^c \frac{x^k\mu}{2E}dx\left(-1-\tanh\frac{E-\eta}{2}\right) - \int_c^\infty \frac{\mu}{E}\frac{x^k dx}{e^{E-\eta}+1} \\ &= -\int_0^c \frac{x^k\mu}{E}dx + \int_0^c \frac{\mu}{E}\frac{x^k dx}{e^{\eta-E}+1} - \int_c^\infty \frac{\mu}{E}\frac{x^k dx}{e^{E-\eta}+1}. \end{aligned} \tag{224}$$

The largest term in Eq. (224) can be evaluated analytically using hypergeometric functions, but in the actual code it is computed numerically:

$$\int_0^c \frac{x^k\mu}{E}dx = \frac{c^{k+1}}{k+1}\,\mathrm{sgn}(\mu)\;{}_2F_1\left(\frac{1}{2},\frac{k+1}{2};\frac{k+3}{2};-\frac{c^2}{\mu^2}\right). \tag{225}$$

The $T = 0$ form for $\eta > |\mu|$ requires an application of the Leibniz integral rule, but the term derived

from differentiating the upper limit of integration is zero:

$$\hat{G}_k(\eta,\mu) = -\int_0^c \frac{x^k\mu}{E}dx + \frac{\partial c}{\partial \mu}c^k\left(\eta - \sqrt{c^2+\mu^2}\right) = -\int_0^c \frac{x^k\mu}{E}dx. \tag{226}$$

The scalar density of an ideal Fermi gas can be expressed in terms of G integrals:

$$\begin{aligned} n^s &= \frac{d}{2\pi^2}\int_0^\infty k^2 dk \frac{m}{E_k}\left\{\left[e^{(E_k-\mu)/T}+1\right]^{-1} + \left[e^{(E_k+\mu)/T}+1\right]^{-1}\right\} \\ &= -P^{01} = -\frac{dT^3}{2\pi^2}\left[G_2\left(\frac{\mu}{T},\frac{m}{T}\right) + G_2\left(-\frac{\mu}{T},\frac{m}{T}\right)\right] \end{aligned} \tag{227}$$

Also, algebraic manipulation of the formula for energy density yields an expression in G integrals:

$$\begin{aligned} \epsilon &= \frac{d}{2\pi^2}\int_0^\infty k^2 dk E_k\left\{\left[e^{(E_k-\mu)/T}+1\right]^{-1} + \left[e^{(E_k+\mu)/T}+1\right]^{-1}\right\} \\ &= \frac{d}{2\pi^2}\int_0^\infty k^2 dk \frac{k^2+m^2}{E_k}\left\{\left[e^{(E_k-\mu)/T}+1\right]^{-1} + \left[e^{(E_k+\mu)/T}+1\right]^{-1}\right\} \\ &= -\frac{d}{2\pi^2}\left\{mT^3\left[G_2\left(\frac{\mu}{T},\frac{m}{T}\right) + G_2\left(-\frac{\mu}{T},\frac{m}{T}\right)\right] + \frac{T^5}{m}\left[G_4\left(\frac{\mu}{T},\frac{m}{T}\right) + G_4\left(-\frac{\mu}{T},\frac{m}{T}\right)\right]\right\}. \end{aligned} \tag{228}$$

Then entropy can be written as:

$$\begin{aligned} s &= \frac{\epsilon - \mu n + P}{T} \\ &= \frac{d}{2\pi^2}\Big\{T^3\left[H_2\left(\frac{\mu}{T},\frac{m}{T}\right) + H_2\left(-\frac{\mu}{T},\frac{m}{T}\right)\right] - \mu T^2\left[F_2\left(\frac{\mu}{T},\frac{m}{T}\right) - F_2\left(-\frac{\mu}{T},\frac{m}{T}\right)\right] \\ &\qquad + mT^2\left[G_2\left(\frac{\mu}{T},\frac{m}{T}\right) + G_2\left(-\frac{\mu}{T},\frac{m}{T}\right)\right] + \frac{T^4}{m}\left[G_4\left(\frac{\mu}{T},\frac{m}{T}\right) + G_4\left(-\frac{\mu}{T},\frac{m}{T}\right)\right]\Big\}. \end{aligned} \tag{229}$$

8.3.4 Fermi T integral (H^{20})

Define

$$T_k(\eta,\mu) := H_k^{20}(\eta,\mu) = \int_0^\infty x^k dk \frac{e^{E-\eta}}{(e^{E-\eta}+1)^2} = \int_0^\infty \frac{x^k dk}{4\cosh^2\left[(E-\eta)/2\right]} \tag{230}$$

In this case, the entire integrand is small with a peak around $x = c$, and the integral can be evaluated directly. It is more numerically accurate to split the integral at c, since quadrature over

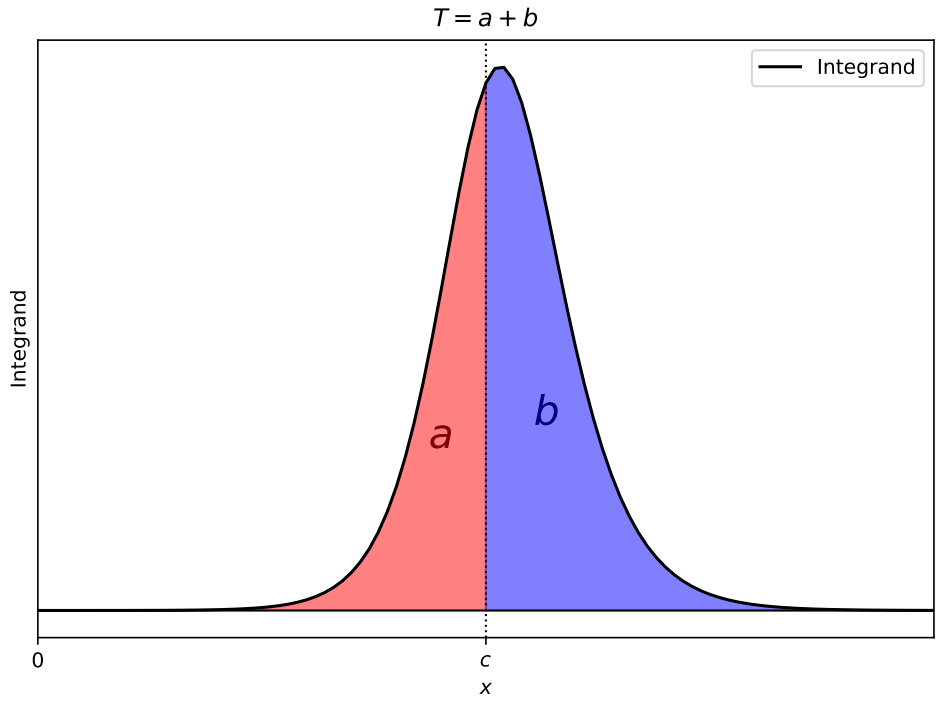

Figure 23: Same as Figs. 20–22, but for the T integral.

the full integral may incompletely capture the peak (Fig. 23). A special result is:

$$\hat{T}_k(\eta,\mu) = \frac{\partial}{\partial\eta}\hat{F}_k(\eta,\mu) = c^k\frac{\partial c}{\partial\eta} = \eta c^{k-1}. \tag{231}$$

The T integral is used in the Jacobian of the root-finder that solves for ν_i given n_i (Section 8.4). Additionally, at low density and high temperature, ν/T is small and this leads to large truncation errors in the calculation of n_i via Eq. (147). In this case, we may use the asymptotic form for $\nu/T \lesssim 10^{-5}$:

$$\begin{aligned} n &= \nu_i P^{20}(\nu, m^*) + O\left[\left(\frac{\nu}{T}\right)^3\right] \\ &= \frac{d_i T^2 \nu}{2\pi^2}\left[T_2\left(\frac{\nu}{T}, \frac{m^*}{T}\right) + T_2\left(-\frac{\nu}{T}, \frac{m^*}{T}\right)\right] + O\left[\left(\frac{\nu}{T}\right)^3\right]. \end{aligned} \tag{232}$$

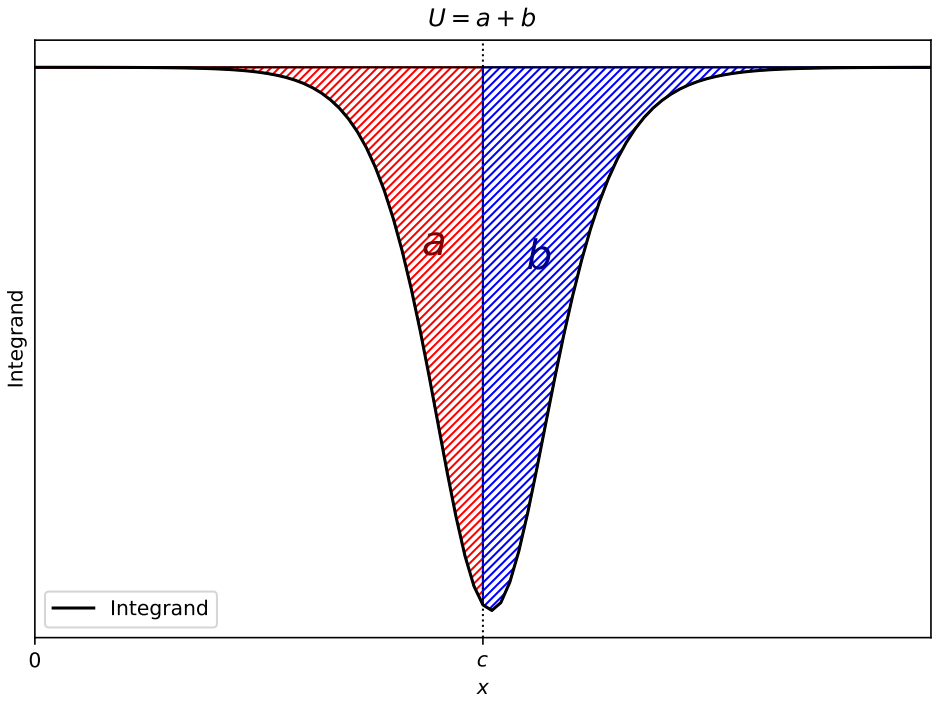

Figure 24: Same as Figs. 20–23, but for the U integral.

8.3.5 Fermi U integral (H^{11})

Define

$$U_k(\eta,\mu) := H_k^{11}(\eta,\mu) = -\int_0^\infty x^k dk \frac{\mu}{E}\frac{e^{E-\eta}}{(e^{E-\eta}+1)^2} = -\int_0^\infty \frac{\mu}{E}\frac{x^k dk}{4\cosh^2\left[(E-\eta)/2\right]} \tag{233}$$

In this case, the entire integrand is small with a dip around $x = c$, and the integral can be evaluated directly, splitting at c (Fig. 24). A special result is:

$$\hat{U}_k(\eta,\mu) = \frac{\partial}{\partial\mu}\hat{F}_k(\eta,\mu) = c^k\frac{\partial c}{\partial\mu} = -\mu c^{k-1}. \tag{234}$$

No algorithm in the EoS solver uses the U integral.

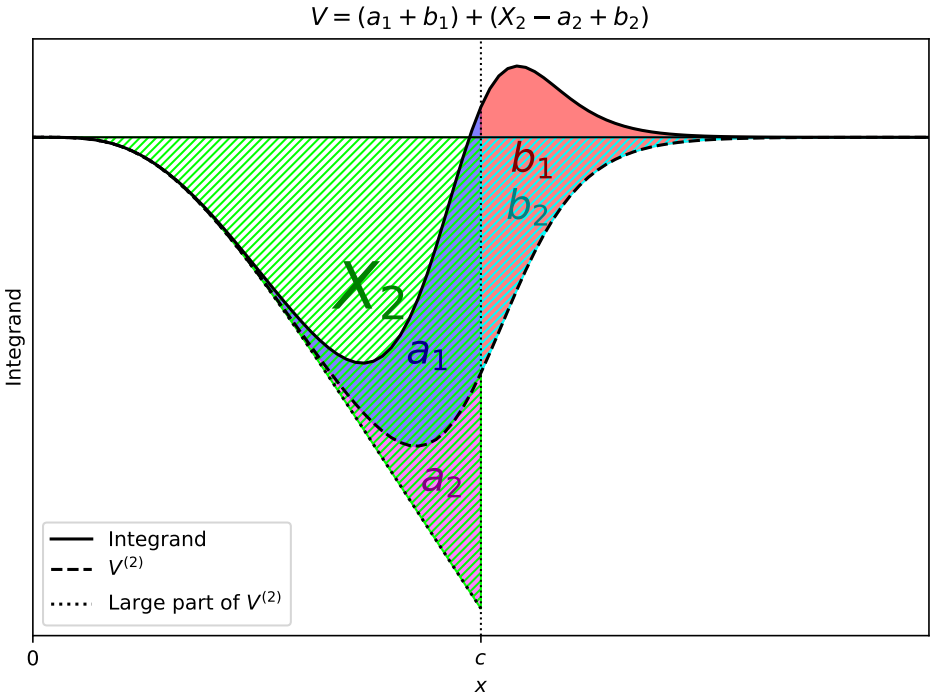

Figure 25: Same as Figs. 20–24, but for the V integral. $V^{(1)}$ and $V^{(2)}$ represent the two terms of the integrand in the form presented in Eq. (235).

8.3.6 Fermi V integral (H^{02})

The V integral is the most complicated of all the Fermi integrals up to order 2:

$$V_k(\eta,\mu) := H_k^{02}(\eta,\mu) = \int_0^\infty \frac{x^k}{E^2}\left[\frac{\mu^2}{4\cosh^2(E-\eta)} - \frac{x^2}{E}\frac{1}{e^{E-\eta}+1}\right]dx. \tag{235}$$

The first term of the integrand is entirely small and can be evaluated directly. The second term can be split in a similar manner as F (Fig. 25):

$$\begin{aligned}
-\int_0^\infty \frac{x^{k+2}}{E^3}\frac{dx}{e^{E-\eta}+1} &= -\int_0^\infty \frac{x^{k+2}}{2E^3}\left(1-\tanh\frac{E-\eta}{2}\right)dx \\
&= -\int_0^c \frac{x^{k+2}}{E^3}dx - \int_0^c \frac{x^{k+2}}{2E^3}\left(-1-\tanh\frac{E-\eta}{2}\right)dx \\
&\quad -\int_c^\infty \frac{x^{k+2}}{E^3}\frac{dx}{e^{E-\eta}+1} \\
&= -\int_0^c \frac{x^{k+2}}{E^3}dx + \int_0^c \frac{x^{k+2}}{E^3}\frac{dx}{e^{\eta-E}+1} - \int_c^\infty \frac{x^{k+2}}{E^3}\frac{dx}{e^{E-\eta}+1}.
\end{aligned} \tag{236}$$

The zero-temperature form of the V integral requires an application of the Leibniz integral rule:

$$\begin{aligned}\hat{V}_k(\eta,\mu) = \frac{\partial}{\partial\mu}\hat{G}_k(\eta,\mu) &= -\int_0^c x^k\left(\frac{1}{E}-\frac{\mu^2}{E^3}\right)dx - c^k\frac{\partial c}{\partial\mu}\frac{\mu}{\sqrt{c^2+\mu^2}} \\ &= \int_0^c x^k\frac{\mu^2-E^2}{E^3}dx + \frac{\mu^2 c^{k-1}}{\eta} = -\int_0^c \frac{x^{k+2}}{E^3}dx + \frac{\mu^2 c^{k-1}}{\eta}.\end{aligned} \tag{237}$$

The large part of the integral can be evaluated with hypergeometric functions (assuming $\mu \neq 0$), but it is even more complicated than those of H and G:

$$\begin{aligned}\int_0^c \frac{x^{k+2}}{E^3}dx = \frac{c^{k+3}}{(k+3)\eta^2|\mu|^3}\Bigg\{&(k+4)\mu^2\,{}_2F_1\left(-\frac{1}{2},\frac{k+3}{2};\frac{k+5}{2};-\frac{c^2}{\mu^2}\right) \\ &+ [(k+2)\eta^2+\mu^2]{}_2F_1\left(\frac{1}{2},\frac{k+3}{2};\frac{k+5}{2};-\frac{c^2}{\mu^2}\right)\Bigg\}.\end{aligned} \tag{238}$$

If $\mu = 0$, then V diverges if $k < 1$.

If $m = 0$, then the second term of Eq. (228) is indeterminate. Applying l'Hôpital's rule to this term gives:

$$\epsilon = -\frac{dT^4}{2\pi^2}\left[V_4\left(\frac{\mu}{T},0\right) + V_4\left(-\frac{\mu}{T},0\right)\right]. \tag{239}$$

Likewise,

$$\begin{aligned}s = \frac{d}{2\pi^2}\Big\{&T^3\left[H_2\left(\frac{\mu}{T},0\right) + H_2\left(-\frac{\mu}{T},0\right)\right] - \mu T^2\left[F_2\left(\frac{\mu}{T},0\right) - F_2\left(-\frac{\mu}{T},0\right)\right] \\ &+ T^4\left[V_4\left(\frac{\mu}{T},0\right) + V_4\left(-\frac{\mu}{T},0\right)\right]\Big\}.\end{aligned} \tag{240}$$

8.4 Solving for ν_i given n_i

For any T, the density of a Fermi gas is monotonic in ν, and this monotony is strict unless $T = 0$ and $\nu \leq |m^*|$. At $T = 0$, it is easy to show that

$$\nu = \mathrm{sgn}(n)\sqrt{m^{*2} + \left(\frac{6\pi^2 n}{d}\right)^{2/3}}. \tag{241}$$

At finite temperature, this is the default initial guess for our root-solver if n is sufficiently large. However, for $\nu \ll \mu$, we get the asymptotic result:

$$\begin{aligned} n &\approx \frac{d}{2\pi^2}\int_0^\infty k^2 dk \left[e^{(\nu - E_k^*)/T} - e^{(-\nu - E_k^*)/T}\right] = \frac{d}{\pi^2}\sinh\frac{\nu}{T}\int_0^\infty k^2 dk\, e^{-E_k^*/T} \\ &= \frac{dT}{\pi^2}\sinh\frac{\nu}{T} K_2\left(\frac{m^*}{T}\right) \sim \frac{dT}{\pi^2}\left(\frac{m^* T}{\pi}\right)^{3/2} e^{-m^*/T}\sinh\frac{\nu}{T} = C\sinh\frac{\nu}{T}, \end{aligned} \tag{242}$$

which means that we may use the initial guess

$$\nu \approx T\,\mathrm{arcsinh}\,\frac{n}{C} \tag{243}$$

if it is smaller in magnitude than Eq. (241). Since $\partial n/\partial\nu$ can be evaluated analytically (it is $P^{20}(T, \nu, m^*)$), we can use Newton's method to solve for ν, falling back to Brent's method on a suitable interval if convergence fails. For multiple fermions, each ν_i can be evalauted separately.

8.5 RMF without hyperons

The RMF without hyperons is solved within `dd2.py`. At fixed meson fields, m_i^* and g_{mi} can be calculated immediately for each nucleon, from which we can also obtain ν_i and n_i^s. The meson fields can be solved by enforcing self-consistency with the EoMs (Eqs. (112)–(114) with ϕ similar to Eq. (113)); our initial guess for the meson fields are those for the nearest evaluated point in (T^3, n_p, n_n)-space (including points calculated while solving HS), or zero if no points have been evaluated.

8.6 RMF with hyperons

For the chemical equilibration of the hyperonic RMF, it is convenient to work in the $(\mu_B, \mu_\mathcal{S}, \mu_Q, \mu_L)$ basis, as they are the independent conserved charges under the strong interaction. Upon expanding the chemical potential for each species via Eq. (136), this yields a relation for μ_B and μ_Q to the

nucleon effective chemical potentials:

$$\mu_B = \mu_n = \nu_n + \Sigma_n^v \tag{244}$$

$$\mu_Q = \mu_p - \mu_n = (\nu_p - \nu_n) + (\Sigma_p^v - \Sigma_n^v) \tag{245}$$

The Σ^v-containing part of the μ_Q formula contains two Σ^r terms that cancel out, so Σ^r does not need to be computed in advance. Thus, we can define:

$$\xi_i = \nu_i + \Sigma^r + (\tau_{3i} - \beta)\Sigma^t = \mu_i - g_{\omega i}\omega - g_{\phi i}\phi - g_{\rho i}\tau_{3i}\rho. \tag{246}$$

Then if we define $\xi_B = \xi_n$, the analogous definition of $\xi_Q = \xi_p - \xi_n = \mu_Q$, and we may reformulate the chemical equilibrium condition as:

$$\xi_i = \xi_B + Q_i \xi_Q. \tag{247}$$

Then at fixed n_B, Y_q, and meson fields, we can solve for the isospin-fraction β and Σ^t via self-consistency:

1. Calculate g_{mi}, their derivatives, and m_i^*.
2. Initialize ν_i that produces nucleonic matter with the correct n_B and Y_q.
3. Solve for ν_p and ν_n such that the correct values of n_B and Y_q are recovered under chemical equilibrium with the hyperons (which includes calculating $\Sigma_i^v - \Sigma^r$ in ξ_i).
4. Recover the equilibrated mixture from the found ν_p and ν_n, including β and Σ^t that are to be matched to input.

Then the meson fields can be solved by consistency with the EoMs, as for the nucleonic RMF.

8.7 Single-nucleus partition function

The module `gaz.cpp` includes the natural logarithms of the g_{AZ} integral (Eq. (173)) and its temperature derivative,[12]

$$\frac{\partial g_{AZ}}{\partial T} = \frac{c_1}{T^2 A^{5/3}} \int_0^{B_{AZ}} E e^{-E/T+\sqrt{2aE}} dE. \tag{248}$$

We handle these quantities as logarithms for two reasons. They can be extremely large — for the hyperheavy nucleus $^{339}126$, $g \approx 1.053 \times 10^{157}$ at the maximal $T = 50$ MeV, while $g^0 = 14$. Also, n_{AZ} as calculated in Eq. (177) is extremely sensitive to $\mu^0_{p,n}$ at low T, so it is itself handled as a logarithm, and g_{AZ} occurs only outside the exponential. The integrals are also converted by substitution of $x = \sqrt{E/T}$ to the form:

$$g_{AZ} = g^0_{AZ} + \frac{2c_1 T}{A^{5/3}} \int_0^{\sqrt{B_{AZ}/T}} x e^{x(\sqrt{2aT}-x)} dx \tag{249}$$

$$\frac{\partial g_{AZ}}{\partial T} = \frac{2c_1}{A^{5/3}} \int_0^{\sqrt{B_{AZ}/T}} x^3 e^{x(\sqrt{2aT}-x)} dx. \tag{250}$$

This form has a dimensionless integral, and it avoids catastrophic cancellation for $\partial g_{AZ}/\partial T$ at low temperature. It is also readily apparent that at $T = 0$, $g_{AZ} - g^0_{AZ}$ vanishes as $O(T)$, and

$$\frac{\partial g_{AZ}}{\partial T} = \frac{2c_1}{A^{5/3}} \int_0^{\infty} x^3 e^{-x^2} dx = \frac{c_1}{A^{5/3}}. \tag{251}$$

Additionally, to prevent numerical overflow or underflow, we may move a factor of e^p out of the integrands, where p is chosen as the maximum value of the exponent over the domain of integration.

Due to their frequent usage in the HS solver, there is also an implementation of $\ln(e^x + e^y)$ that

[12] For a dimensional quantity Q, $\ln Q$ is understood to be that of its numerical value in arbitrary units. In the underlying formulas, the arguments of logarithms are always dimensionless.

is equivalent to NumPy's `logaddexp`, and of the two functions

$$\texttt{logsumexp}(\mathbf{x}) = \ln\left(\sum_i e^{x_i}\right), \tag{252}$$

$$\texttt{logsumexp}(\mathbf{x}, \mathbf{b}) = \ln\left(\sum_i b_i e^{x_i}\right) \tag{253}$$

that are equivalent to, but faster than, SciPy's function in module `special` with the same name.

8.8 Solution of the HS model

8.8.1 Solving with nuclei

At fixed meson fields, the method `bootub` takes an input value of ν_i^0. It then takes $m_i^{*\prime}$ (outside the nuclei) and computes n_i' and g_{mi}, and solves for self-consistency of $m_i^{*\prime}$ with Eq. (134). From there, we can calculate n_i' and use Eqs. (136) and (175)–177 to calculate n_{AZ}.

Then we compute n_i using Eqs. (161) and (162); we will denote these calculated values as $n_i^1(\nu_i^0)$. We first use Powell's method to locate the unique ν_i^0 such that n_i^1 matches the actual values of the n_i; we do this by minimizing the function

$$f(\nu_i^0) = \sum_{i\in\{p,n\}} \ln^2\left[\frac{n_i^1(\nu_i^0)}{n_i}\right]. \tag{254}$$

This objective function can sometimes have a narrow valley around the root (Fig. 26b). At low temperatures, the Powell method might terminate before reaching the minimum, but it will nonetheless land somewhere in the valley if the HS model is solvable for the given f_m.[13] We accept the reported solution if $f(\nu_i^0) < 10^{-16}$, which corresponds to a maximum relative error in n_B of $\sim 10^{-8}$. If Powell's method does not give the desired tolerance, we use a backup method using two layers of Brent's method:

1. For fixed ν_p^0, solve for ν_n^0 such that $n_B^1(\nu_i^0) = n_B$.

[13] Because the HS model does not include anti-nuclei, it may fail at $T > 50$ MeV. Meson-field values very far from the physical point can also break the model.

2. Solve for $n_n^1(\nu_i^0) = n_n$ along the contour defined by the previous item.

This method will always converge efficiently if DD2 is solvable because n_p^1 and n_n^1 are both convex in ν_i^0.

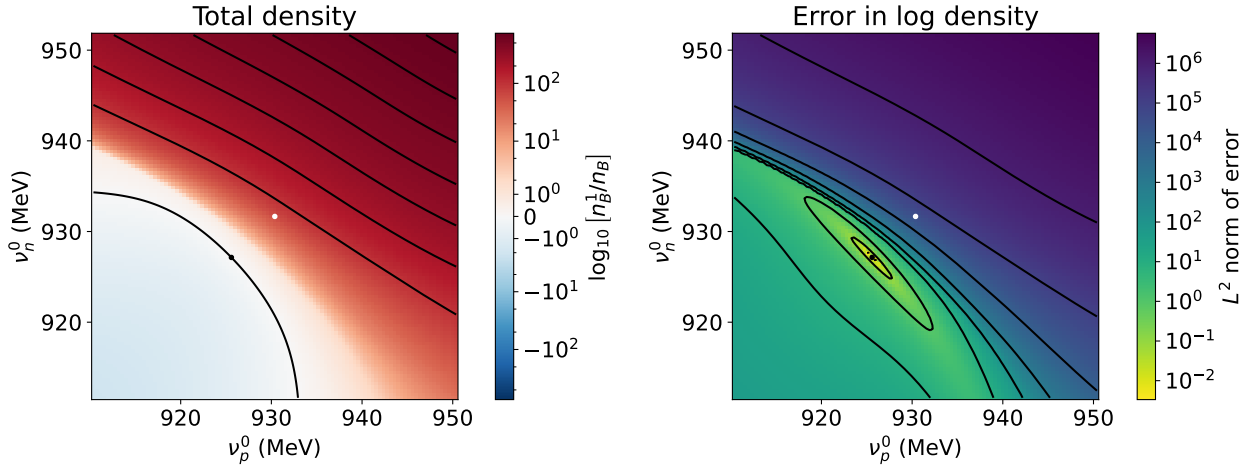

(a) (b)

Figure 26: (a) Total density of bound nucleons in HS(DD2) at $T = 10^{0.60} \approx 3.981$ MeV and all meson fields equal to zero, as computed by Eq. (177). The white dot represents the solution to the RMF at $n_B = 10^{-3}$ fm^{-3} ($\kappa = 0.9933$) and $Y_q = 0.5$ with no meson fields, while the black dot is the actual solution at these conditions. (b) The ℓ^2 residual error in $\ln(n_i)$ for both nucleons, as calculated in Eq. (254). The presence of a valley around the solution is evident.

8.8.2 Meson fields

In the HS model, the meson fields live only in the space not occupied by nuclei; the meson fields within the nuclei are effectively confined to the nuclei and their contribution to the EoS is accounted for through the nuclear binding energy.

For fixed f_m outside the nuclei, we can solve the HS model to obtain the nucleon density n_i' within this region. It is possible to derive the EoMs such that $(\partial f/\partial f_m)_{n_i} = 0$, but because their internal fields are already accounted for by the mass table, we can take the approximation that the clusters do not affect the external meson fields, and thus are ignored except for their volume exclusion [45]. Then we can solve for the f_m such that this agrees with the EoMs, but with n_i' and $n_i^{s\prime}$ (defined analogously to n_i') in place of the RMF densities.

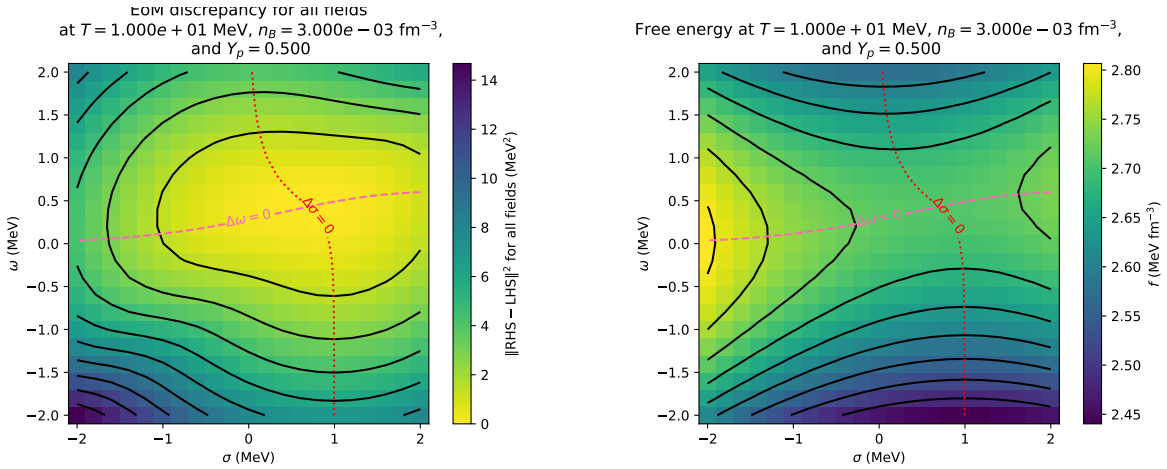

(a) (b)

Figure 27: Discrepancy in HS(DD2) between the meson fields and their expected values from the cluster-ignorant EoM (a), and free energy (b) at $T = 10$ MeV, $n_B = 3 \times 10^{-3}$ fm^{-3}, and $Y_q = 0.5$ over the σ–ω plane, with ρ's EoM already solved.

At higher densities and low T, there are sometimes two stable equilibria. The physical significance of this is that the phase closer to RMF equilibrium is an approximation to the Maxwell transition; in order to construct the Maxwell transition properly, we need to choose an initial guess for the root solver so that it always converges to the cluster-rich equilibrium (Fig. 28).

8.9 Maxwell transition

HS is only necessary up to the phase transition to RMF, where P and μ (including electrons) are equal; after this, the Maxwell construction can be applied to connect the two phases. For this reason, the series at fixed T and Y_q must be solved sequentially in increasing order of n_B. At such conditions, $P(\mu)$ is a monotonically increasing function for both HS and RMF by Theorem 3, and

$$\left(\frac{\partial P}{\partial \mu}\right)_T = \left(\frac{\partial P}{\partial n}\right)_T \left(\frac{\partial n}{\partial \mu}\right)_T = n. \tag{255}$$

Therefore, $P(\mu)$ can be interpolated with a cubic spline with the boundary condition that $\partial P/\partial \mu = n_B$ at the endpoints. The Maxwell transition is approximately equal to the point where the splines intersect, and n_B at each endpoint can be found by taking $\partial P/\partial \mu$. The error of the approximation

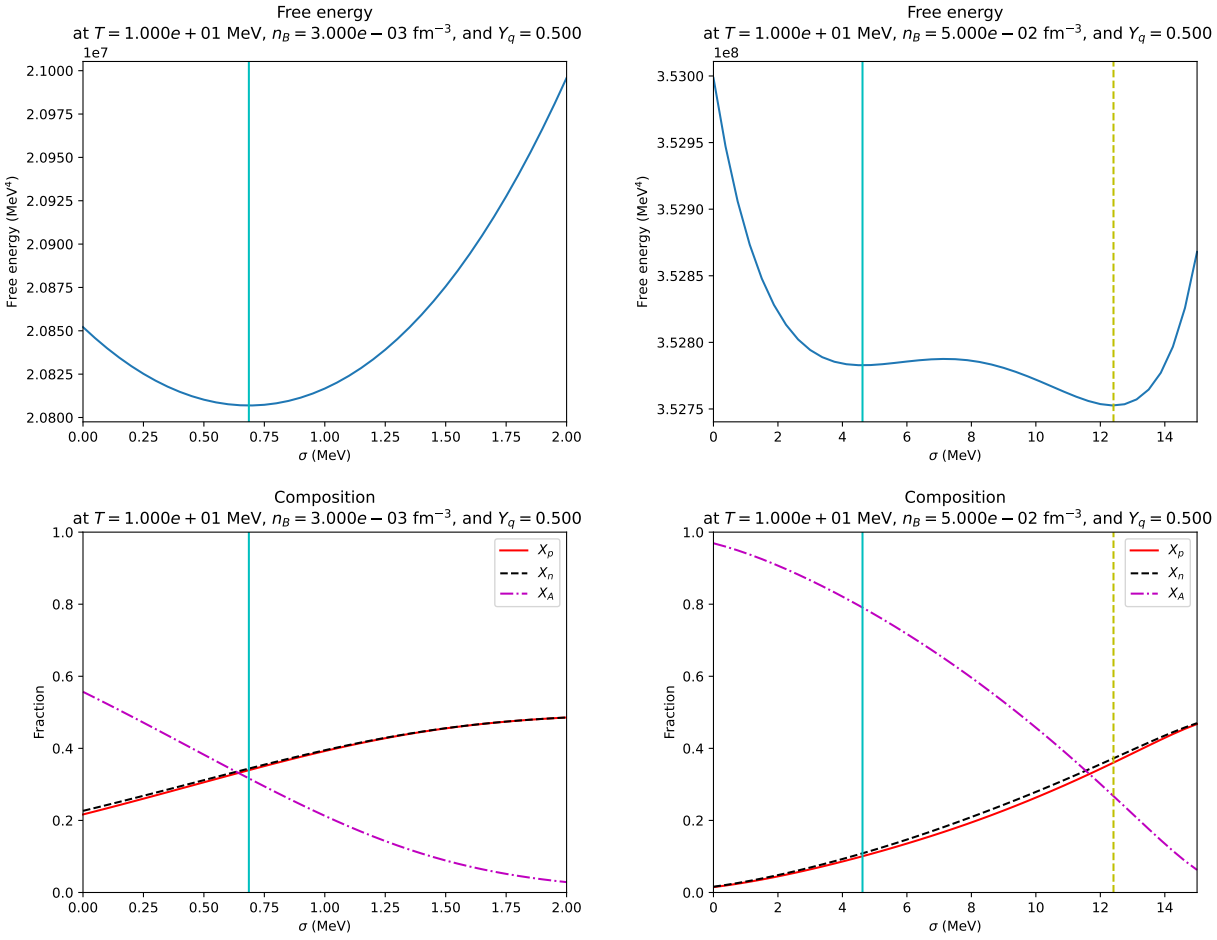

(a) (b)

Figure 28: Free energy and composition of HS(DD2) as functions of σ, with all other meson-field EoMs solved, at $T = 10$ MeV, $Y_q = 0.5$, and (a) $n_B = 3 \times 10^{-3}$ fm^{-3} and (b) 5×10^{-2} fm^{-3}.

is on the order of $(\partial^4 P/\partial\mu^4)\Delta n_B^4$, where Δn_B is the difference between two consecutive datapoints [166]. The exact transition endpoints can be found by iterating a root-solver from this intersection to get equality of P and μ between the two phases.

9 Fitting

We took all the hyperon couplings to be in fixed ratios to the nucleon couplings, and $g_{mN}(\beta = -1)/g_{mN}(\beta = 0)$ was a fixed ratio as well; as Eq. (119) is set up, this can be done by adjusting $g_{mN}^{S,N(0)}$ only. Additionally, in order to qualitatively reproduce the coupling curves in Ref. [152] and

the c_s^2 curve in Ref. [17], and to get a reasonably smooth EoS as judged by the profile of c_s^2, we set the transition zones to a center $c_{\omega,\phi,\rho} = 3.5$ and width $d = 1.8$ (in units of n_0) for the vector mesons, while no flattening was done for the σ ($c_\sigma = \infty$). With these constraints, there are 17 free parameters:

- The parameters $g_{\sigma N}^{S,N(0)}$ and a_σ for the σ coupling to nucleons.
- The parameters $g_{\sigma Y}^{S(0)}$ for $Y \in \{\Lambda, \Sigma, \Xi\}$, with $g_{\sigma Y}^{N(0)}$ in the same proportion to these parameters as their nucleon counterparts (and likewise for the other mesons). For convenience of fitting, we varied these constants directly, not as ratios to $g_{\sigma N}^0$.
- The "effective $g_{\omega N}^{S,N(0)}$" [153] due to the combined effects of the ω and ϕ in nucleonic matter,

$$\tilde{g}_{\omega N}^{S,N(0)} := g_{\omega N}^{S,N(0)} \sqrt{1 + \left(\frac{g_{\phi N}^{S,N(0)}/m_\phi}{g_{\omega N}^{S,N(0)}/m_\omega} \right)^2}. \tag{256}$$

- The $\mathrm{SU}(3)_f$ parameter z for vectors, with $\alpha = 1$.
- a_ω and b_ω.
- The parameters $g_{\rho N}^{S,N(0)}$, a_ρ, and b_ρ for the ρ coupling to nucleons.
- The parameters $g_{\rho Y}^{S(0)}$ for $Y \in \{\Sigma, \Xi\}$. ($g_{\rho\Lambda}$ is always zero, since the Λ has isospin 0.)

For convenience and lack of strong constraint, we surveyed five values of $b_\omega = \{0.60, 0.65, 0.70, 0.75, 0.80\}$ in order to pick the one that was most consistent with NS constrains on Λ, with $b_\omega = 0.80$ ultimately chosen. We also set $b_\rho = 0.40$ a priori because a low b_ρ tends to delay the onset of hyperons. For the process on Λs mentioned above, this critical density is only slightly larger than the density of Λ appearance in NS matter. Therefore, an accurate determination of hyperon critical densities is essential for a consistent description of the NS cooling. The model, which we dubbed "DID" (for "density- and isospin-dependent"), and also as "DIDY" where hyperons are included, was fitted using Bayesian analysis, which assigns the posterior probability distribution of N-dimensional

model parameters θ for a hypothesis H, given a prior distribution $\pi(\theta)$ and evidence E, as [167]:

$$P(\theta|E) = \frac{\Lambda(\theta)\pi(\theta)}{Z}, \tag{257}$$

where $\Lambda(\theta) = \Pr(E|\theta)$ is the likelihood of the evidence given a value of θ, $\pi(\theta)$ is the prior, and

$$Z = \Pr(E|H) = \int \Lambda(\theta)\pi(\theta)d^N\theta \tag{258}$$

is the Bayesian evidence. We used the `PyMultiNest` package [168], which uses a "nested sampling" procedure that continually refines an estimate of Z, with 2000 live points and a uniform prior distribution. Eighteen pieces of evidence were used, and its likelihood was modeled as independent, normally distributed variables; that is, least-squares minimization of the z-scores for the computed observables. At the end of the procedure, a sample from the posterior was obtained. The best likelihood model, the MLE, was then found using a minimizer beginning at the greatest-likelihood samples. We found that the Nelder–Mead algorithm provides stable, albeit slow, convergence, in a space where some parameter values can be excluded as unphysical by heuristics. The results are listed in Table 6.

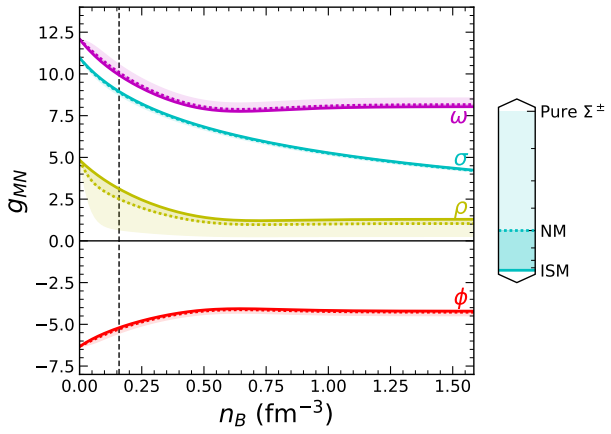

Figure 29: Plot of the meson–nucleon couplings as functions of density for DID, including the range of values as functions of isospin fraction. For the isospin-0 mesons, the solid lines are for symmetric matter ($\beta = 0$), the dashed lines are for pure neutron or proton matter ($\beta = \pm 1$), and the unmarked edge of the shaded regions are the theoretical limits of $\beta = \pm 2$ for the baryon octet.

Table 6: List of parameters of DID and their values, as well as the bounds used in the Bayesian analysis.

Parameter	Range		MLE	68% C.L.
$g_{\sigma N}^{S(0)}$	6.00	11.00	8.94873669	$8.263^{+0.713}_{-0.735}$
$g_{\sigma N}^{N(0)}$	6.00	11.00	8.89241948	$8.094^{+0.695}_{-0.706}$
a_σ	0.00	1.00	0.16394393	$0.189^{+0.041}_{-0.032}$
$g_{\sigma\Lambda}^{S(0)}$	5.00	11.00	7.51077621	$6.203^{+0.887}_{-0.741}$
$g_{\sigma\Sigma}^{S(0)}$	3.00	9.00	6.26418057	$4.770^{+0.999}_{-0.809}$
$g_{\sigma\Xi}^{S(0)}$	1.00	7.00	6.53781517	$4.616^{+1.309}_{-1.373}$
$\tilde{g}_{\omega N}^{0}$	7.00	14.00	10.82857726	$9.703^{+1.165}_{-1.255}$
$\tilde{g}_{\omega N}^{1}$	7.00	14.00	11.00228164	$9.698^{+1.087}_{-1.133}$
a_ω	0.00	1.00	0.15313180	$0.172^{+0.048}_{-0.032}$
b_ω	—		0.80000000	0.800
z	0.00	$2/\sqrt{6}$	0.07720445	$0.194^{+0.135}_{-0.121}$
$g_{\rho N}^{S(0)}$	0.00	6.00	3.23020263	$3.563^{+0.400}_{-0.320}$
$g_{\rho N}^{N(0)}$	0.00	6.00	2.59340047	$2.663^{+0.644}_{-0.541}$
a_ρ	0.00	4.00	0.39223762	$0.212^{+0.149}_{-0.130}$
b_ρ	—		0.40000000	0.400
$g_{\rho\Sigma}^{S(0)}$	0.00	6.00	0.00545444	$0.787^{+0.819}_{-0.553}$
$g_{\rho\Xi}^{S(0)}$	0.00	6.00	1.11415631	$2.096^{+0.820}_{-0.729}$

For any choice of parameters, saturation density n_0 was calibrated so that $P(n_0) = 0$ in symmetric matter without leptons at $T = 0$. Some EoS candidates were discarded because this could not be done; specifically, we ruled out EoS's if we could determine that $n_0 < 0.01$ fm^{-3} or $n_0 > 0.30$ fm^{-3}, under presumption that these are extremely implausible or do not have an n_0. We used the experimental measurement $n_0 = 0.150 \pm 0.010$ fm^{-3} from Ref. [88], which was estimated from a radius measurement of ^{208}Pb with parity-violating electron scattering.

Another exclusion constraint was that since the DD couplings in DD-RMFs are not Lorentz-invariant [159], we needed to constrain $0 < c_s^2 < 1$ at two keypoints. We chose to evaluate this for symmetric and neutron matter for $c_\omega n_0$, which correspond to a peak in the graph of c_s^2 against n_B.

9.1 Hyperon potentials

For symmetric matter, the only significant difference between DD2Y and our model is because the $g_{\sigma Y}^0$'s are normalized to different values for the U_Y's [145], specifically the empirical estimates

from Ref. [118]: −30 MeV for Λ, +30 MeV for Σ, and −18 MeV for Ξ. The latter two are highly uncertain experimentally due to limited data and widely varying estimates from models based on those data [118, 2], which is why we used the LQCD-based results from Ref. [2] in our fitting. For easier comparison, we also made an extension of DDB [147], called DDBY, which includes $SU(6)_{sf}$ symmetry for vectors and σ couplings fitted to the HALQCD potentials (Table 7). This EoS has saturation density $n_0 = 0.143862$ fm^{-3}.

Table 7: The σ couplings in DDBY.

Iso-multiplet	$g_{\sigma i}$
N	8.983000
Λ	5.699184
Σ	4.339637
Ξ	2.732038

All the hyperon-related parameters are dependent on the U_Y's at $|\mathbf{k}| = 0$ in symmetric and neutron matter from HALQCD [2], which were calculated in a BHF model with baryon–baryon correlation parameters from LQCD. The LQCD calculations were done at near-physical quark masses (with $m_\pi = 146$ MeV and $m_K = 525$ MeV). There are nine datapoints in this evidence: three for the iso-multiplets in symmetric matter, six for the hyperons in neutron matter. All the statistical uncertainties in this data are about ±2 MeV. Table 8 lists these datapoints, as well as the values obtained in our model.

Table 8: Hyperon potentials in symmetric and neutron matter at $n_B = n_0$ vs. results from [2]. Blank cells in the ISM columns are the same across each iso-multiplet.

Quantity	HALQCD		Value @ MLE		68% C.L.	
	ISM	NM	ISM	NM	ISM	NM
Λ	−28.15±2.02	−25.42±1.78	−27.87	−25.54	$-28.39^{+1.75}_{-1.69}$	$-25.17^{+1.52}_{-1.60}$
Σ^+	+14.62±1.82	+8.24±3.68	+14.99	+6.85	$+15.04^{+1.68}_{-1.70}$	$+6.48^{+2.51}_{-2.51}$
Σ^0		+15.73±1.70		+15.79		$+15.67^{+1.24}_{-1.22}$
Σ^-		+24.86±1.39		+24.74		$+24.86^{+1.35}_{-1.33}$
Ξ^0	−3.60±2.14	−12.19±1.46	−3.97	−12.13	$-3.46^{+1.68}_{-1.71}$	$-12.22^{+1.45}_{-1.40}$
Ξ^-		+5.79±2.59		+5.85		$+5.73^{+2.30}_{-2.35}$

9.2 Bulk nuclear properties

We also took six quantities regarding low-density symmetric matter, and two on neutron matter, tabulated in Table 9. The first is the binding energy per nucleon of saturated symmetric matter, $B = -15.6 \pm 0.6$ MeV [169]. We use the incompressibility from GMR of ^{208}Pb and ^{90}Zr, 240 ± 20 MeV [105]. Next is the quadratic symmetry energy at saturation $S_2 = 32.0 \pm 1.1$ MeV from Ref. [16] (fitted to various nuclear data). While $K_{\rm sym}$, Q, S_4, and higher-order derivatives of binding energy are poorly constrained [16], another well-constrained number is

$$\begin{aligned} M :=& 3n_B \frac{\partial}{\partial n_B} \left(9n^2 \frac{\partial^2 B}{\partial n^2} + 18 \frac{P}{n} \right) \\ =& x \left(18 \frac{\partial B}{\partial y} + 12Kx + Qx^2 \right) \end{aligned} \tag{259}$$

at the mean nuclear density of 0.11 fm^{-3} $\approx 0.7\ n_0$, which is attained in the bulk of an atomic nucleus. EoSs fitted to finite nuclei agree most strongly at this point [170]. Additionally, while neutron matter is not well-constrained experimentally, it is easier than symmetric matter to compute with ChEFT: Ref. [15] used an N^{3}LO + 3N formulation to return estimates of the pressure of neutron matter (related to L) over the density range from 0.05–0.34 fm^{-3} $\approx$ 0.3–2.2 n_0. From this dataset, we singled out two keypoints to ensure that low-density matter is well-behaved: $n_B \in \{0.08, 0.16\}$ fm^{-3} $\approx \{0.5, 1.1\}\ n_0$.

Lastly, to control the behavior of dense matter, we used the pressure data series from Ref. [17] on symmetric matter (not including electrons). They used Bayesian analysis from HIC data on a crude EoS model with three inputs: K below 2 n_0 (with $n_0 = 0.16$ fm^{-3}), plus two regions with constant c_s^2 over $[2, 3]\ n_0$ and $[3, 4]\ n_0$; c_s^2 was fixed at the near-conformal value of 0.3 above this threshold. The points at $n_B \in \{2, 3.5\}\ n_0 = \{0.32, 0.56\}$ fm^{-3} were chosen as keypoints —while this model likely overestimates [171], the confidence band of $P_{\rm SM}$ is more consistent with DD2 and DDB than they are with that from Ref. [18].

DID is not fitted to finite nuclei, and we made no attempt to check how accurately they describe their measured masses and shapes. We recommend using the approach of Ref. [150] with triaxial

Table 9: List of datapoints, other than hyperon potentials, used as evidence in the Bayesian analysis.

Quantity	Units	Empirical	Ref.	Value @ MLE	68% C.L.
n_0	fm^{-3}	0.150±0.010	[88]	0.15880045	$0.153^{+0.006}_{-0.006}$
B	MeV	−15.6±0.6	[169]	−15.40	$-15.42^{+0.58}_{-0.57}$
K	MeV	240±20	[169]	227.06	$212.0^{+15.0}_{-9.04}$
$M(0.11\ \mathrm{fm}^{-3})$	MeV	1100±70	[170]	1122.72	$1132.^{+60}_{-62}$
S_2	MeV	32.0±1.1	[16]	32.44	$32.43^{+1.06}_{-1.03}$
$P_{\mathrm{NM}}(0.08\ \mathrm{fm}^{-3})$	$\mathrm{MeV\ fm}^{-3}$	0.472±0.036	[15]	0.4569	$0.441^{+0.032}_{-0.034}$
$P_{\mathrm{NM}}(0.16\ \mathrm{fm}^{-3})$	$\mathrm{MeV\ fm}^{-3}$	2.898±0.404	[15]	3.233	$3.243^{+0.238}_{-0.232}$
$P_{\mathrm{ISM}}(0.32\ \mathrm{fm}^{-3})$	$\mathrm{MeV\ fm}^{-3}$	19.0±14.3	[17]	12.11	$12.36^{+0.86}_{-0.78}$
$P_{\mathrm{ISM}}(0.56\ \mathrm{fm}^{-3})$	$\mathrm{MeV\ fm}^{-3}$	106.8±22.0	[17]	109.0	$109.2^{+10.9}_{-10.7}$

nuclear shapes; the PDG mass values for the ω, ϕ, and ρ^0 mesons; and the Skyrme-potential depth V_0 or the pion Yukawa potential as an additional free parameter for nuclear pairing. The mass of the σ meson would also need to be recalibrated because it is poorly constrained experimentally, with a Particle Data Group-quoted uncertainty of 200 MeV [1].

10 Results

We computed the EoS table of DIDY with electrons for 1487160 grid points covering the full range of hadronic matter in the QCD phase diagram:

- 81 temperature values logarithmically spaced with 25 points per decade, from 0.1 MeV to $10^{2.20} \approx 158.5$ MeV.
- 306 density values logarithmically spaced with 25 points per decade, from 10^{-12} fm^{-3} to $10^{0.20} \approx 1.585$ fm^{-3}.
- 60 Y_q values linearly spaced from 0.01 to 0.60.

For DD2Y and DDBY, we also computed the above n_B and Y_q datapoints, but only for $T = 0.1$ MeV (18360 grid points). When computing β-equilibrium via $\mu_L = 0$, we fixed $T = 0.1$ MeV, used cubic interpolation, and capped $0.01 \leq Y_q \leq 0.60$; the upper bound was never violated, but the lower one has an effect at high densities with abundant hyperons. For this reason, we also computed β-equilibrium directly within the pure RMF models, usually at eight times the logarithmic resolution

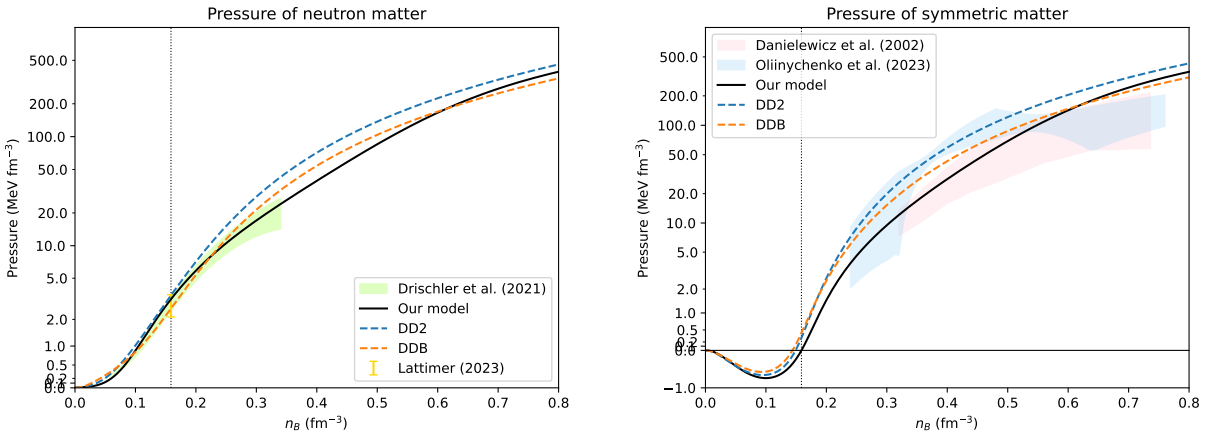

(a) $Y_q = 0$ (b) $Y_q = 0.5$

Figure 30: Pressure of DID vs. DD2 and DDB in (a) neutron matter vs. the ChEFT model in Ref. [15] and L predicted by [16]; and (b) symmetric matter, excluding leptons, against Refs. [17] (sky-blue) and [18] (pink). All plots are at $T = 0$.

in n_B in order to analyze c_s^2 better.

10.1 Bulk properties of cold matter

10.1.1 Pressure and energy density

The pressure of DID in neutron matter and symmetric matter, excluding leptons, is shown in Fig. 30. All three models have similar behavior below saturation density n_0, where all models provide an adequate description of the ChEFT constraint [15] for neutron matter, with DD2 following the upper edge of the uncertainty band. For $n_B > n_0$, DD2 predicts a larger pressure than DID or DDB in both ISM and NM. For $n_B \gtrsim 2n_0$, DD2 significantly exceeds the ChEFT constraint, predicting the stiffest EoS. Out of the three models, DID is the softest, while DDB demonstrates intermediate stiffness, remaining closer to the ChEFT band than DD2. The isospin-density dependence in DID produces a moderately softer NM EoS compared to DDB in the range $n_B \simeq (1.5\text{–}3.5)\, n_0$, but afterward it overtakes it.

In symmetric matter at low densities $n_B \lesssim 0.1$ fm^{-3}, all models exhibit negative pressure corresponding to the nuclear liquid-gas phase transition, with zero pressure at their respective

saturation densities. For $n_B \gtrsim n_0$, the pressure has the same ordering as in neutron matter, with DD2Y being the stiffest and DIDY the softest until it overtakes DDB near 0.60 fm^{-3}. Compared to HIC constraints from Refs. [18, 17] at $n_B \simeq (2\text{–}5)\, n_0$, corresponding to $n_B \simeq (0.3\text{–}0.8)$ fm^{-3}, DID is in good agreement with Ref. [18] throughout the range. Therefore, the isospin dependence of the couplings introduced to accommodate HALQCD-based hyperon potentials in neutron-rich matter does not compromise the description of symmetric-matter properties constrained by terrestrial experiments, validating the isospin-density-dependent coupling framework across the full range of isospin asymmetries.

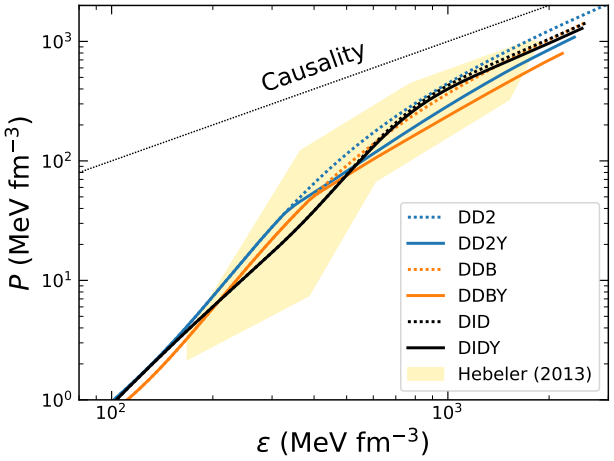

Figure 31: Pressure of DDB and DID, as well as their respective EoSs with hyperons, against energy density, in β-equilibrium with electrons but not nuclei, against the constraint from Ref. [19] assuming causality and $M_{\rm max} > 1.97\ M_\odot$ (yellow). The dotted diagonal line is the causal limit, $P = \epsilon$.

In β-equilibrium, all of DD2(Y), DDB(Y), and DID(Y) are in reasonable agreement with the constraint from Ref. [19] based on causality and $M_{\rm max} > 1.97\ M_\odot$ (Fig. 31). At low energy densities $\epsilon \lesssim 300$ MeV fm^{-3}, all models exhibit nearly identical behavior in the nucleon-dominated regime. At higher energy densities $\epsilon \gtrsim 400$ MeV fm^{-3}, the models deviate significantly from each other, as hyperons begin to populate the matter and $g_{\omega N}$ for DID and DIDY bottom out. DDBY's early onset for hyperons causes it to soften drastically at this point compared to DDB. DID and DIDY are also moderately softer than DDB for $\epsilon \simeq (250\text{–}550)$ MeV fm^{-3}, after which the hyperon onset begins in DIDY but the EoSs are both comparable to DDB. DD2 is stiffer than all of these, while

DD2Y is between DDBY and DIDY in stiffness.

Plotting c_s^2 (as calculated from Eq. (82) with cubic interpolation), we found that in contrast to DD2Y and DDBY, which show small dips at the hyperon onset but steadily increase afterward, DIDY shows a large peak of $c_s^2 = 0.71$ at 0.66 fm^{-3}, driven by the plateauing of $g_{\omega N}$ near this density, before rapidly descending to $c_s^2 = 0.54$ near 1.05 fm^{-3} and gradually increasing afterward (Fig. 32). Other models based on HIC or NS data also tend to predict this feature in their $c_s^2(n_B)$ profiles [172, 17]. None of the models converge to the conformal limit of $c_s^2 = 1/3$ at high density, as quark models do.

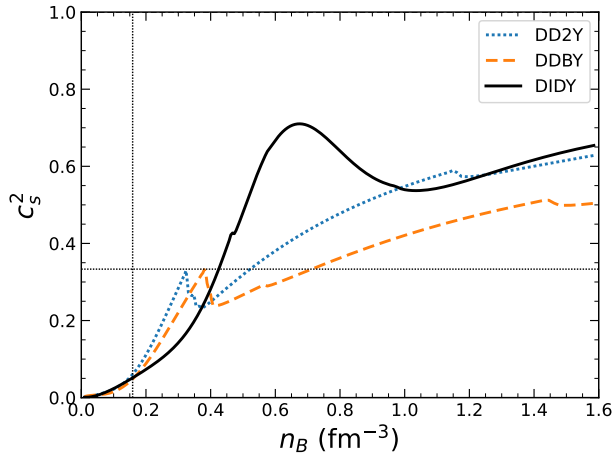

Figure 32: Speed of sound squared of DDB, DID, and DD2Y as a function of baryon density, in β-equilibrium with electrons but not nuclei. The dotted line at $c_s^2 = 1/3$ is the conformal limit.

10.1.2 Composition and hyperon potentials

In Fig. 33, we plot the hyperon potentials in DD2Y, DIDY, and DDBY as functions of density and against the HALQCD potentials at n_0 [2]. In symmetric matter, they are similar at and below n_0, but the Λ and Ξ potentials increase faster in DIDY at high density. The neutron-matter hyperon potentials is where DID's isospin dependence has the strongest impact: in the latter two models, the Λ and Σ^0 values are ~ 20 MeV below their symmetric values in DDBY, while the DID potentials and the HALQCD potentials at $|\mathbf{k}| = 0$ are slightly above the symmetric ones. A hyperon appears in the EoS at $T = 0$ if and only if $\nu_i > m_i^*$, which upon rearrangement by adding Σ_i^v to both sides,

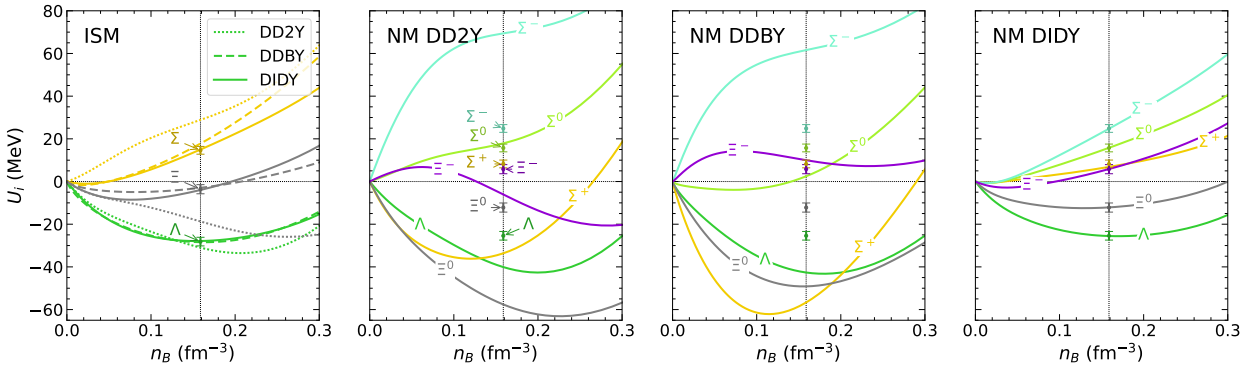

Figure 33: Comparison of hyperon potentials of DIDY and DDBY in symmetric matter (left) and in neutron matter (center and right) against the HALQCD results at n_0 (central error bars in each figure) [2].

gives a necessary and sufficient condition for hyperon onset:

$$\mu_i > m_i + U_i. \tag{260}$$

Fig. 34 plots the baryon fractions of various constituents in β-equilibrium, and the densities at which hyperons first appear under these conditions is shown in Table 10. An unusual finding is that, despite its repulsive interaction with nucleons, the Σ^- is a major constituent of the NS inner core in DID, appearing at much lower densities than Λ in β-equilibrium. This happens because at low Y_q, the Σ^- potential is relatively lower, and the Λ potential higher, than in DDBY. The composition of DDBY and our model in β-equilibrium with electrons only is shown in Fig. 34. All three models predict an appearance of the heavier, doubly strange Ξ^- baryon at higher densities, but it happens much later in DIDY than in DD2Y or DDBY because its potential increases more dramatically above n_0.

We also see that the DID model has a different proton fraction $X_p \simeq 0.03$ at $n = n_0$, while the DDB and DD2 models give $X_p \simeq 0.05$. This seeming contradiction for two models with similar saturation properties is resolved by considering the expansion of the binding energy per nucleon of nuclear matter beyond the quadratic approximation in terms of the asymmetry β. Generally, this dependence can be presented as a power series (Eq. (85)) [16]. In practice, the symmetry energy

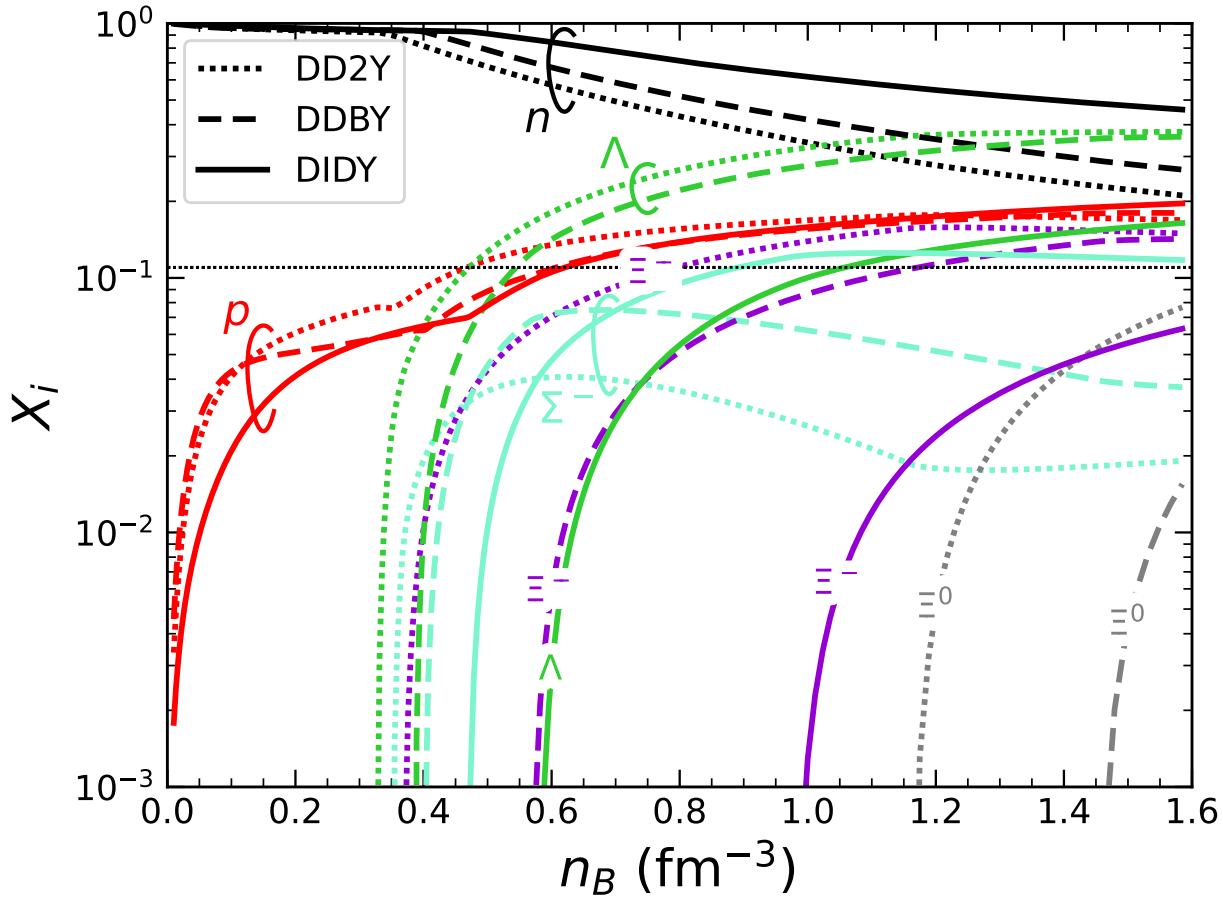

Figure 34: Composition of DD2Y vs. DDBY vs. DIDY in β-equilibrium as a function of density, including nuclei.

Table 10: Density of hyperon onset, in fm^{-3}, for cold β-equilibrated matter, as calculated from Eq. (260). The Ξ^0 does not appear in DIDY below the maximum density of the table, and the Σ^+ and Σ^0 do not appear in any of the models.

Baryon	DD2Y	DDBY	DIDY
Λ	0.327	0.386	0.623
Σ^-	0.352	0.401	0.479
Ξ^-	0.369	0.568	1.013
Ξ^0	1.162	1.453	—

S_2, which we used for the Bayesian analysis, is much larger than subsequent coefficients and close to S. In the parabolic approximation, where B is exactly quadratic in β and $m_e \ll \mu_B$ [173],

$$\mu_L = \frac{1}{n_B}\left(\frac{\partial \epsilon}{\partial X_p}\right)_{n_B} = (3\pi^2 n_B X_p)^{1/3} + 4S_2(2X_p - 1). \tag{261}$$

Adding the next term in the expansion $B(\beta)$, of order β^4, corrects this by

$$\mu_L^{(4)} = 2\frac{\partial}{\partial \beta}(S_4\beta^4) = 8S_4(2X_p - 1)^3, \tag{262}$$

and likewise for higher-order coefficients. Thus, a positive $S - S_2$ will lower μ_L in neutron-rich matter and raise the X_p of β-equilibrium relative to the parabolic approximation (m_e is still small relative to this correction). The S_2's of DD2, DDB, and DID are similar ($\simeq 31$ MeV), but while $S - S_2$ is positive in DD2 and DDB, it is negative in DID (Table 11). Therefore, DID has a lower β-equilibrated X_p at saturation density.

Table 11: Both definitions of symmetry energy, slope $L = 3\,\partial S/\partial x$, incompressibility $K = 9\,\partial^2 B/\partial x^2$, skewness $Q = 27\,\partial^3 B/\partial x^3$, $K_{\rm sym} = 9\,\partial^2 S/\partial x^2$, and X_p in β-equilibrium at saturation density; as well as M at 0.11 fm^{-3}; compared to estimates from experiment or ChEFT. X_p is dimensionless, n_0 in fm^{-3}, and all other quantities are in MeV.

Quantity	DD2	DDB	DID	Emp.	Ref.
n_0	0.149065	0.143862	0.158800	0.150±0.010	[88]
B	−16.02	−15.27	−15.40	−15.6±0.6	[169]
K	242.68	210.87	227.06	240±20	[169]
Q	168.58	−138.05	−608.09		
$M(0.11\ \text{fm}^{-3})$	1148.70	1215.57	1122.72	1100±70	[170]
S_2	31.67	30.26	32.44	32.0±1.1	[16]
$S - S_2$	1.00	0.86	−2.72	1.2±1.5	[174]
L_2	55.03	38.10	59.90	53±13	[16]
$L - L_2$	2.67	2.28	0.05	0±6	[174]
$K_{\rm sym2}$	−93.23	−117.99	−130.59	−78±43	[16]
$K_{\rm sym} - K_{\rm sym2}$	−0.46	−0.06	33.27	−24±58	[174]
$X_p^{\rm eq}(n_0)$	0.0523	0.0481	0.0336		

10.2 NS properties

The NS mass–radius curves, as the tidal deformability Λ, the moment of inertia I, and the central energy density ϵ_c were calculated using the `QLIMR` module of the MUSES Collaboration Calculation Engine [175] at $T = 0.1$ MeV in β-equilibrium, using the HS crust model. Some calculated properties are listed in Table 12.

Table 12: Various properties of neutron stars calculated with the HS crust model.

Property	DD2	DD2Y	DDB	DDBY	DID	DIDY
$R_{1.4}$ (km)	13.25	13.24	12.65	12.65	11.99	11.99
$\Lambda_{1.4}$	702.37	700.24	511.30	510.40	355.13	355.00
$n_B^{c(1.4)}$ (fm^{-3})	0.349	0.358	0.410	0.418	0.487	0.488
$I_{1.4}$ ($M_\odot$ km^2)	86.18	86.10	79.11	79.07	71.85	71.85
$M_{\max}$ ($M_\odot$)	2.422	2.035	2.199	1.864	2.245	2.196
$R_{\max}$ (km)	12.06	11.46	11.17	11.06	10.87	10.91
$\Lambda_{\max}$	6.34	15.13	6.89	22.30	4.92	6.13
$n_B^{c(\max)}$ (fm^{-3})	0.804	0.983	1.004	1.097	1.008	0.999
$I_{\max}$ ($M_\odot$ km^2)	165.92	111.65	125.46	91.69	127.92	123.32

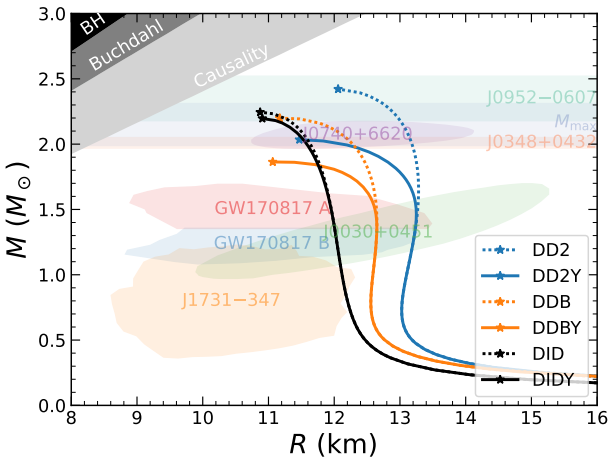

Figure 35: Mass–radius plot for non-rotating NSs for several EoS's compared against 2σ confidence regions for the mass and radius of PSR J0740+6620 [20], PSR J0030+0451 [21], the low-mass compact object HESS J1731−347 [22], and the predecessors of GW170817 [23]; 1σ mass measurements for the high-mass pulsars PSR J0952−0607 [24] and J0348+0432 [25]; and the $M_{\max}$ estimate at 1σ from Ref. [26] based on GW170817.

In Fig. 35, we first plot the mass–radius relations against some high-mass pulsars and those with radius measurements based on X-ray spectroscopy, such as PSR J0740+6620. DID is consistent

with all the plotted confidence zones. In particular, it is the only EoS consistent with the 3σ lower bound of 2.09 $M_\odot$ estimated by Ref. [24] based on PSR J0952−0607, and it is marginally consistent with the low-mass compact object HESS J1731−347 [22] at $0.77^{+0.20}_{-0.17}$ $M_\odot$ and $10.4^{+0.86}_{-0.78}$ km. We see that while the NS $M_{\max}$ in the DD2(Y) and DDB(Y) models are significantly affected by the appearance of hyperons, the effect of hyperons on the mass–radius curve is very small in the DID model. In particular, the decrease of the maximum NS mass due to hyperons is just $0.049\,M_\odot$, resolving the hyperon puzzle with more realistic neutron-matter potentials.

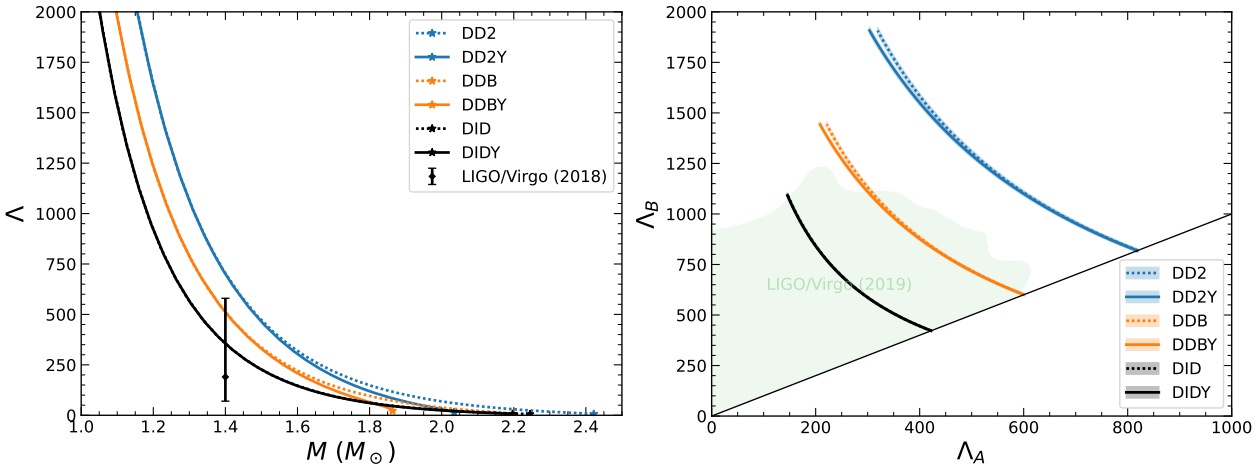

(a) (b)

Figure 36: (a) Λ vs. mass for non-rotating NSs, compared against the 90% confidence interval at 1.4 $M_\odot$ from GW170817 [23]. (b) Λ_1 and Λ_2 for the two components of GW170817 against the constraint from Ref. [27]. By convention, $M_A \geq M_B$, which implies $\Lambda_A \leq \Lambda_B$; this bound is marked by the solid black line.

For Λ, we computed the mass–Λ relation (Fig. 36a). The constraint $\Lambda_{1.4} = 190^{+390}_{-120}$ (90% confidence) from Ref. [23] is marginally consistent with DDBY, and DID is in much closer agreement. We also used this relation to obtain the Λ's for each component of the GW170817 system, which had a chirp mass of 1.186(1) $M_\odot$ and a 90% confidence upper bound of 1.60 $M_\odot$ for the primary [27]. From Eq. (108), we can recover the mass of one component as a depressed cubic equation:

$$m_B^3 - \frac{\mathcal{M}^{1/5}}{m_A^3} m_B - \frac{\mathcal{M}^{1/5}}{m_A^2} = 0 \tag{263}$$

This can be solved in closed form from the other one using the Cardano formula:[14]

$$m_B = \left(\frac{\mathcal{M}^5}{m_A^2} + \sqrt{D}\right)^{1/3} + \left(\frac{\mathcal{M}^5}{m_A^2} - \sqrt{D}\right)^{1/3} \tag{264}$$

where

$$D = \frac{\mathcal{M}^{10}}{m_A^4}\left(\frac{1}{4} - \frac{\mathcal{M}^5}{27 m_A^5}\right). \tag{265}$$

From the strict relation between the GW170817 masses, we can draw a curve (with a small uncertainty band) in Λ_A–Λ_B space for GW170817 within a model. Again, DDBY and DIDY are within the 90% confidence zone estimated by Ref. [27], while DD2Y falls far outside it (Fig. 36b).

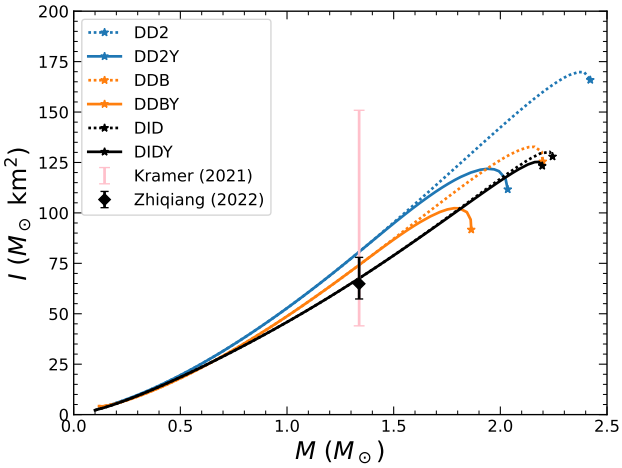

Figure 37: Moment of inertia vs. mass for non-rotating NSs, compared with that estimated for PSR J0737−3039A. from Ref. [28]. The pink error bar demarcates the upper (90% confidence) and lower (causal) bounds on the same NS from Ref. [29].

For moment of inertia, I versus mass is plotted against the constraints from Refs. [29, 28] on the primary component of the Double Pulsar, PSR J0737−3039A ($M = 1.3381(7)\ M_\odot$ [135]), in Fig. 37. While DD2Y meets the very broad limits of $I_{\rm J0737A} \in [44.0, 150.9]\ M_\odot\ {\rm km}^2$ from Ref. [29], it fails the far narrower estimate of $I_{\rm J0737A} = 64.9^{+13.1}_{-7.5}\ M_\odot\ {\rm km}^2$ from Ref. [28]. While the latter estimate is model-dependent in principle, the two models the authors tried gave indistinguishable posteriors, and their results are similar to other published estimates for $I_{\rm J0737A}$. DIDY is close to

[14]The solution of a cubic equation is expressible in real numbers if and only if it has one real root. For the chirp-mass problem, it can be verified by the reader that D in Eq. (265) is always real if $m_A \geq m_B$.

the median estimate, while DDBY falls near the upper limit of this confidence interval.

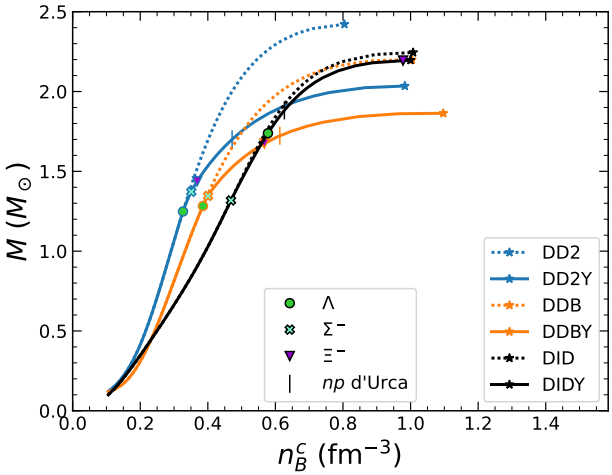

Figure 38: Mass vs. central baryon density n_B^c for non-rotating NSs in DD2Y, DDBY, and DIDY. Colored markers are the critical densities for hyperon onsets, and vertical marks are an estimate for the onset of the $n \to p + e^- + \overline{\nu}_e$ direct Urca process, which in nucleonic matter without muons happens if $X_p \gtrsim 1/9$ [30].

Lastly, we remark that the central baryon density of DIDY is comparable to DD2Y for high-mass NSs (Fig. 38). Below $\sim 1.5\ M_\odot$, DIDY has the highest central density while DD2Y has the lowest. DDBY's central density overtakes DID around $1.65\ M_\odot$, and DD2Y surpasses DIDY near $1.9\ M_\odot$. All three n_B^c's increase rapidly as the EoSs approach their respective maximum masses: in DIDY, it increases from $0.681\ \mathrm{fm}^{-3}$ at $2.0\ M_\odot$ to $0.999\ \mathrm{fm}^{-3}$ at the maximum mass of $2.196\ M_\odot$. The hyperonic inner core appears around $M \simeq (1.25\text{–}1.3)\ M_\odot$ in all three models, and in particular the Σ^- appears in NSs above $(1.3\text{–}1.4)\ M_\odot$. However, the Λ in DIDY is delayed to $M \geq 1.738\ M_\odot$, and whereas Ξ^- begins at $1.437\ M_\odot$ in DD2Y and $1.675\ M_\odot$ in DDBY, in DIDY it does not appear unless the NS is very close to the maximum mass ($\geq 2.194\ M_\odot$). The critical threshold of $X_p \simeq 1/9$ for the $n \to p + e^- + \overline{\nu}_e$ direct Urca process [30] is also delayed from $1.700\ M_\odot$ in DD2Y and $1.723\ M_\odot$ in DDBY to $1.882\ M_\odot$ in DIDY. We have not investigated the inclusion of muons, which would make up $\sim 1\%$ of the NS mass, and probably less in the hyperonic EoSs due to competition with the negative hyperons [176].

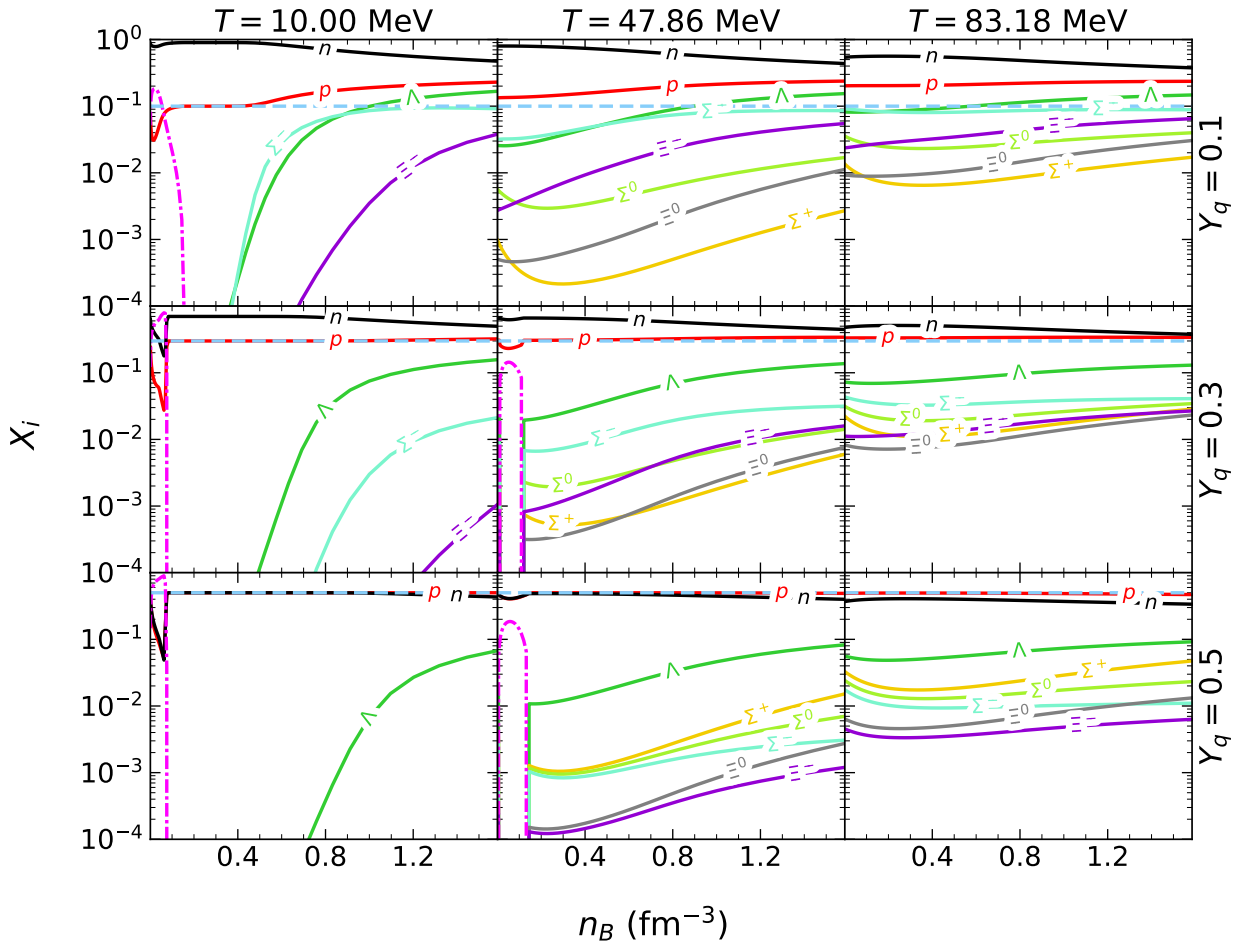

Figure 39: Baryon fractions in DIDY as functions of density for $T \in \exp_{10}\{1.00, 1.68, 1.92\} \approx \{10.00, 47.86, 83.18\}$ MeV for $Y_q \in \{0.1, 0.3, 0.5\}$.

10.3 Finite temperature

Fig. 39 plots the baryon fractions of hyperons and nuclei at $T \approx 10, 48, 83$ MeV and $Y_q \in \{0.1, 0.3, 0.5\}$. Sharp hyperon thresholds characterize the low-temperature regime ($T \lesssim 10$ MeV): for example, X_Λ at $T = 10$ MeV and $Y_q = 0.3$ increases from 2.1×10^{-4} at $n_B \simeq 0.52$ fm^{-3} to 0.075 at $n_B = 1.00$ fm^{-3}. Increasing to $T \simeq 48$ MeV broadens these sharp thresholds into smooth transitions where multiple hyperon species coexist over wider density ranges, including the Σ^0, which is strongly suppressed at low temperatures by being in chemical equilibrium with the less massive

Λ.[15] Thermal effects dominate at $T \simeq 83$ MeV, populating all hyperon species simultaneously. As the isospin asymmetry decreases from $Y_q = 0.1$ to $Y_q = 0.5$, the hyperon fractions become more isospin-degenerate, whereas for large asymmetries the negatively charged baryons have significantly larger fractions. Overall, the temperature and asymmetry dependences of the hyperon fractions are qualitatively similar to the ones observed in the literature [142].

The cluster phase is also more prominent at Y_q closer to 0.5, vanishing at higher temperatures compared to the case with low Y_q. At $T = 10$ MeV, X_A peaks at around 0.18 at $n_B \sim 0.021$ fm^{-3}, while at $Y_q = 0.5$ and the same density, $X_A \simeq 0.70$, and it continues to increase until $X_A \simeq 0.90$ before the Maxwell transition. At $T \simeq 48$ MeV, X_A for the $Y_q = 0.5$ case had dropped to about 0.14, while the crust phase for $Y_q = 0.1$ has vanished. $\langle A \rangle$ also decreases dramatically with temperature: for $Y_q = 0.5$ at $n_B \sim 0.021$ fm^{-3}, it is around 128, but by $T = 10$ MeV, only the lightest nuclei remain, with $\langle A \rangle \simeq 3.5$. This is qualitatively similar to other models of the NS crust at finite temperature [45].

11 Conclusions

Since the discovery of the first neutron stars in the 1960s, immense progress has been made on understanding their structure and what it implies for the still poorly understood intermediate-density, low-temperature region of the QCD phase diagram between the ChEFT and NS-crust regime of $\lesssim 1.1\ n_0$ and the perturbative regime at $\gtrsim 20\ n_0$. In particular, very little is known about the formation of hyperons in the dense nuclear medium, and how they can be reconciled with observed high-mass NSs such as PSR J0740+6620; NS cooling rates; and the radius and Λ measurements from LIGO/Virgo and the NICER X-ray telescope.

This dissertation improves this understanding by incorporating hyperons, alongside data on bulk nuclear matter compiled over the past two decades, into a DD-RMF EoS with a novel isospin-dependent coupling, called DID(Y), that replicates the isospin-asymmetry Fock-term effects in

[15] The mass difference in vacuum is 77 MeV, and the Σ^0 decays electromagnetically to Λ on a timescale of $\sim 10^{-20}$ s [1].

BHF. In particular, we have also reproduced realistic LQCD-based hyperon potentials in neutron matter for the first time, and the resulting EoS is also relatively soft at intermediate densities, lowering Λ relative to DD2 in accordance with GW170817 constraints; and its c_s^2 profile features a large peak. This will lead to more accurate modeling of the hyperon contents of the NS, particularly for cooling since Σ^- rather than Λ is the most abundant hyperon in NSs around 1.4–1.8 $M_\odot$; as well as of GW events involving NS or NS–BH mergers. We have also developed a tool for the MUSES Collaboration that will make future progress on DD-RMFs accessible to the field.

Nonetheless, some gaps remain. For instance, DID does not include the δ meson, which required us to break $\mathrm{SU}(3)_f$ symmetry in the ρ sector to compensate. If the δ is primarily tetraquark or $K\overline{K}$ with hidden strangeness, as is supported by weak decays of charmed mesons and baryons such as $D^+ \to \delta^+ + \pi^0$ [1, 177], then it may couple more strongly to hyperons, an effect that would be masked in our model and deflate the effective ρ coupling of the hyperons. It is possible that extending the $\mathrm{SU}(3)_f$ symmetry to the light scalar nonet, which would also introduce the ζ as a neutral isoscalar that preferentially couples to hyperons, will reveal this effect.

Secondly, it is possible to map out the liquid–gas phase transition without hyperons: its critical point is where the Maxwell transition goes away. However, a version of HS that incorporates hyperons, and possibly anti-nuclei, will be needed to fully understand what happens to the nuclei in the regime where they dissipate, patching over what are currently sharp discontinuities in the composition (though not of the thermodynamic variables) where both clusters and hyperons can exist, but the hyperonic phase becomes lower in free energy.

Thirdly, it would be interesting to apply the isospin-dependent coupling formalism to a description of finite nuclei in light of the CREX/PREX controversy [16, 178], which is a tension between measurements of L using the neutron skins of ^{48}Ca (CREX) and ^{208}Pb (PREX). The current work presents an example of large-scale Bayesian analysis to constrain a model with 17 parameters, which is made possible by modern high-performance computing; and it will be expanded to even larger scales upon application of machine learning-based tools like TOV emulators [179].

Finally, it would be interesting to constrain b_ω or b_ρ explicitly using data from HICs or NSs.

This procedure would likely constrain b_ω and b_ρ using their predicted effects on NS properties. In particular, cooling rates are sensitive to the amount of hyperons of the NS inner core [30, 122]. The species not included in our models, such as charged mesons and the Δ baryons, are likely to have an impact as well [30, 180]. For the Δs, their presence tends to soften the EoS at near-saturation density and stiffen it at higher density, resulting in smaller radii for 1.4 $M_\odot$ NSs but increasing the maximum mass, and the $\Delta^- \to \Lambda + e^- + \overline{\nu}_e$ [41, 180]. For the charged-meson scenarios, their presence has a smaller effect on cooling rates than nucleon Urca processes [121, 181], but their effects on NS properties are strongly model-dependent [42].

In conclusion, DD-RMFs are an established tool for describing hadronic matter throughout the hadronic phase of QCD matter, and DID represents the next phase of innovation in the development of the hadronic EoS.

Bibliography

[1] Particle Data Group Collab., "Review of particle physics," *Phys. Rev. D*, vol. 110, p. 030001, August 2024.

[2] T. Inoue and for HAL QCD Collaboration, "Strange nuclear physics from QCD on lattice," *AIP Conference Proceedings*, vol. 2130, p. 020002, July 2019.

[3] S. Raby, *Introduction to the Standard Model and Beyond*. Cambridge University Press, 2021.

[4] M. Wang, W. Huang, F. Kondev, G. Audi, and S. Naimi, "The AME 2020 atomic mass evaluation (II). tables, graphs and references," *Chinese Phys. C*, vol. 45, p. 030003, 2021.

[5] P. Möller, A. J. Sierk, T. Ichikawa, and H. Sagawa, "Nuclear ground-state masses and deformations: FRDM(2012)," *Atomic Data and Nuclear Data Tables*, vol. 109-110, pp. 1–204, 2016.

[6] J. Keller, C. Wellenhofer, K. Hebeler, and A. Schwenk, "Neutron matter at finite temperature based on chiral effective field theory interactions," *Physical Review C*, vol. 103, May 2021.

[7] E. Annala, T. Gorda, A. Kurkela, J. Nättilä, and A. Vuorinen, "Evidence for quark-matter cores in massive neutron stars," *Nature Physics*, vol. 16, no. 9, pp. 907–910, 2020.

[8] D. Keane, "The beam energy scan at the Relativistic Heavy Ion Collider," *Journal of Physics: Conference Series*, vol. 878, p. 012015, July 2017.

[9] D. H. Rischke, "The quark–gluon plasma in equilibrium," *Progress in Particle and Nuclear Physics*, vol. 52, no. 1, pp. 197–296, 2004.

[10] D. Radice, "General-relativistic large-eddy simulations of binary neutron star mergers," *The Astrophysical Journal Letters*, vol. 838, p. L2, March 2017.

[11] D. Radice, S. Bernuzzi, W. D. Pozzo, L. F. Roberts, and C. D. Ott, "Probing extreme-density matter with gravitational-wave observations of binary neutron star merger remnants," *The Astrophysical Journal Letters*, vol. 842, p. L10, June 2017.

[12] P. Braun-Munzinger and B. Dönigus, "Loosely-bound objects produced in nuclear collisions at the LHC," *Nuclear Physics A*, vol. 987, pp. 144–201, 2019.

[13] C. Ratti, "Lattice QCD and heavy ion collisions: a review of recent progress," *Reports on Progress in Physics*, vol. 81, p. 084301, July 2018.

[14] F. Weber, R. Negreiros, and P. Rosenfield, *Neutron Star Interiors and the Equation of State of Superdense Matter*, pp. 213–245. Berlin, Heidelberg: Springer Berlin Heidelberg, 2009.

[15] C. Drischler, R. Furnstahl, J. Melendez, and D. Phillips, "How well do we know the neutron-matter equation of state at the densities inside neutron stars? a Bayesian approach with correlated uncertainties," *Physical Review Letters*, vol. 125, November 2020.

[16] J. M. Lattimer, "Constraints on nuclear symmetry energy parameters," *Particles*, vol. 6, no. 1, pp. 30–56, 2023.

[17] D. Oliinychenko, A. Sorensen, V. Koch, and L. McLerran, "Sensitivity of Au + Au collisions to the symmetric nuclear matter equation of state at 2–5 nuclear saturation densities," *Phys. Rev. C*, vol. 108, p. 034908, September 2023.

[18] P. Danielewicz, R. Lacey, and W. G. Lynch, "Determination of the equation of state of dense matter," *Science*, vol. 298, pp. 1592–1596, 2002.

[19] K. Hebeler, J. M. Lattimer, C. J. Pethick, and A. Schwenk, "Equation of state and neutron star properties constrained by nuclear physics and observation," *The Astrophysical Journal*, vol. 773, p. 11, July 2013.

[20] T. E. Riley, A. L. Watts, P. S. Ray, S. Bogdanov, S. Guillot, S. M. Morsink, A. V. Bilous, Z. Arzoumanian, D. Choudhury, J. S. Deneva, K. C. Gendreau, A. K. Harding, W. C. G. Ho, J. M. Lattimer, M. Loewenstein, R. M. Ludlam, C. B. Markwardt, T. Okajima, C. Prescod-Weinstein, R. A. Remillard, M. T. Wolff, E. Fonseca, H. T. Cromartie, M. Kerr, T. T. Pennucci, A. Parthasarathy, S. Ransom, I. Stairs, L. Guillemot, and I. Cognard, "A NICER view of the massive pulsar PSR J0740+6620 informed by radio timing and XMM-Newton spectroscopy," *The Astrophysical Journal Letters*, vol. 918, p. L27, September 2021.

[21] G. Raaijmakers, T. E. Riley, A. L. Watts, S. K. Greif, S. M. Morsink, K. Hebeler, A. Schwenk, T. Hinderer, S. Nissanke, S. Guillot, Z. Arzoumanian, S. Bogdanov, D. Chakrabarty, K. C. Gendreau, W. C. G. Ho, J. M. Lattimer, R. M. Ludlam, and M. T. Wolff, "A NICER view of PSR J0030+0451: Implications for the dense matter equation of state," *The Astrophysical Journal Letters*, vol. 887, p. L22, December 2019.

[22] V. Sagun, E. Giangrandi, T. Dietrich, O. Ivanytskyi, R. Negreiros, and C. Providência, "What is the nature of the HESS J1731-347 compact object?," *Astrophys. J.*, vol. 958, no. 1, p. 49, 2023.

[23] LIGO Collab. and VIRGO Collab., "GW170817: Measurements of neutron star radii and equation of state," *Phys. Rev. Lett.*, vol. 121, p. 161101, October 2018.

[24] R. W. Romani, D. Kandel, A. V. Filippenko, T. G. Brink, and W. Zheng, "PSR J0952−0607: The fastest and heaviest known galactic neutron star," *The Astrophysical Journal Letters*, vol. 934, p. L17, July 2022.

[25] J. Antoniadis, P. C. C. Freire, N. Wex, T. M. Tauris, R. S. Lynch, M. H. van Kerkwijk, M. Kramer, C. Bassa, V. S. Dhillon, T. Driebe, J. W. T. Hessels, V. M. Kaspi, V. I. Kondratiev, N. Langer, T. R. Marsh, M. A. McLaughlin, T. T. Pennucci, S. M. Ransom, I. H. Stairs, J. van Leeuwen, J. P. W. Verbiest, and D. G. Whelan, "A massive pulsar in a compact relativistic binary," *Science*, vol. 340, no. 6131, p. 1233232, 2013.

[26] L. Rezzolla, E. R. Most, and L. R. Weih, "Using gravitational-wave observations and quasi-universal relations to constrain the maximum mass of neutron stars," *The Astrophysical Journal Letters*, vol. 852, p. L25, January 2018.

[27] LIGO Collab. and VIRGO Collab., "Properties of the binary neutron star merger GW170817," *Phys. Rev. X*, vol. 9, p. 011001, January 2019.

[28] Z. Miao, A. Li, and Z.-G. Dai, "On the moment of inertia of PSR J0737−3039 A from LIGO/Virgo and NICER," *Monthly Notices of the Royal Astronomical Society*, vol. 515, pp. 5071–5080, July 2022.

[29] M. Kramer, I. H. Stairs, R. N. Manchester, N. Wex, A. T. Deller, W. A. Coles, M. Ali, M. Burgay, F. Camilo, I. Cognard, T. Damour, G. Desvignes, R. D. Ferdman, P. C. C. Freire, S. Grondin, L. Guillemot, G. B. Hobbs, G. Janssen, R. Karuppusamy, D. R. Lorimer, A. G. Lyne, J. W. McKee, M. McLaughlin, L. E. Münch, B. B. P. Perera, N. Pol, A. Possenti, J. Sarkissian, B. W. Stappers, and G. Theureau, "Strong-field gravity tests with the double pulsar," *Phys. Rev. X*, vol. 11, p. 041050, December 2021.

[30] T. Klahn *et al.*, "Constraints on the high-density nuclear equation of state from the phenomenology of compact stars and heavy-ion collisions," *Phys. Rev. C*, vol. 74, p. 035802, 2006.

[31] M. E. Peskin and D. V. Schroeder, *An Introduction to Quantum Field Theory*. Westview Press, Student Economy ed., 2016.

[32] A. M. Jaffe, "The millennium grand challenge in mathematics," *Notices of the AMS*, vol. 53, no. 6, pp. 652–660, 2006.

[33] D. G. Pak, R.-G. Cai, T. Tsukioka, P. Zhang, and Y.-F. Zhou, "Inherent color symmetry in quantum Yang-Mills theory," *Physics Letters B*, vol. 839, p. 137804, 2023.

[34] S. Mitra, "Determination of lattice QCD equation of state at a finite chemical potential," in *Proceedings of the XXV DAE-BRNS High Energy Physics (HEP) Symposium 2022, 12–16 December, Mohali, India* (S. Jena, A. Shivaji, V. Bhardwaj, K. Lochan, H. K. Jassal, A. Joseph, and P. Khuswaha, eds.), (Singapore), pp. 209–212, Springer Nature Singapore, 2024.

[35] I. Vidaña, "A short walk through the physics of neutron stars," *The European Physical Journal Plus*, vol. 133, no. 10, p. 445, 2018.

[36] W. Baade and F. Zwicky, "Remarks on super-novae and cosmic rays," *Phys. Rev.*, vol. 46, pp. 76–77, July 1934.

[37] A. Hewish and S. E. Okoye, "Evidence for an unusual source of high radio brightness temperature in the Crab Nebula," *Nature*, vol. 207, no. 4992, pp. 59–60, 1965.

[38] I. S. Shklovsky, "On the nature of the source of X-ray emission of Sco XR-1.," *ApJL*, vol. 148, p. L1, April 1967.

[39] S. J. B. Burnell, "Petit four," *Annals of the New York Academy of Sciences*, vol. 302, no. 1, pp. 685–689, 1977.

[40] R. V. E. Lovelace and G. L. Tyler, "On the discovery of the period of the Crab Nebula pulsar," *The Observatory*, vol. 132, pp. 186–188, June 2012.

[41] L. Tolos and L. Fabbietti, "Strangeness in nuclei and neutron stars," *Progress in Particle and Nuclear Physics*, vol. 112, p. 103770, 2020.

[42] E. E. Kolomeitsev, K. A. Maslov, and D. N. Voskresensky, "Charged ρ-meson condensation in neutron stars," *Nucl. Phys. A*, vol. 970, pp. 291–315, 2018.

[43] K. D. Marquez, D. P. Menezes, H. Pais, and C. m. c. Providência, "Δ baryons in neutron stars," *Phys. Rev. C*, vol. 106, p. 055801, November 2022.

[44] S. Banik, M. Hempel, and D. Bandyopadhyay, "New hyperon equations of state for supernovae and neutron stars in density-dependent hadron field theory," *Astrophys. J. Suppl.*, vol. 214, p. 22, 2014.

[45] M. Hempel and J. Schaffner-Bielich, "Statistical model for a complete supernova equation of state," *Nucl. Phys. A*, vol. 837, 210-254, pp. 210–254, 2010.

[46] L. W. Alvarez and F. Bloch, "A quantitative determination of the neutron moment in absolute nuclear magnetons," *Phys. Rev.*, vol. 57, pp. 111–122, January 1940.

[47] V. E. Barnes, P. L. Connolly, D. J. Crennell, B. B. Culwick, W. C. Delaney, W. B. Fowler, P. E. Hagerty, E. L. Hart, N. Horwitz, P. V. C. Hough, J. E. Jensen, J. K. Kopp, K. W. Lai, J. Leitner, J. L. Lloyd, G. W. London, T. W. Morris, Y. Oren, R. B. Palmer, A. G. Prodell, D. Radojičić, D. C. Rahm, C. R. Richardson, N. P. Samios, J. R. Sanford, R. P. Shutt, J. R. Smith, D. L. Stonehill, R. C. Strand, A. M. Thorndike, M. S. Webster, W. J. Willis, and S. S. Yamamoto, "Observation of a hyperon with strangeness minus three," *Phys. Rev. Lett.*, vol. 12, pp. 204–206, February 1964.

[48] Y.-B. Yang, J. Liang, Y.-J. Bi, Y. Chen, T. Draper, K.-F. Liu, and Z. Liu, "Proton mass decomposition from the QCD energy momentum tensor," *Phys. Rev. Lett.*, vol. 121, p. 212001, November 2018.

[49] K. Raya, A. Bashir, D. Binosi, C. D. Roberts, and J. Rodríguez-Quintero, "Pseudoscalar mesons and emergent mass," *Few-Body Systems*, vol. 65, no. 2, p. 60, 2024.

[50] C. P. Burgess, *Introduction to Effective Field Theory.* Cambridge University Press, 2021.

[51] W. F. Chen, "Differential geometry from quantum field theory," *International Journal of Geometric Methods in Modern Physics*, vol. 10, no. 04, p. 1350003, 2013.

[52] A. Deur, S. J. Brodsky, and G. F. de Téramond, "The QCD running coupling," *Progress in Particle and Nuclear Physics*, vol. 90, pp. 1–74, September 2016.

[53] K. K. Pathak, S. Bhattacharya, and T. Das, "Parameterisation space for Cornell potential in a QCD potential model," *The European Physical Journal C*, vol. 82, no. 11, p. 1081, 2022.

[54] R. Gupta, "Introduction to lattice QCD," 1998.

[55] M. W. Davis, *The geometry and topology of Coxeter groups*, vol. 32 of *Lond. Math. Soc. Monogr. Ser.* Princeton, NJ: Princeton University Press, 2008.

[56] D. Tong, *Lectures on Gauge Theory.* University of Cambridge, 2018.

[57] Y. Aoki, T. Blum, S. Collins, L. D. Debbio, M. D. Morte, P. Dimopoulos, X. Feng, M. Golterman, S. Gottlieb, R. Gupta, G. Herdoiza, P. Hernandez, A. Jüttner, T. Kaneko, E. Lunghi, S. Meinel, C. Monahan, A. Nicholson, T. Onogi, P. Petreczky, A. Portelli, A. Ramos, S. R. Sharpe, J. N. Simone, S. Sint, R. Sommer, N. Tantalo, R. V. de Water, A. Vaquero, U. Wenger, and H. Wittig, "FLAG review 2024," *Phys. Rev. D*, pp. –, June 2025.

[58] R. Aliberti, T. Aoyama, E. Balzani, A. Bashir, G. Benton, J. Bijnens, V. Biloshytskyi, T. Blum, D. Boito, M. Bruno, E. Budassi, S. Burri, L. Cappiello, C. Carloni Calame, M. Cè, V. Cirigliano, D. Clarke, G. Colangelo, L. Cotrozzi, M. Cottini, I. Danilkin, M. Davier, M. Della Morte, A. Denig, C. DeTar, V. Druzhinin, G. Eichmann, A. El-Khadra, E. Estrada, X. Feng, C. Fischer, R. Frezzotti, G. Gagliardi, A. Gérardin, M. Ghilardi, D. Giusti, M. Golterman, S. Gonzàlez-Solís, S. Gottlieb, R. Gruber, A. Guevara, V. Gülpers, A. Gurgone, F. Hagelstein, M. Hayakawa, N. Hermansson-Truedsson, A. Hoecker, M. Hoferichter, B.-L. Hoid, S. Holz, R. Hudspith, F. Ignatov, L. Jin, N. Kalntis, G. Kanwar, A. Keshavarzi, J. Komijani, J. Koponen, S. Kuberski, B. Kubis, A. Kupich, A. Kupść, S. Lahert, S. Laporta, C. Lehner, M. Lellmann, L. Lellouch, T. Leplumey, J. Leutgeb, T. Lin, Q. Liu, I. Logashenko, C. London, G. López Castro, J. Lüdtke, A. Lusiani, A. Lutz, J. Mager, B. Malaescu, K. Maltman, M. Marinković, J. Márquez, P. Masjuan, H. Meyer, T. Mibe, N. Miller, A. Miramontes, A. Miranda, G. Montagna, S. Müller, E. Neil, A. Nesterenko, O. Nicrosini, M. Nio, D. Nomura, J. Paltrinieri, L. Parato, J. Parrino, V. Pascalutsa, M. Passera, S. Peris, P. Petit Rosàs, F. Piccinini, R. Pilato, L. Polat, A. Portelli, D. Portillo-Sánchez, M. Procura, L. Punzi, K. Raya, A. Rebhan, C. Redmer, B. Roberts, A. Rodríguez-Sánchez, P. Roig, J. Ruiz de Elvira, P. Sánchez-Puertas, A. Signer, J. Sitison, D. Stamen, D. Stöckinger, H. Stöckinger-Kim, P. Stoffer, Y. Sue, P. Tavella, T. Teubner, J.-N. Toelstede, G. Toledo, W. Torres Bobadilla, J. Tsang, F. Ucci, Y. Ulrich, R. Van de Water, G. Venanzoni, S. Volkov, G. von Hippel, G. Wang, U. Wenger, H. Wittig, A. Wright, E. Zaid, M. Zanke, Z. Zhang, M. Zillinger, C. Alexandrou, A. Altherr, M. Anderson, C. Aubin, S. Bacchio, P. Beltrame, A. Beltran, P. Boyle, I. Campos Plasencia, I. Caprini, B. Chakraborty, G. Chanturia, A. Crivellin, A. Czarnecki, L.-Y. Dai, T. Dave, L. Del Debbio, K. Demory, D. Djukanovic, T. Draper, A. Driutti, M. Endo, F. Erben, K. Ferraby, J. Finkenrath, L. Flower, A. Francis, E. Gámiz, J. Gogniat, A. Grebe, S. Gündogdu, M. Hansen, S. Hashimoto, H. Hayashii, D. Hertzog, L. Heuser, L. Hostetler, X. Hou, G. Huang, T. Iijima, K. Inami, A. Jüttner, R. Kitano, M. Knecht, S. Kollatzsch, A. Kronfeld, T. Lenz, G. Levati, Q. Li, Y. Liao, J. Libby, K. Liu, V. Lubicz, M. Lynch, A. Lytle, J. Ma, K. Miura, K. Möhling, J. Muskalla, F. Noël, K. Ottnad, P. Paradisi, C. Peterson, A. Pich, S. Pitelis, S. Plura, A. Price, D. Radic, A. Radzhabov, A. Risch, S. Romiti, S. Sahoo, F. Sannino, H. Schäfer, Y. Schelhaas, S. Serednyakov, O. Shekhovtsova, J. Simone, S. Simula, E. Solodov, F. Stokes, M. Vanderhaeghen, A. Vaquero, N. Vestergaard, W. Wang, Z. Wąs, K. Yamashita, Y. Yang, T. Yoshioka, C. Yuan, and A. Zhevlakov, "The anomalous magnetic moment of the muon in the Standard Model: an update," *Physics Reports*, vol. 1143, pp. 1–158, November 2025.

[59] S. D. Bass and P. Moskal, "η' and η mesons with connection to anomalous glue," *Rev. Mod. Phys.*, vol. 91, p. 015003, February 2019.

[60] N. H. Christ, C. Dawson, T. Izubuchi, C. Jung, Q. Liu, R. D. Mawhinney, C. T. Sachrajda, A. Soni, and R. Zhou, "η and η' mesons from lattice QCD," *Phys. Rev. Lett.*, vol. 105, p. 241601, December 2010.

[61] T. Miyatsu, M.-K. Cheoun, and K. Saito, "Asymmetric nuclear matter in relativistic mean-field models with isoscalar- and isovector-meson mixing," *The Astrophysical Journal*, vol. 929, p. 82, April 2022.

[62] P. J. Mohr, D. B. Newell, B. N. Taylor, and E. Tiesinga, "CODATA recommended values of the fundamental physical constants: 2022," *Rev. Mod. Phys.*, vol. 97, p. 025002, April 2025.

[63] R. B. Wiringa, V. G. J. Stoks, and R. Schiavilla, "Accurate nucleon–nucleon potential with charge-independence breaking," *Phys. Rev. C*, vol. 51, pp. 38–51, January 1995.

[64] R. Machleidt and I. Slaus, "The nucleon–nucleon interaction," *Journal of Physics G: Nuclear and Particle Physics*, vol. 27, p. R69, May 2001.

[65] R. Smolańczuk and J. Dobaczewski, "Particle-drip lines from the Hartree–Fock–Bogoliubov theory with Skyrme interaction," *Phys. Rev. C*, vol. 48, pp. R2166–R2169, November 1993.

[66] Z. Y. Zhang, Z. G. Gan, H. B. Yang, L. Ma, M. H. Huang, C. L. Yang, M. M. Zhang, Y. L. Tian, Y. S. Wang, M. D. Sun, H. Y. Lu, W. Q. Zhang, H. B. Zhou, X. Wang, C. G. Wu, L. M. Duan, W. X. Huang, Z. Liu, Z. Z. Ren, S. G. Zhou, X. H. Zhou, H. S. Xu, Y. S. Tsyganov, A. A. Voinov, and A. N. Polyakov, "New isotope ^{220}Np: Probing the robustness of the $N = 126$ shell closure in neptunium," *Phys. Rev. Lett.*, vol. 122, p. 192503, May 2019.

[67] D. S. Ahn, J. Amano, H. Baba, N. Fukuda, H. Geissel, N. Inabe, S. Ishikawa, N. Iwasa, T. Komatsubara, T. Kubo, K. Kusaka, D. J. Morrissey, T. Nakamura, M. Ohtake, H. Otsu, T. Sakakibara, H. Sato, B. M. Sherrill, Y. Shimizu, T. Sumikama, H. Suzuki, H. Takeda, O. B. Tarasov, H. Ueno, Y. Yanagisawa, and K. Yoshida, "Discovery of ^{39}Na," *Phys. Rev. Lett.*, vol. 129, p. 212502, November 2022.

[68] M. Thoennessen, "Reaching the limits of nuclear stability," *Reports on Progress in Physics*, vol. 67, p. 1187, June 2004.

[69] O. B. Tarasov, D. S. Ahn, D. Bazin, N. Fukuda, A. Gade, M. Hausmann, N. Inabe, S. Ishikawa, N. Iwasa, K. Kawata, T. Komatsubara, T. Kubo, K. Kusaka, D. J. Morrissey, M. Ohtake, H. Otsu, M. Portillo, T. Sakakibara, H. Sakurai, H. Sato, B. M. Sherrill, Y. Shimizu, A. Stolz, T. Sumikama, H. Suzuki, H. Takeda, M. Thoennessen, H. Ueno, Y. Yanagisawa, and K. Yoshida, "Discovery of ^{60}Ca and implications for the stability of ^{70}Ca," *Phys. Rev. Lett.*, vol. 121, p. 022501, July 2018.

[70] F. Kondev, M. Wang, W. Huang, S. Naimi, and G. Audi, "The NUBASE2020 evaluation of nuclear physics properties," *Chinese Phys. C*, vol. 45, no. 3, p. 030001, 2021.

[71] M. P. Fewell, "The atomic nuclide with the highest mean binding energy," *American Journal of Physics*, vol. 63, pp. 653–658, July 1995.

[72] P. Belli, R. Bernabei, F. A. Danevich, A. Incicchitti, and V. I. Tretyak, "Experimental searches for rare alpha and beta decays," *The European Physical Journal A*, vol. 55, no. 8, p. 140, 2019.

[73] Y. M. Tsipenyuk, "Valley of nuclear stability," 1999.

[74] H. Koura and S. Chiba, "Single-particle levels of spherical nuclei in the superheavy and extremely superheavy mass region," *Journal of the Physical Society of Japan*, vol. 82, pp. 4201–, January 2013.

[75] C. Pan and X.-H. Wu, "Examination of possible proton magic number $Z = 126$ with the deformed relativistic Hartree–Bogoliubov theory in continuum," *Particles*, vol. 8, no. 1, 2025.

[76] A. Såmark-Roth, D. M. Cox, D. Rudolph, L. G. Sarmiento, B. G. Carlsson, J. L. Egido, P. Golubev, J. Heery, A. Yakushev, S. Åberg, H. M. Albers, M. Albertsson, M. Block, H. Brand, T. Calverley, R. Cantemir, R. M. Clark, C. E. Düllmann, J. Eberth, C. Fahlander, U. Forsberg, J. M. Gates, F. Giacoppo, M. Götz, S. Götz, R.-D. Herzberg, Y. Hrabar, E. Jäger, D. Judson, J. Khuyagbaatar, B. Kindler, I. Kojouharov, J. V. Kratz, J. Krier, N. Kurz, L. Lens, J. Ljungberg, B. Lommel, J. Louko, C.-C. Meyer, A. Mistry, C. Mokry, P. Papadakis, E. Parr, J. L. Pore, I. Ragnarsson, J. Runke, M. Schädel, H. Schaffner, B. Schausten, D. A. Shaughnessy, P. Thörle-Pospiech, N. Trautmann, and J. Uusitalo, "Spectroscopy along flerovium decay chains: Discovery of ^{280}Ds and an excited state in ^{282}Cn," *Phys. Rev. Lett.*, vol. 126, p. 032503, January 2021.

[77] H. L. Crawford, P. Fallon, A. O. Macchiavelli, P. Doornenbal, N. Aoi, F. Browne, C. M. Campbell, S. Chen, R. M. Clark, M. L. Cortés, M. Cromaz, E. Ideguchi, M. D. Jones, R. Kanungo, M. MacCormick, S. Momiyama, I. Murray, M. Niikura, S. Paschalis, M. Petri, H. Sakurai, M. Salathe, P. Schrock, D. Steppenbeck, S. Takeuchi, Y. K. Tanaka, R. Taniuchi, H. Wang, and K. Wimmer, "First spectroscopy of the near drip-line nucleus ^{40}Mg," *Phys. Rev. Lett.*, vol. 122, p. 052501, February 2019.

[78] C. Middleton, "Neutron-rich magnesium undergoes unexpected transitions," *Physics Today*, vol. 72, pp. 14–16, April 2019.

[79] N. Tajima and N. Suzuki, "Prolate dominance of nuclear shape caused by a strong interference between the effects of spin–orbit and l^2 terms of the Nilsson potential," *Phys. Rev. C*, vol. 64, p. 037301, August 2001.

[80] N. Schunck and D. Regnier, "Theory of nuclear fission," *Progress in Particle and Nuclear Physics*, vol. 125, p. 103963, 2022.

[81] STAR Collab., "Imaging shapes of atomic nuclei in high-energy nuclear collisions," *Nature*, vol. 635, no. 8037, pp. 67–72, 2024.

[82] J. Dvorak, W. Brüchle, M. Chelnokov, R. Dressler, C. E. Düllmann, K. Eberhardt, V. Gorshkov, E. Jäger, R. Krücken, A. Kuznetsov, Y. Nagame, F. Nebel, Z. Novackova, Z. Qin, M. Schädel, B. Schausten, E. Schimpf, A. Semchenkov, P. Thörle, A. Türler, M. Wegrzecki, B. Wierczinski, A. Yakushev, and A. Yeremin, "Doubly magic nucleus $^{270}_{108}$Hs$_{162}$," *Phys. Rev. Lett.*, vol. 97, p. 242501, December 2006.

[83] J. Dechargé, J.-F. Berger, K. Dietrich, and M. Weiss, "Superheavy and hyperheavy nuclei in the form of bubbles or semi-bubbles," *Physics Letters B*, vol. 451, no. 3, pp. 275–282, 1999.

[84] S. E. Agbemava and A. V. Afanasjev, "Hyperheavy spherical and toroidal nuclei: The role of shell structure," *Phys. Rev. C*, vol. 103, p. 034323, March 2021.

[85] M. Bender, K. Rutz, P. G. Reinhard, and J. A. Maruhn, "Pairing gaps from nuclear mean-field models," *The European Physical Journal A*, vol. 8, no. 1, pp. 59–75, 2000.

[86] G. D. Mahan, *Many-Particle Physics*. Kluwer Academic/Plenum Publishers, 3rd ed., 2000.

[87] P. Möller and J. Nix, "Nuclear pairing models," *Nuclear Physics A*, vol. 536, no. 1, pp. 20–60, 1992.

[88] C. J. Horowitz, J. Piekarewicz, and B. Reed, "Insights into nuclear saturation density from parity-violating electron scattering," *Phys. Rev. C*, vol. 102, p. 044321, October 2020.

[89] S. Borsányi, Z. Fodor, J. N. Guenther, R. Kara, S. D. Katz, P. Parotto, A. Pásztor, C. Ratti, and K. K. Szabó, "Lattice QCD equation of state at finite chemical potential from an alternative expansion scheme," *Phys. Rev. Lett.*, vol. 126, p. 232001, June 2021.

[90] A. Kurkela, K. Rajagopal, and R. Steinhorst, "Astrophysical equation-of-state constraints on the color-superconducting gap," *Physical Review Letters*, vol. 132, June 2024.

[91] B. Müller and J. Rafelski, *A New Phase of Matter: Quark–Gluon Plasma Beyond the Hagedorn Critical Temperature*, pp. 107–116. Cham: Springer International Publishing, 2016.

[92] B. Müller and J. L. Nagle, "Results from the Relativistic Heavy Ion Collider," *Annual Review of Nuclear and Particle Science*, vol. 56, no. Volume 56, 2006, pp. 93–135, 2006.

[93] H. Song, S. A. Bass, U. Heinz, T. Hirano, and C. Shen, "200 A GeV Au + Au collisions serve a nearly perfect quark–gluon liquid," *Phys. Rev. Lett.*, vol. 106, p. 192301, May 2011.

[94] S. Borsanyi *et al.*, "Calculation of the axion mass based on high-temperature lattice quantum chromodynamics," *Nature*, vol. 539, no. 7627, pp. 69–71, 2016.

[95] S. Weinberg, "Superconductivity for particular theorists," *Progress of Theoretical Physics Supplement*, vol. 86, pp. 43–53, January 1986.

[96] C.-J. Xia, H.-M. Jin, and T.-T. Sun, "Quarkyonic matter and quarkyonic stars in an extended relativistic mean field model," *Phys. Rev. D*, vol. 108, p. 054013, September 2023.

[97] B. Holdom, J. Ren, and C. Zhang, "Quark matter may not be strange," *Phys. Rev. Lett.*, vol. 120, p. 222001, May 2018.

[98] E. Norbeck and Y. Onel, "The strangelet saga," *Journal of Physics: Conference Series*, vol. 316, p. 012034, September 2011.

[99] J. Haidenbauer, U. G. Meissner, and A. Nogga, "Hyperon–nucleon interaction within chiral effective field theory revisited," *Eur. Phys. J. A*, vol. 56, no. 91, 2020.

[100] V. Vovchenko, "Hadron resonance gas with van der Waals interactions," *International Journal of Modern Physics E*, vol. 29, no. 05, p. 2040002, 2020.

[101] C. M. Keil, F. Hofmann, and H. Lenske, "Density dependent hadron field theory for hypernuclei," *Phys. Rev. C*, vol. 61, p. 064309, May 2000.

[102] H. Müller, "Effective field theory for Λ–Σ^0 mixing in nuclear matter," *Phys. Rev. C*, vol. 59, pp. 1405–1421, March 1999.

[103] E. N. E. van Dalen and H. Müther, "Relativistic description of finite nuclei based on realistic NN interactions," *Phys. Rev. C*, vol. 84, p. 024320, August 2011.

[104] A. Y. Potekhin, "The physics of neutron stars," *Physics-Uspekhi*, vol. 53, p. 1235, December 2010.

[105] J. C. Zamora and S. Giraud, "Monopole excitation and nuclear compressibility: Present and future perspectives," *Oxford Research Encyclopedia of Physics*, June 2024.

[106] F. Isaule, H. F. Arellano, and A. Rios, "Di-neutrons in neutron matter within a Brueckner–Hartree–Fock approach," *Physical Review C*, vol. 94, September 2016.

[107] T. M. Tauris and E. P. J. van den Heuvel, "Formation and evolution of compact stellar X-ray sources," in *Compact stellar X-ray sources* (W. H. G. Lewin and M. van der Klis, eds.), vol. 39, pp. 623–665, Cambridge University Press, 2006.

[108] T. M. Tauris, M. Kramer, P. C. C. Freire, N. Wex, H.-T. Janka, N. Langer, P. Podsiadlowski, E. Bozzo, S. Chaty, M. U. Kruckow, E. P. J. v. d. Heuvel, J. Antoniadis, R. P. Breton, and D. J. Champion, "Formation of double neutron star systems," *The Astrophysical Journal*, vol. 846, p. 170, September 2017.

[109] LIGO Collab. and VIRGO Collab., "Multi-messenger observations of a binary neutron star merger," *The Astrophysical Journal Letters*, vol. 848, p. L12, October 2017.

[110] J. M. Weisberg, D. J. Nice, and J. H. Taylor, "Timing measurements of the relativistic binary pulsar PSR B1913+16," *The Astrophysical Journal*, vol. 722, p. 1030, September 2010.

[111] LIGO Collab. and VIRGO Collab., "GW170817: Observation of gravitational waves from a binary neutron star inspiral," *Phys. Rev. Lett.*, vol. 119, p. 161101, October 2017.

[112] J. R. Green, A. D. Hanlon, P. M. Junnarkar, and H. Wittig, "Weakly bound H dibaryon from SU(3)-flavor-symmetric QCD," *Phys. Rev. Lett.*, vol. 127, p. 242003, December 2021.

[113] A. Ayriyan, N.-U. Bastian, D. Blaschke, H. Grigorian, K. Maslov, and D. N. Voskresensky, "Robustness of third family solutions for hybrid stars against mixed phase effects," *Phys. Rev. C*, vol. 97, p. 045802, April 2018.

[114] X.-L. Zhang, Y.-F. Huang, and Z.-C. Zou, "Recent progresses in strange quark stars," *Frontiers in Astronomy and Space Sciences*, vol. 11, p. 1409463, 2024.

[115] A. Ohnishi, D. Jido, T. Sekihara, and K. Tsubakihara, "Possibility of an s-wave pion condensate in neutron stars reexamined," *Phys. Rev. C*, vol. 80, p. 038202, September 2009.

[116] J. Yasuda, M. Sasano, R. G. T. Zegers, H. Baba, D. Bazin, W. Chao, M. Dozono, N. Fukuda, N. Inabe, T. Isobe, G. Jhang, D. Kameda, M. Kaneko, K. Kisamori, M. Kobayashi, N. Kobayashi, T. Kobayashi, S. Koyama, Y. Kondo, A. J. Krasznahorkay, T. Kubo, Y. Kubota, M. Kurata-Nishimura, C. S. Lee, J. W. Lee, Y. Matsuda, E. Milman, S. Michimasa,

T. Motobayashi, D. Muecher, T. Murakami, T. Nakamura, N. Nakatsuka, S. Ota, H. Otsu, V. Panin, W. Powell, S. Reichert, S. Sakaguchi, H. Sakai, M. Sako, H. Sato, Y. Shimizu, M. Shikata, S. Shimoura, L. Stuhl, T. Sumikama, H. Suzuki, S. Tangwancharoen, M. Takaki, H. Takeda, T. Tako, Y. Togano, H. Tokieda, J. Tsubota, T. Uesaka, T. Wakasa, K. Yako, K. Yoneda, and J. Zenihiro, "Extraction of the Landau–Migdal parameter from the Gamow–Teller giant resonance in ^{132}Sn," *Phys. Rev. Lett.*, vol. 121, p. 132501, September 2018.

[117] D. N. Voskresensky, "Pion softening and pion condensation," *Physics of Atomic Nuclei*, vol. 83, no. 2, pp. 188–202, 2020.

[118] A. Gal, E. V. Hungerford, and D. J. Millener, "Strangeness in nuclear physics," *Rev. Mod. Phys.*, vol. 88, p. 035004, 2016.

[119] K. Sasaki, S. Aoki, T. Doi, S. Gongyo, T. Hatsuda, Y. Ikeda, T. Inoue, T. Iritani, N. Ishii, K. Murano, and T. Miyamoto, "$\Lambda\Lambda$ and $N\Xi$ interactions from lattice QCD near the physical point," *Nuclear Physics A*, vol. 998, p. 121737, 2020.

[120] D. K. Nadyozhin, "Gamow and the physics and evolution of stars," *Space Science Reviews*, vol. 74, pp. 455–461, November 1995.

[121] H. Grigorian, D. N. Voskresensky, and K. A. Maslov, "Cooling of neutron stars in "nuclear medium cooling scenario" with stiff equation of state including hyperons," *Nucl. Phys. A*, vol. 980, pp. 105–130, 2018.

[122] A. R. Raduta, J. J. Li, A. Sedrakian, and F. Weber, "Cooling of hypernuclear compact stars: Hartree–Fock models and high-density pairing," *Mon. Not. Roy. Astron. Soc.*, vol. 487, no. 2, pp. 2639–2652, 2019.

[123] V. M. Kaspi and A. M. Beloborodov, "Magnetars," *Annual Review of Astronomy and Astrophysics*, vol. 55, no. Volume 55, 2017, pp. 261–301, 2017.

[124] K. D. Marquez, M. R. Pelicer, S. Ghosh, J. Peterson, D. Chatterjee, V. Dexheimer, and D. P. Menezes, "Exploring the effects of Δ baryons in magnetars," *Phys. Rev. C*, vol. 106, p. 035801, September 2022.

[125] R. R. Silbar and S. Reddy, "Neutron stars for undergraduates," *American Journal of Physics*, vol. 72, pp. 892–905, July 2004.

[126] A. Del Popolo, M. Le Delliou, and M. Deliyergiyev, "Neutron stars and dark matter," *Universe*, vol. 6, no. 12, 2020.

[127] B. Schutz, *A First Course in General Relativity.* Cambridge University Press, 2nd ed., 2009.

[128] A. Tsokaros, M. Ruiz, S. L. Shapiro, L. Sun, and K. b. o. Uryū, "Great impostors: Extremely compact, merging binary neutron stars in the mass gap posing as binary black holes," *Phys. Rev. Lett.*, vol. 124, p. 071101, February 2020.

[129] Y. Suwa, T. Yoshida, M. Shibata, H. Umeda, and K. Takahashi, "On the minimum mass of neutron stars," *Monthly Notices of the Royal Astronomical Society*, vol. 481, pp. 3305–3312, September 2018.

[130] Potekhin, A. Y., Fantina, A. F., Chamel, N., Pearson, J. M., and Goriely, S., "Analytical representations of unified equations of state for neutron-star matter," *A&A*, vol. 560, p. A48, 2013.

[131] E. Fonseca, H. T. Cromartie, T. T. Pennucci, P. S. Ray, A. Y. Kirichenko, S. M. Ransom, P. B. Demorest, I. H. Stairs, Z. Arzoumanian, L. Guillemot, A. Parthasarathy, M. Kerr, I. Cognard, P. T. Baker, H. Blumer, P. R. Brook, M. DeCesar, T. Dolch, F. A. Dong, E. C. Ferrara, W. Fiore, N. Garver-Daniels, D. C. Good, R. Jennings, M. L. Jones, V. M. Kaspi, M. T. Lam, D. R. Lorimer, J. Luo, A. McEwen, J. W. McKee, M. A. McLaughlin, N. McMann, B. W. Meyers, A. Naidu, C. Ng, D. J. Nice, N. Pol, H. A. Radovan, B. Shapiro-Albert, C. M. Tan, S. P. Tendulkar, J. K. Swiggum, H. M. Wahl, and W. W. Zhu, "Refined mass and geometric measurements of the high-mass PSR J0740+6620," *The Astrophysical Journal Letters*, vol. 915, p. L12, July 2021.

[132] K. Chatziioannou, "Neutron-star tidal deformability and equation-of-state constraints," *General Relativity and Gravitation*, vol. 52, no. 11, p. 109, 2020.

[133] T. Hinderer, "Tidal Love numbers of neutron stars," *The Astrophysical Journal*, vol. 677, p. 1216, April 2008.

[134] A. Worley, P. G. Krastev, and B.-A. Li, "Nuclear constraints on the moments of inertia of neutron stars," *The Astrophysical Journal*, vol. 685, p. 390, September 2008.

[135] M. Kramer, I. H. Stairs, R. N. Manchester, M. A. McLaughlin, A. G. Lyne, R. D. Ferdman, M. Burgay, D. R. Lorimer, A. Possenti, N. D'Amico, J. M. Sarkissian, G. B. Hobbs, J. E. Reynolds, P. C. C. Freire, and F. Camilo, "Tests of general relativity from timing the double pulsar," *Science*, vol. 314, no. 5796, pp. 97–102, 2006.

[136] PREX Collaboration, "Accurate determination of the neutron skin thickness of ^{208}Pb through parity-violation in electron scattering," *Phys. Rev. Lett.*, vol. 126, p. 172502, April 2021.

[137] G. Giacalone, G. Nijs, and W. van der Schee, "Determination of the neutron skin of ^{208}Pb from ultrarelativistic nuclear collisions," *Phys. Rev. Lett.*, vol. 131, p. 202302, November 2023.

[138] T. M. Tauris and E. van den Heuvel, "Formation and evolution of compact stellar X-ray sources," 2003.

[139] Q. An, T. Lu, G. M. Brandt, T. D. Brandt, and G. Li, "Significant mutual inclinations between the stellar spin and the orbits of both planets in the HAT-P-11 system," *The Astronomical Journal*, vol. 169, p. 22, December 2024.

[140] J. M. Weisberg and J. H. Taylor, "Relativistic binary pulsar B1913+16: Thirty years of observations and analysis," in *Binary radio pulsars* (F. A. Rasio and I. H. Stairs, eds.), vol. 328 of *ASP Conference Series*, pp. 25–31, Aspen Conference, 2005.

[141] I. H. Stairs, "Testing general relativity with pulsar timing," *Living Reviews in Relativity*, vol. 6, no. 1, p. 5, 2003.

[142] S. Tsiopelas, A. Sedrakian, and M. Oertel, "Finite-temperature equations of state of compact stars with hyperons: three-dimensional tables," *The European Physical Journal A*, vol. 60, no. 6, p. 127, 2024.

[143] E. D. Barr, A. Dutta, P. C. C. Freire, M. Cadelano, T. Gautam, M. Kramer, C. Pallanca, S. M. Ransom, A. Ridolfi, B. W. Stappers, T. M. Tauris, V. V. Krishnan, N. Wex, M. Bailes, J. Behrend, S. Buchner, M. Burgay, W. Chen, D. J. Champion, C.-H. R. Chen, A. Corongiu, M. Geyer, Y. P. Men, P. V. Padmanabh, and A. Possenti, "A pulsar in a binary with a compact object in the mass gap between neutron stars and black holes," *Science*, vol. 383, no. 6680, pp. 275–279, 2024.

[144] M. H. P. M. van Putten and M. Della Valle, "Observational evidence for extended emission to GW170817," *Monthly Notices of the Royal Astronomical Society: Letters*, vol. 482, pp. L46–L49, September 2018.

[145] M. Marques, M. Oertel, M. Hempel, and J. Novak, "New temperature dependent hyperonic equation of state: Application to rotating neutron star models and I–Q relations," *Phys. Rev. C*, vol. 96, p. 045806, October 2017.

[146] S. Typel, G. Röpke, T. Klähn, D. Blaschke, and H. H. Wolter, "Composition and thermodynamics of nuclear matter with light clusters," *Phys. Rev. C*, vol. 81, no. 015803, 2010.

[147] T. Malik, M. Ferreira, B. K. Agrawal, and C. Providência, "Relativistic description of dense matter equation of state and compatibility with neutron star observables: A Bayesian approach," *The Astrophysical Journal*, vol. 930, p. 17, April 2022.

[148] T. Malik, S. Banik, and D. Bandyopadhyay, "Equation-of-state table with hyperon and antikaon for supernova and neutron star merger," *The Astrophysical Journal*, vol. 910, p. 96, April 2021.

[149] J. I. Kapusta and C. Gale, *Finite-Temperature Field Theory: Principles and Applications*. Cambridge University Press, 2nd ed., 2006.

[150] Y. Gambhir, P. Ring, and A. Thimet, "Relativistic mean field theory for finite nuclei," *Annals of Physics*, vol. 198, no. 1, pp. 132–179, 1990.

[151] D. Peña-Arteaga, S. Goriely, and N. Chamel, "Relativistic mean-field mass models," *The European Physical Journal A*, vol. 52, no. 10, p. 320, 2016.

[152] E. van Dalen, C. Fuchs, and A. Faessler, "The relativistic Dirac–Brueckner approach to asymmetric nuclear matter," *Nuclear Physics A*, vol. 744, pp. 227–248, 2004.

[153] S. Weissenborn, D. Chatterjee, and J. Schaffner-Bielich, "Hyperons and massive neutron stars: Vector repulsion and SU(3) symmetry," *Phys. Rev. C*, vol. 85, p. 065802, June 2012.

[154] J. J. de Swart, "The octet model and its Clebsch–Gordan coefficients," *Rev. Mod. Phys.*, vol. 35, pp. 916–939, 1963. [Erratum: *Rev. Mod. Phys.*, vol. 37, p. 326, 1965].

[155] M. Oertel, C. Providência, F. Gulminelli, and A. R. Raduta, "Hyperons in neutron star matter within relativistic mean-field models," *Journal of Physics G: Nuclear and Particle Physics*, vol. 42, p. 075202, June 2015.

[156] S. Wang, H. Tong, Q. Zhao, C. Wang, P. Ring, and J. Meng, "Neutron–proton effective mass splitting in neutron-rich matter," *Phys. Rev. C*, vol. 108, p. L031303, September 2023.

[157] L. G. Teodoro dos Santos, T. Malik, and C. m. c. Providência, "Impact of the scalar isovector δ meson on the description of nuclear matter and neutron star properties," *Phys. Rev. C*, vol. 111, p. 035805, March 2025.

[158] J. Schaffner and I. N. Mishustin, "Hyperon-rich matter in neutron stars," *Phys. Rev. C*, vol. 53, pp. 1416–1429, March 1996.

[159] S. Typel and H. H. Wolter, "Relativistic mean field calculations with density dependent meson nucleon coupling," *Nucl. Phys. A*, vol. 656, pp. 331–364, 1999.

[160] B.-A. Li, B.-J. Cai, L.-W. Chen, and J. Xu, "Nucleon effective masses in neutron-rich matter," *Progress in Particle and Nuclear Physics*, vol. 99, pp. 29–119, 2018.

[161] E. van Dalen and H. Müther, "Relativistic effects in nuclear matter and nuclei," *International Journal of Modern Physics E*, vol. 19, no. 11, pp. 2077–2122, 2010.

[162] P. Möller, M. Mumpower, T. Kawano, and W. Myers, "Nuclear properties for astrophysical and radioactive-ion-beam applications (II)," *Atomic Data and Nuclear Data Tables*, vol. 125, pp. 1–192, 2019.

[163] N. Chamel, "Effective mass of free neutrons in neutron star crust," *Nucl. Phys. A*, vol. 773, pp. 263–278, 2006.

[164] J. Nymann, "On the probability that k positive integers are relatively prime," *Journal of Number Theory*, vol. 4, no. 5, pp. 469–473, 1972.

[165] M. Hempel, G. Pagliara, and J. Schaffner-Bielich, "Conditions for phase equilibrium in supernovae, protoneutron, and neutron stars," *Phys. Rev. D*, vol. 80, p. 125014, December 2009.

[166] R. L. Burden, D. J. Faires, and A. M. Burden, *Numerical Analysis*. Cengage Learning, 10th ed., 2016.

[167] F. Feroz, M. P. Hobson, and M. Bridges, "`MultiNest`: an efficient and robust Bayesian inference tool for cosmology and particle physics," *Monthly Notices of the Royal Astronomical Society*, vol. 398, pp. 1601–1614, October 2009.

[168] J. Buchner, A. Georgakakis, K. Nandra, L. Hsu, C. Rangel, M. Brightman, A. Merloni, M. Salvato, J. Donley, and D. Kocevski, "X-ray spectral modelling of the AGN obscuring region in the CDFS: Bayesian model selection and catalogue," *Astronomy & Astrophysics*, vol. 564, p. A125, April 2014.

[169] K. A. Maslov, E. E. Kolomeitsev, and D. N. Voskresensky, "Relativistic Mean-Field Models with Scaled Hadron Masses and Couplings: Hyperons and Maximum Neutron Star Mass," *Nucl. Phys. A*, vol. 950, pp. 64–109, 2016.

[170] E. Khan, J. Margueron, and I. Vidaña, "Constraining the nuclear equation of state at subsaturation densities," *Phys. Rev. Lett.*, vol. 109, p. 092501, August 2012.

[171] A. Sorensen, K. Agarwal, K. W. Brown, Z. Chajęcki, P. Danielewicz, C. Drischler, S. Gandolfi, J. W. Holt, M. Kaminski, C.-M. Ko, R. Kumar, B.-A. Li, W. G. Lynch, A. B. McIntosh, W. G. Newton, S. Pratt, O. Savchuk, M. Stefaniak, I. Tews, M. B. Tsang, R. Vogt, H. Wolter, H. Zbroszczyk, N. Abbasi, J. Aichelin, A. Andronic, S. A. Bass, F. Becattini, D. Blaschke, M. Bleicher, C. Blume, E. Bratkovskaya, B. A. Brown, D. A. Brown, A. Camaiani, G. Casini, K. Chatziioannou, A. Chbihi, M. Colonna, M. D. Cozma, V. Dexheimer, X. Dong, T. Dore, L. Du, J. A. Dueñas, H. Elfner, W. Florkowski, Y. Fujimoto, R. J. Furnstahl, A. Gade, T. Galatyuk, C. Gale, F. Geurts, F. Gramegna, S. Grozdanov, K. Hagel, S. P. Harris, W. Haxton, U. Heinz, M. P. Heller, O. Hen, H. Hergert, N. Herrmann, H. Z. Huang, X.-G. Huang, N. Ikeno, G. Inghirami, J. Jankowski, J. Jia, J. C. Jiménez, J. Kapusta, B. Kardan, I. Karpenko, D. Keane, D. Kharzeev, A. Kugler, A. Le Fèvre, D. Lee, H. Liu, M. A. Lisa, W. J. Llope, I. Lombardo, M. Lorenz, T. Marchi, L. McLerran, U. Mosel, A. Motornenko, B. Müller, P. Napolitani, J. B. Natowitz, W. Nazarewicz, J. Noronha, J. Noronha-Hostler, G. Odyniec, P. Papakonstantinou, Z. Paulínyová, J. Piekarewicz, R. D. Pisarski, C. Plumberg, M. Prakash, J. Randrup, C. Ratti, P. Rau, S. Reddy, H.-R. Schmidt, P. Russotto, R. Ryblewski, A. Schäfer, B. Schenke, S. Sen, P. Senger, R. Seto, C. Shen, B. Sherrill, M. Singh, V. Skokov, M. Spaliński, J. Steinheimer, M. Stephanov, J. Stroth, C. Sturm, K.-J. Sun, A. Tang, G. Torrieri, W. Trautmann, G. Verde, V. Vovchenko, R. Wada, F. Wang, G. Wang, K. Werner, N. Xu, Z. Xu, H.-U. Yee, S. Yennello, and Y. Yin, "Dense nuclear matter equation of state from heavy-ion collisions," *Progress in Particle and Nuclear Physics*, vol. 134, p. 104080, 2024.

[172] I. Tews, J. Carlson, S. Gandolfi, and S. Reddy, "Constraining the speed of sound inside neutron stars with chiral effective field theory interactions and observations," *Astrophys. J.*, vol. 860, no. 2, p. 149, 2018.

[173] S. P. Harris, "Symmetry energy expansion and the peak value of the bulk viscosity," *Phys. Rev. C*, vol. 112, no. 3, p. 035806, 2025.

[174] R. Somasundaram, C. Drischler, I. Tews, and J. Margueron, "Constraints on the nuclear symmetry energy from asymmetric-matter calculations with chiral NN and $3N$ interactions," *Phys. Rev. C*, vol. 103, p. 045803, April 2021.

[175] T. A. Manning, "MUSES Calculation Engine," February 2025.

[176] N.-B. Zhang and B.-A. Li, "Constraints on the muon fraction and density profile in neutron stars," *Astrophys. J.*, vol. 893, p. 61, 2020.

[177] H.-Y. Cheng, C.-W. Chiang, and F. Xu, "Tetraquark nature of the $a_0(980)$ meson in hadronic D decays," *Phys. Rev. D*, vol. 110, p. 094052, November 2024.

[178] T. Miyatsu, M.-K. Cheoun, K. Kim, and K. Saito, "Can the PREX-2 and CREX results be understood by relativistic mean-field models with the astrophysical constraints?," *Phys. Lett. B*, vol. 843, p. 138013, 2023.

[179] B. T. Reed, R. Somasundaram, S. De, C. L. Armstrong, P. Giuliani, C. Capano, D. A. Brown, and I. Tews, "Toward accelerated nuclear-physics parameter estimation from binary neutron star mergers: Emulators for the Tolman–Oppenheimer–Volkoff equations," *Astrophys. J.*, vol. 974, no. 2, p. 285, 2024.

[180] J. J. Li, A. Sedrakian, and F. Weber, "Competition between delta isobars and hyperons and properties of compact stars," *Phys. Lett. B*, vol. 783, pp. 234–240, 2018.

[181] D. Yakovlev and C. Pethick, "Neutron star cooling," *Annual Review of Astronomy and Astrophysics*, vol. 42, pp. 169–210, September 2004.